BIOPHYSICAL AND CHEMICAL MECHANISMS OF CELLULAR ORGANIZATION AND DYNAMICS DURING 3-D VASCULOGENESIS

A Dissertation

Presented to the Faculty of the Graduate School

of Cornell University

In Partial Fulfillment of the Requirements for the Degree of

Doctor of Philosophy

by

Valerie Cross

February 2010

BIOPHYSICAL AND CHEMICAL MECHANISMS OF CELLULAR ORGANIZATION AND DYANMICS DURING 3-D VASCULOGENESIS

Valerie Cross, Ph. D.

Cornell University 2010

The morphogenesis of the vascular system is a complex and interesting example of cellular self-organization, but understanding the principles of the process remains an outstanding challenge in the field of developmental biology. The two key sequential processes that underlie the vascular developmental process include *vasculogenesis* and *angiogenesis*. *Vasculogenesis* is the process by which endothelial progenitor cells interact to form a honeycomb-like network of channels of uniform diameter called the primary vascular plexus. *Angiogenesis* is the growth and remodeling of this structure to form new vessels after the onset of flow and is a process known to be critical during wound healing, development, and cancer. Here, we describe our work developing and characterizing native type I collagen matrices for three-dimensional cell culture and then using these matrices with human umbilical vein endothelial cells to study the critical steps and mechanisms of cellular self-organization during vascular network formation *in vitro*. Because the primary vascular plexus precedes the functional vascular network *in vivo,* it is an appropriate base state for investigating angiogenesis and the formation of the mature vascular system. An accurate understanding of this process would advance research in basic cell biology and angiogenesis during development and disease and form the basis of powerful tissue engineering strategies.

BIOGRAPHICAL SKETCH

Valerie Lynne Cross (Curtis) was born on June 7, 1981 in Darlington, Wisconsin. Valerie grew up on a small farm near Shullsburg, Wisconsin where she attended elementary, junior high, and high school. She spent her summers working on the farm, helping in her parents' veterinary practices, riding ponies, and working in the woods with her two older sisters. Valerie's daily chores and responsibilities on the farm taught her the importance of hard work and dedication, traits which remain with her today. After high school, Valerie studied physics and biology at Lawrence University (LU) in Appleton, Wisconsin where she received her B.A. degree in 2003. While attending Lawrence, Valerie developed a passion for distance running, and she competed on the cross country and track teams. Valerie met her future husband, Joshua Cross, while running and studying physics at Lawrence University (he was a teammate and a teaching assistant in her first physics class). After graduation from LU, Valerie moved to Ithaca, New York. In August 2004, Valerie enrolled in the Department of Biomedical Engineering at Cornell University, and she was awarded a three-year graduate fellowship from the Department of Homeland Security. She immediately began working with Dr. Abraham Stroock at Cornell where her research focused on understanding the physical mechanisms of vascular development *in vitro*. While working on her Ph.D. at Cornell, Valerie's passion for running expanded into a passion for running, biking, and swimming, and she competed in and finished three Ironman triathlons. Valerie finished her Ph.D. in Biomedical Engineering in January 2010. She plans to move to the west coast where she will continue solving the interesting puzzles of science and competing in long distance triathlons.

To my parents

ACKNOWLEDGMENTS

I would like to give my sincere gratitude to the many individuals who have supported, guided, challenged, and motivated me at some point during the first twenty-eight years of my existence. I am not able to mention everyone on this page, but I would like to point out a few influential people who have made a significant impact in my life.

First, thank you to my advisor, Abraham Stroock. Abe is one of the most intelligent, creative, and inspiring people I have had the chance of knowing, and he has been an extraordinary advisor in all aspects. I'd like to thank my husband, Josh, for our productive brainstorming sessions at the dinner table and for reminding me to keep things simple. I have also appreciated his MATLAB assistance over the years. I have dedicated this dissertation to my parents and would like to again thank them for their support and encouragement throughout my life. I'd like to acknowledge my sisters, Vanessa and Janelle, who have been my role models and best friends. Thank you to Dr. George Davis who took me into his lab in Texas for a week and sparked my interest in the field of vascular biology and to Dr. Danny Manor who gave me my first job in Ithaca and introduced me to Cornell University. I'd also like to acknowledge Larry Bonassar and Tom Sato for serving as my minor thesis advisors. Finally, thank you to all of my triathlon and running friends and competitors. Taking breaks to train and race during graduate school kept me happy and productive in the lab.

TABLE OF CONTENTS

LIST OF FIGURES

LIST OF TABLES

LIST OF ABBREVIATIONS

1-D –one-dimension (-s, -al)

2-D – two-dimension (-s, -al)

3-D – three-dimension (-s, -al)

AU –airy unit

BCs –boundary conditions

bFGF –basic fibroblast growth factor

DAG -diacylglycerol

DAPI –4’6, diamidino-2-phenylindole

DMSO –dimethyl sulfoxide

ECGS –endothelial cell growth supplement

ECM –extra cellular matrix

ECs –endothelial cells

EDTA - ethylenediamine tetra-acetic acid

FBS –fetal bovine serum

FEM –finite element method

GAGs -glycosaminoglycans

HEPES - 4-(2-hydroxyethyl)-1-piperazineethanesulfonic acid

HUVECs – human umbilical vein endothelial cells

IP3 -inositol triphosphate

M199 –medium 199

MAPK -mitogen-activated protein kinase

MMPs –matrix metalloproteinases

MWCO –molecular weight cut-off

NA –numerical aperture

OSCC -oral squamous cell carcinoma

Pa -Pascal

PBS –phosphate buffered saline

PDMS -polydimethylsiloxane

PKC -protein kinase C

PLC -phospholipase C

PMA –phorbol-12-myristate-13-acetate

SDS-PAGE -sodium dodecyl sulfate polyacrylamide gel electrophoresis

tPA –tissue plasminogen activator

TPA –tetradecanoyl phorbol acetate

TRITC -tetramethylrhodamine isothiocyanate

VE-cadherin –vascular endothelial cadherin

VEGF – vascular endothelial growth factor

LIST OF SYMBOLS

ϕ -volume fraction collagen

ε -porosity

r_H –hydraulic radius [μm]

a –pore radius [μm]

w_c –microchannel width [μm]

h_c –microchannel height [μm]

ρ_c -percolation threshold [cell density]

ρ_{cells} –cell density [cells/ml]

Δx_{cell} –cell-cell separation [μm]

$\bar{r}$ -mean resultant vector

Θ_{mean} -mean angular direction [degrees]

$\Theta_{neighbor}$ –mean angle to neighboring cell [degrees]

$\Theta_{boundary}$ –mean angle to neighboring boundary [degrees]

R- resultant vector magnitude

ϕ_A –predicted angular direction [degrees]

V_0 -length of the projection of the resultant vector towards ϕ_A

N –number of protrusions

α_i –angle of the i^{th} protrusion [degrees]

CHAPTER 1

INTRODUCTION

1-1 Self-organization in biology

Identifying the principles and mechanisms by which dynamic, global organization emerges from the collective behavior of individual, smaller scale units is an outstanding challenge in the field of developmental biology. The concept of self-organization (sometimes also referred to as self-assembly)[1] is ubiquitous in chemistry, materials science, and biology, and while the theories of self-organization were developed with molecules, components of any size have been shown to be able to self-assemble under the right conditions. For example, self-organization of a spatial or temporal pattern occurs at multiple scales in biology from subcellular levels [1, 2] to the level of tissues and organs [3-5] to larger scale systems like the formation of animal coat patterns[6] and the collective behavior of insects[7].

For self-organization to occur, there are a number of criteria that must be satisfied [8]: 1) Molecules (or meso- and macroscopic components) ought to interact with one another through a balance of attractive and repulsive interactions, 2) the individual components must be able to readjust their position once an ordered structure has formed, and 3) the components must be in an environment that allows them to move and search their surroundings (both physically and through mass transport mechanisms).

The morphogenesis of the primary vascular plexus during the process of vasculogenesis is a complex and interesting example of self-organization during

[1] It is important to note that the concepts *self-organization* and *self-assembly* both describe processes that give rise to collective order from dynamic small-scale interactions; however, there are fundamental differences between the mechanisms with respect to the system's thermodynamics and equilibrium state. Throughout this document, I will use the terms *self-organization* and *self-assembly* (implying dynamic and in a nonequilibrium state) interchangeably.

development in which individual cells form an intricate global structure (the primary vascular plexus) which then acquires a function (delivery of nutrients and oxygen throughout the body). Vascular network formation meets the above criteria for a self-organizational process in that 1) endothelial cells (ECs) (mesoscopic components) interact with each other, 2) the cells are able to move around and change their position within the vascular network, and 3) the cellular native extracellular matrix (ECM) and specific cell surface proteins (both *in vivo* and *in vitro*) allow cells to search for and signal to each other.

The mechanisms regulating how and why endothelial cells communicate with other cells during vascular network formation remain unclear. We, and others[9], suggest cell searching, signaling, and interactions are controlled by local interactions. I would like to point out that spatially extended mechanisms may exist, either as a gradient of one or more chemicals or as some longer-range mechanical gradient. However, even though these signals are not precisely local, they also do not contain global information. One must also consider that genetic control remains a critical component of vascular network formation; but, we argue that spatial organization is not genetically pre-patterned, but it emerges from genetically specified molecules. Put differently, genes simply specify the parts that assemble into the functional structure.

The primary function of the vascular network-- to supply tissues with nutrients and oxygen during development and post-natal life-- is well known, but the mechanisms guiding the process are not. Therefore, I focus on the general principles operating during the morphogenesis and the self-organization of the primitive vascular network during a process called vasculogenesis.

1-2 Vasculogenesis and angiogenesis

Two key sequential processes underlie vascular development: vasculogenesis and angiogenesis. Vasculogenesis is the process by which clusters of progenitor cells

locate neighboring cells, migrate, degrade their surrounding extracellular matrix, and interconnect to form a honeycomb-like network of channels of uniform diameter called the primary vascular plexus [10]. This primitive plexus appears prior to the onset of the heart beat, and thus forms when the embryo is still being nourished by diffusion. Remodeling of the primary vascular plexus into a mature vascular system with vessels of various diameters and veins and arteries in a functional loop occurs by a process called angiogenesis [11]. Angiogenesis does not occur until the lumen is perfused with blood flow[12] and blood pressure, shear stress, and convective mass transport become influential. Angiogenesis involves splitting and sprouting of vessels and is known to be critical in many cellular processes including wound healing, development, and cancer [11, 13]. Because the primary vascular plexus develops prior to the mature vascular network and is the base state for which angiogenesis to act, we begin by focusing primarily on the process of vasculogenesis. Near the end of the introduction, we dedicate a discussion to studies of primary plexus remodeling and the challenges associated with *in vitro* study of angiogenesis.

1-3 Studying vasculogenesis in vivo and in vitro

Studies in developing embryos have advanced our knowledge of the molecular and physical mechanisms underlying the morphogenesis of the first embryonic vascular network. The use of knockout mice have significantly aided in the understanding of the molecular pathways that are involved in vascular network formation [14]. The developing zebrafish is a nice model for studying vasculogenesis as it is genetically and optically accessible [15]. By using living transgenic zebrafish embryos which express GFP in the vascular endothelium [16], researchers have been able to study how the vascular trunk develops and then how circulatory flow plays a role in the patterning of the vessels[15]. In addition to angiogenesis studies, the whole-mount quail embryo (both the intra-embryonic and extra-embryonic yolk sac) has been used

as an *in vivo* model of vasculogenesis [17, 18]. It is an excellent model as a mouse monoclonal antibody, QH1, recognizes an epitope on the surface of quail endothelial cells and then confocal microscopy can be used to examine the complete network formation process in a single live embryo [12, 19]. *In vivo* models lack a certain amount of experimental control that one could potentially obtain with *in vitro* systems.

In vitro work investigating the question of how vascular networks form began with Dr. Judah Folkman's work on *in vitro* angiogenesis in 1980 [20]. He and others have shown that, when provided with the right chemical and mechanical stimuli, capillary endothelial cells can spontaneously self-organize into a vascular plexus *in vitro* and even form open lumen [20-22]. Multiple types of assays have been developed to study the key stages and regulators in the processes of vasculogenesis and angiogenesis. They most commonly use endothelial cells seeded in or on an extracellular matrix (ECM) scaffold, and much of the work is still performed in two dimensions [23-31]. The studies of vasculogenesis and angiogenesis *in vitro* include an enormous variety of experimental protocols which make it difficult to settle on a unified description of the biological process. The cell type, ECM type, a 2-D or 3-D format, cell invasion or assembly, and media conditions are just a few examples of parameters that widely vary in these experiments. In Chapter 3, we describe the 3-D format we use to study vasculogenesis *in vitro* which consists of human umbilical vein endothelial cells (HUVECs) embedded within a 3-D type I collagen matrix.

It is important to note that depending on the assay format, *in vitro* models can mimic steps in vasculogenesis or angiogenesis or some combination of both. Invasion assays[22], where cells are plated on top of an ECM and are allowed to invade into the ECM, mimic sprouting angiogenesis. Angiogenesis assays are appropriate for use as a bioassay to identify relevant chemical mediators of vessel sprouting during cancer and other diseases. During 3-D tube formation assays, endothelial cells are suspended

in an ECM (commonly type I collagen) and are allowed to self-assemble into a network of tubes [32]. The first portion of this assay—the self-organization into a plexus—is the key step during vasculogenesis and therefore, is the main format we use in our vascular network formation studies in Chapters 3, 4, and 5.

Both *in vivo* and *in vitro* models of vascular development possess significant limitations. As mentioned above, *in vivo* systems lack control over aspects such as cell density, cell position, and the chemical and mechanical microenvironment of the cells. Similarly, most current *in vitro* systems lack control on the microscale; however, current work in our lab is being done to develop tools to control the cellular microenvironment [33] and to study and control single cell and multicellular dynamics in 3-D matrices which will be discussed in the following chapters. Despite the limitations in the current models, a few key *in vivo* and *in vitro* experiments, described below, have led to a basic understand the mechanisms regulating vasculogenesis.

1-4 Chemical mediators of cell organization during vasculogenesis

Chemotactic cell movement and crosstalk between cells are considered to be a key mechanisms during vasculogenesis [34]. According to Drake and Little [35] (and others), an essential cytokine regulating vasculogenesis is vascular endothelial growth factor (VEGF). There are numerous other cytokines that have been implicated in vascular development including basic fibroblast growth factor (bFGF)[36] and transforming growth factor beta (TGF-β)[37]. Other cytokines cannot be ignored if we are to understand the chemical mediators behind vasculogenesis, but VEGF is the focus of many researchers; there is overwhelming data *in vivo* suggesting that VEGF plays a fundamental role in vasculogenesis and tumor angiogenesis. For example, in studies where mouse embryos lack a single VEGF allele, mice exhibit abnormal vascular development and only survive to mid-gestation [14]. In the quail embryo model, microinjection of high levels of VEGF leads to increased cellular protrusion

activity and vessel formation. Similarly, a loss of function microinjection (excess soluble VEGF receptor to sequester active VEGF molecules) leads to decreased cellular protrusion activity and network formation[19]. It is well-known that tumor cell-secreted VEGF promotes tumor vascularization, thus, anti-VEGF monoclonal antibodies are currently being used as an anti-cancer therapy[38]. *In vitro* studies have also shown that matrix bound and soluble growth factors, including VEGF, induce a chemotactic response in endothelial cells and enhance tube formation [31, 39, 40]. On 2-D substrates, cell migration plays an important role in the cellular dynamics. In contrast, when cells are embedded within a 3-D fibrous matrix such as collagen or fibrin, migration is less prominent as it requires either matrix degradation[41] or amoeboid type movement between collagen fibers[42]. In Chapter 3, results of endothelial cell migration studies are presented.

From the *in vivo* and *in vitro* results presented above, it is apparent that VEGF is critical during vascular development and remodeling, but it is not clear how VEGF controls specific cell-cell interactions during the initial self-assembly of cells into a network. It is also not clear whether chemical gradients (VEGF or other growth factors) are the primary signaling mechanisms when cells are seeded in 3-D environments. More specifically, do gradients of soluble factors signal cells to migrate, perform some kind of directional search, to stretch, or to divide? And how is a 3-D system different than the well-studied 2-D system? In Chapter 4 and 5 we discuss our work towards answering these questions using chemistry (Chapter 4) a new assay format (Chapter 5) that allows us to distinguish mass transport from mechanical cell-cell signaling in a 3-D collagen matrix. The geometry of the new assay consists of cells near boundaries with different mass transport and mechanical properties, which permits an investigation of the role of non-specific soluble factors on cell behavior.

1-5 Mechanical aspects of vascular development

While vascular network formation can be initiated and directed by soluble factors, an increasing amount of evidence has been established that mechanical forces and the ECM are key regulators of cell function [43-45]. Matrix proteins influence cell behavior due to specific binding of cell surface ECM-receptors including the integrin family of receptors[46]. It has been shown that bi-directional cell-ECM signaling ("outside-in/inside-out" signaling) depends on the balance between the traction exerted by the cells and the passive mechanical resistance of the ECM to those cellular forces [47]. For example, recent work in this field has shown that matrix transduced tensional forces in stretched collagen gels are sufficient to control the directional outgrowth of endothelial cells[48], and cells migrate in the direction of increasing ECM stiffness, a mechanotaxis phenomenon known as durotaxis [49].

These results indicate that cells can sense the local tension of their surrounding ECM suggesting the mechanical deformation of the ECM may act as short-range or long-range (perhaps depending on the fibrous nature of the ECM) signaling mechanism for collections of cells. Indeed, mechanical signals that propagate through a compliant 2-D matrix have been shown to influence endothelial cell-cell communication [50], and increasing the stiffness of that matrix changes the deformation field, which changes cell behavior. Similarly, experiments on 2-D fibrin gels have demonstrated that fibrin concentration significantly influences vascular network formation[25]; however, changing matrix concentration not only changes the matrix stiffness, but also changes the available receptors and chemical environment accessible to the cells. Thus, it is difficult to isolate the affect of matrix stiffness alone on network formation. Differentiating the specific contributions of chemokines versus ECM and mechanical signaling is even more complicated because growth factors like VEGF and bFGF can bind to the ECM. It has been established that the different

VEGF isoforms exhibit very different solubility properties and some isoforms are sequestered in the extracellular matrix [51]. The ECM, therefore, acts to regulate the activity of VEGF and other cytokines.

1-6 Mechanical models for vascular network formation

Mechanobiological models have been developed in order to simulate and describe cell patterning and, more specifically, the formation of vascular networks [24, 30, 52, 53]. Following the "wrinkle" experiments of Harris et al.[54] and their finding that the ECM may propagate long-range mechanical signals in 2-D, Murray and Oster [53, 55] developed a comprehensive mechanical model of cell-ECM mechanical interactions aiming to describe the interactions between a cell population and the ECM. They describe the mechanical equilibrium state by incorporating variables of cell density, ECM density, and displacement of the ECM from its original position. They grant that cells exert traction forces on the viscoelastic ECM, the 'dish' below the ECM exerts a drag force on the matrix, and cells move because of haptotaxis and/or chemotaxis. Their theory considers a continuum of cells, and therefore is modeling tissue scale behavior. They apply the classical mass balance equations with vectors corresponding to cell convection (passive), cell migration (active), and cell diffusion, as well as continuum mechanics to describe the displacement as the solution of the force balance equation. The forces generated by the cells are considered proportional to the cell density and the local matrix density. Their model results in three nonlinear differential equations, and they then perform a linear stability analysis of the model. According to the linear stability analysis, Murray and others have shown that for a given density of cells, pattern formation (and instability) occurs only if the traction forces are sufficiently high or the substrate is not too stiff. In other words, cells pull on their ECM and if there are enough cells and the force they exert overcomes the restoring force of the ECM (and the drag force due to the dish below),

the cells in the lower density regions will get pulled towards the cells in the higher density regions generating a pattern where some areas have cells and some do not.

The mechanical activity of cells has been proposed as a way for cells to collect information about the mechanical properties of its environment as well as an important aspect of defining the physiological function of the cell[56]. Bischofs et al.[57] have developed a model for analyzing the elastic interactions for both physical force dipoles and active cells in an isotropic soft medium as well as a soft medium in the presence of a zero-displacement boundary. They use the concept of anisotropic force dipoles to describe the mechanical activity of cells, and their model shows how stress and strain follows from the force dipoles by solving the elastic equations for the geometry and boundary conditions of interest. The main result that I'd like to emphasize is their findings relating to boundary-induced image strain and elastic interactions of cells. They find that in finite 3-D environments the geometry and boundary condition of the sample can affect cell behavior and structure formation. They show that active cells sense anisotropies in their environment and that the cells prefer an environment with large effective stiffness. Therefore cells move/stretch towards clamped boundaries because they can sense this medium which effectively rigidifies towards the boundary. In contrast, cells generally tend to migrate away from a free boundary because the medium effectively softens towards the free boundary. In [58], Bishofs et al. advance their model to show how individual cell behavior translate into collective cell behaviors. Briefly, the screening of elastic fields due to multiple cells and the Poisson ratio of the elastic medium are shown to strongly affect cellular structure formation. Their model demonstrates that cellular structure formation, which would include vascular network formation, could arise from mechanical effects in collections of mechanosensitive cells.

Mechanical models like described above are valuable and insightful but still lack a

complete realistic description of the physical and dynamic phases of vasculogenesis. In addition, the cellular behaviors due to ECM components differ greatly depending on whether the matrix is in a 2-D or 2-D configuration, so modeling the mechanical deformations of a 3-D elastic ECM with embedded cells could generate a new and different understanding of the mechanical aspects of network formation.

1-7 Maturation of the primary vascular plexus

Gaining an understanding of the mechanisms behind vascular self-organization is the first step towards studying flow-induced vascular remodeling *in vitro*. Blood flow through the primary plexus *in vivo* has been shown to play a pivotal role in the maturation of the primary plexus into a functional branching structure. For example, flow is crucial for regulating vessel diameter and the expression and release of growth factors implicated in vascular remodeling. Le Noble et al. [59] investigate how hemodynamic forces influence primary plexus remodeling (angiogenesis) and arterial-venous differentiation. Using incision and ligation in a quail yolk sac model to inhibit flow during critical periods of development, they demonstrate that plexus remodeling and arterial-venous differentiation is a flow-driven process[12]. Others have used genetics to inhibit flow and prevent the maturation of the primary plexus[15].

While these *in vivo* models have advanced our understanding of flow-driven plexus maturation, an *in vitro* model would be ideal for distinguishing the roles of physical stimuli in dictating the maturation of the primary plexus during angiogenesis. An *in vitro* model would give an unprecedented amount of control over flow speeds, pressure gradients (sensed as shear stress), and gradients of chemokines. It would allow one to distinguish the roles of mechanics and chemistry during morphogenesis; however, the tools to create and mature an *in vitro* primary vascular plexus via perfusion have not been established. In Chapter 2, I describe the current work in our lab that is being done to develop tools to control the cellular microenvironment [33]

and to study and control single cell and multicellular dynamics in 3-D matrices.

1-8 Engineering microvascular structure in vitro

The ability to direct the maturation and maintain a functional vascular network *in vitro* would also be an invaluable tool with which to develop complex tissues *in vitro* for tissue engineering purposes. In tissue engineering, cells are often embedded within three-dimensional constructs designed to provide the cells with functional, mechanical cues and for tissue shape [60]. A major limitation in engineering viable three-dimensional, clinically useful tissues *in vitro* is the lack of transport of oxygen, nutrients, and waste byproducts in the interior of the construct, especially with cells that have high metabolic activities [13, 61]. Methods to create microvasculature *in vitro* have been described [62-65]; however, controlled microstructure within a completely cell-remodelable material has not been demonstrated. An endothelial cell lined microfluidic channel within a cell seeded collagen gel is a means to create an accessible, functional microvascular network *in vitro* that can be used supply thick engineered tissue constructs with the necessary nutrients and oxygen for survival.

There are a wide variety of both natural and synthetic matrices used for 3-D cell culture. Chapter 2 describes in more detail these materials as well as how they have been utilized for studying vascular development *in vitro*. We focus on type 1 collagen as it is the most abundant structural protein in tissues, is a natural substrate for cell adhesion and growth, and is remodelable by cells [66]. *In vitro*, type I collagen self-assembles into complex, 3-D supramolecular gels [67]. These fibrillar hydrogels are commonly used for *in vitro* 3-D cell culture scaffolds in angiogenesis assays and fibroblast contraction and migration studies [68-70]. Integration of microfluidic control within a collagen scaffold that is cell-seedable and cell-remodelable would advance tissue engineering of thick complex tissues, and would be a tool to study spatial and temporal patterning in development. In Chapter 2, we focus on

characterizing the mechanical and cellular properties of dense native collagen gels and report upon our initial microfabrication results.

REFERENCES

1. Nedelec, F.J., et al., *Self-organization of microtubules and motors.* Nature, 1997. **389**(6648): p. 305-8.

2. Daga, R.R., et al., *Self-organization of microtubule bundles in anucleate fission yeast cells.* Nat Cell Biol, 2006. **8**(10): p. 1108-13.

3. Katz, M.J. and R.J. Lasek, *Invited review: guidance cue patterns and cell migration in multicellular organisms.* Cell Motil, 1980. **1**(1): p. 141-57.

4. Hilgenfeldt, S., S. Erisken, and R.W. Carthew, *Physical modeling of cell geometric order in an epithelial tissue.* Proc Natl Acad Sci U S A, 2008. **105**(3): p. 907-11.

5. Gustafson, T. and L. Wolpert, *Cellular movement and contact in sea urchin morphogenesis.* Biol Rev Camb Philos Soc, 1967. **42**(3): p. 442-98.

6. Murray, J.D., *On pattern formation mechanisms for lepidopteran wing patterns and mammalian coat markings.* Philos Trans R Soc Lond B Biol Sci, 1981. **295**(1078): p. 473-96.

7. Theraulaz, G., et al., *The formation of spatial patterns in social insects: from simple behaviours to complex structures.* Philos Transact A Math Phys Eng Sci, 2003. **361**(1807): p. 1263-82.

8. Whitesides, G.M. and M. Boncheva, *Beyond molecules: self-assembly of mesoscopic and macroscopic components.* Proc Natl Acad Sci U S A, 2002. **99**(8): p. 4769-74.

9. Britten, R.J., *Underlying assumptions of developmental models.* Proc Natl Acad Sci U S A, 1998. **95**(16): p. 9372-7.

10. Risau, W. and I. Flamme, *Vasculogenesis.* Annu Rev Cell Dev Biol, 1995. **11**: p. 73-91.

11. Risau, W., *Mechanisms of angiogenesis.* Nature, 1997(386): p. 671-674.

12. le Noble, F., et al., *Flow regulates arterial-venous differentiation in the chick embryo yolk sac.* Development, 2004. **131**(2): p. 361-375.

13. Carmeliet, P. and R.K. Jain, *Angiogenesis in cancer and other diseases.* Nature, 2000. **407**(6801): p. 249-257.

14. Carmeliet, P., et al., *Abnormal blood vessel development and lethality in embryos lacking a single VEGF allele.* Nature, 1996. **380**(6573): p. 435-9.

15. Isogai, S., et al., *Angiogenic network formation in the developing vertebrate trunk.* Development, 2003. **130**(21): p. 5281-90.

16. Motoike, T., et al., *Universal GFP reporter for the study of vascular development.* Genesis, 2000. **28**(2): p. 75-81.

17. Drake, C.J. and C.D. Little, *Exogenous vascular endothelial growth factor induces malformed and hyperfused vessels during embryonic neovascularization.* Proc Natl Acad Sci U S A, 1995. **92**(17): p. 7657-61.

18. Coffin, J.D. and T.J. Poole, *Endothelial cell origin and migration in embryonic heart and cranial blood vessel development.* Anat Rec, 1991. **231**(3): p. 383-95.

19. Drake, C.J., et al., *VEGF regulates cell behavior during vasculogenesis.* Dev Biol, 2000. **224**(2): p. 178-88.

20. Haudenschild, F.a., *Angiogenesis in vitro.* Nature, 1980. **288**: p. 551-556.

21. Ng, C.P., C.L.E. Helm, and M.A. Swartz, *Interstitial flow differentially stimulates blood and lymphatic endothelial cell morphogenesis in vitro.* Microvascular Research, 2004. **68**(3): p. 258-264.

22. Davis, G.E., S.M. Black, and K.J. Bayless, *Capillary morphogenesis during human endothelial cell invasion of three-dimensional collagen matrices.* In Vitro Cell Dev Biol Anim, 2000. **36**(8): p. 513-9.

23. Tracqui, P. and J. Ohayon, *Transmission of mechanical stresses within the*

cytoskeleton of adherent cells: a theoretical analysis based on a multi-component cell model. Acta Biotheor, 2004. **52**(4): p. 323-41.

24. Tranqui, L. and P. Tracqui, *Mechanical signalling and angiogenesis. The integration of cell-extracellular matrix couplings.* C R Acad Sci III, 2000. **323**(1): p. 31-47.

25. Vailhe, B., et al., *In vitro angiogenesis is modulated by the mechanical properties of fibrin gels and is related to alpha(v)beta3 integrin localization.* In Vitro Cell Dev Biol Anim, 1997. **33**(10): p. 763-73.

26. Vailhe, B., et al., *The formation of tubular structures by endothelial cells is under the control of fibrinolysis and mechanical factors.* Angiogenesis, 1998. **2**(4): p. 331-44.

27. Coniglio, A., et al., *Percolation and Burgers' dynamics in a model of capillary formation.* Phys Rev E Stat Nonlin Soft Matter Phys, 2004. **69**(5 Pt 1): p. 051910.

28. Gamba, A., et al., *Percolation, morphogenesis, and burgers dynamics in blood vessels formation.* Phys Rev Lett, 2003. **90**(11): p. 118101.

29. Montesano, R., L. Orci, and P. Vassalli, *In vitro rapid organization of endothelial cells into capillary-like networks is promoted by collagen matrices.* J Cell Biol, 1983. **97**(5 Pt 1): p. 1648-52.

30. Namy, P., J. Ohayon, and P. Tracqui, *Critical conditions for pattern formation and in vitro tubulogenesis driven by cellular traction fields.* J Theor Biol, 2004. **227**(1): p. 103-20.

31. Serini, G., et al., *Modeling the early stages of vascular network assembly.* Embo J, 2003. **22**(8): p. 1771-9.

32. Davis, G.E., W. Koh, and A.N. Stratman, *Mechanisms controlling human endothelial lumen formation and tube assembly in three-dimensional extracellular matrices.* Birth Defects Res C Embryo Today, 2007. **81**(4): p. 270-85.

33. Choi, N.W., et al., *Microfluidic scaffolds for tissue engineering.* Nat Mater, 2007. **6**(11): p. 908-15.

34. Helmlinger, G., et al., *Formation of endothelial cell networks.* Nature, 2000. **405**(6783): p. 139-41.

35. Little, C.J.D.a.C.D., *The Morphogenesis of Primordial Vascular Networks*, in *Vascular Morphogenesis: In vivo, In vitro, In mente.* M. Little, and Sage, Editor. 1998: Charleston, SC. p. 3-19.

36. Shing, Y., et al., *Angiogenesis is stimulated by a tumor-derived endothelial cell growth factor.* J Cell Biochem, 1985. **29**(4): p. 275-87.

37. Pepper, M.S., et al., *Transforming growth factor-beta 1 modulates basic fibroblast growth factor-induced proteolytic and angiogenic properties of endothelial cells in vitro.* J Cell Biol, 1990. **111**(2): p. 743-55.

38. Ferrara, N., K.J. Hillan, and W. Novotny, *Bevacizumab (Avastin), a humanized anti-VEGF monoclonal antibody for cancer therapy.* Biochem Biophys Res Commun, 2005. **333**(2): p. 328-35.

39. Zisch, A.H., et al., *Covalently conjugated VEGF--fibrin matrices for endothelialization.* J Control Release, 2001. **72**(1-3): p. 101-13.

40. Gerhardt, H., et al., *VEGF guides angiogenic sprouting utilizing endothelial tip cell filopodia.* J Cell Biol, 2003. **161**(6): p. 1163-77.

41. Murphy, G. and J. Gavrilovic, *Proteolysis and cell migration: creating a path?* Curr Opin Cell Biol, 1999. **11**(5): p. 614-21.

42. Friedl, P. and E.B. Brocker, *The biology of cell locomotion within three-dimensional extracellular matrix.* Cell Mol Life Sci, 2000. **57**(1): p. 41-64.

43. Ingber, D., *Mechanical and Chemical Determinants of Tissue Development*, in *Principles of Tissue Engineering*. 2000, Academic Press, Inc.: San Diego, CA. p. 101-110.

44. Davis, G.E. and C.W. Camarillo, *Regulation of Endothelial-Cell Morphogenesis by Integrins, Mechanical Forces, and Matrix Guidance Pathways.* Experimental Cell Research, 1995. **216**(1): p. 113-123.

45. Sieminski, A.L., R.P. Hebbel, and K.J. Gooch, *The relative magnitudes of endothelial force generation and matrix stiffness modulate capillary morphogenesis in vitro.* Exp Cell Res, 2004. **297**(2): p. 574-84.

46. Davis, G.E. and C.W. Camarillo, *The Alpha-6-Beta-1 Integrin and Mechanical Tension Regulate Endothelial Tube Formation on Basement-Membrane Matirx.* Journal of Cellular Biochemistry, 1994: p. 248-248.

47. Ingber, D.E., *Mechanical signaling and the cellular response to extracellular matrix in angiogenesis and cardiovascular physiology.* Circ Res, 2002. **91**(10): p. 877-87.

48. Korff, T. and H.G. Augustin, *Tensional forces in fibrillar extracellular matrices control directional capillary sprouting.* Journal of Cell Science, 1999. **112**(19): p. 3249-3258.

49. Lo, C.M., et al., *Cell movement is guided by the rigidity of the substrate.* Biophys J, 2000. **79**(1): p. 144-52.

50. Reinhart-King, C.A., M. Dembo, and D.A. Hammer, *Cell-cell mechanical communication through compliant substrates.* Biophysical Journal, 2008. **95**(12): p. 6044-51.

51. Park, J.E., G.A. Keller, and N. Ferrara, *The vascular endothelial growth factor (VEGF) isoforms: differential deposition into the subepithelial extracellular matrix and bioactivity of extracellular matrix-bound VEGF.* Mol Biol Cell, 1993. **4**(12): p. 1317-26.

52. Manoussaki, D., et al., *A mechanical model for the formation of vascular networks in vitro.* Acta Biotheoretica, 1996. **44**(3-4): p. 271-282.

53. Murray, J.D., G.F. Oster, and A.K. Harris, *A mechanical model for mesenchymal morphogenesis.* J Math Biol, 1983. **17**(1): p. 125-9.

54. Harris, A.K., P. Wild, and D. Stopak, *Silicone rubber substrata: a new wrinkle in the study of cell locomotion.* Science, 1980. **208**(4440): p. 177-9.

55. Murray, J.D. and G.F. Oster, *Cell traction models for generating pattern and form in morphogenesis.* J Math Biol, 1984. **19**(3): p. 265-79.

56. Chicurel, M.E., C.S. Chen, and D.E. Ingber, *Cellular control lies in the balance of forces.* Curr Opin Cell Biol, 1998. **10**(2): p. 232-9.

57. Bischofs, I.B., S.A. Safran, and U.S. Schwarz, *Elastic interactions of active cells with soft materials.* Phys Rev E Stat Nonlin Soft Matter Phys, 2004. **69**(2 Pt 1): p. 021911.

58. Bischofs, I.B. and U.S. Schwarz, *Collective effects in cellular structure formation mediated by compliant environments: a Monte Carlo study.* Acta Biomater, 2006. **2**(3): p. 253-65.

59. le Noble, F.A.C., A. Eichmann, and V. Fleury, *Flow controls embryonic arterial venous differentiation and branching morphogenesis through novel shear evoked events: vessel disconnection and guidance of vessel sprouts.* Hypertension, 2004. **44**(4): p. 570-570.

60. Chang, S.C.N., et al., *Injection molding of chondrocyte/alginate constructs in the shape of facial implants.* Journal of Biomedical Materials Research, 2001. **55**(4): p. 503-511.

61. Davis, M.W. and J.P. Vacanti, *Toward development of an implantable tissue engineered liver.* Biomaterials, 1996. **17**(3): p. 365-372.

62. Vernon, R.B., et al., *Microgrooved fibrillar collagen membranes as scaffolds for cell support and alignment.* Biomaterials, 2005. **26**(16): p. 3131-3140.

63. Cabodi, M., et al., *A microfluidic biomaterial.* Journal of the American Chemical Society, 2005. **127**(40): p. 13788-13789.

64. Tan, W. and T.A. Desai, *Layer-by-layer microfluidics for biomimetic three-dimensional structures.* Biomaterials, 2004. **25**(7-8): p. 1355-1364.

65. Bellan, L.M., et al., *Fabrication of an artificial 3-dimensional vascular network using sacrificial sugar structures.* Soft Matter, 2009. **5**(7): p. 1354-1357.

66. Hotary, K., et al., *Regulation of cell invasion and morphogenesis in a three-dimensional type I collagen matrix by membrane-type matrix metalloproteinases 1, 2, and 3.* J Cell Biol, 2000. **149**(6): p. 1309-23.

67. Gelman, R.A., B.R. Williams, and K.A. Piez, *Collagen Fibril Formation - Evidence for a Multistep Process.* Journal of Biological Chemistry, 1979. **254**(1): p. 180-186.

68. Davis, G.E. and D.R. Senger, *Endothelial extracellular matrix - Biosynthesis, remodeling, and functions during vascular morphogenesis and neovessel stabilization.* Circulation Research, 2005. **97**(11): p. 1093-1107.

69. Ng, C.P. and M.A. Swartz, *Fibroblast alignment under interstitial fluid flow using a novel 3-D tissue culture model.* American Journal of Physiology-Heart and Circulatory Physiology, 2003. **284**(5): p. H1771-H1777.

70. Enever, P.A.J., D.I. Shreiber, and R.T. Tranquillo, *A novel implantable collagen gel assay for fibroblast traction and proliferation during wound healing.* Journal of Surgical Research, 2002. **105**(2): p. 160-172.

CHAPTER 2

DENSE TYPE I COLLAGEN AS A 3-D SCAFFOLD FOR VASCULAR BIOLOGY

2-1 Introduction

Native type I collagen is a natural substrate for cell adhesion and growth and is remodelable by many tissue cells, making it an ideal material for the study of dynamic cellular processes. Hydrated collagen matrices are commonly used for *in vitro* three-dimensional (3-D) cell culture scaffolds; however, the low mass fraction of collagen typically used (1.0-3.0 mg/ml) results in an extremely low elastic modulus gel. In addition, the degradation rate of these low mass fraction collagen matrices is rapid, making long-term 3-D cell culture difficult. A more mechanically robust, higher mass fraction, native type I collagen matrix would allow one to handle, define a shape, and even microfabricate the material, making it more versatile and functional. In addition it would be a more suitable material for tumor biology and angiogenesis studies as the collagen concentration in tumor tissue is an order of magnitude greater than that used in the conventional 3-D collagen cell culture scaffolds.

In this chapter, I give an overview of the historical uses of collagen and other natural materials used for 3-D cell culture scaffolds. Then I will describe our methods for preparing dense collagen matrices, and I will report upon the physical and mechanical properties of the dense type I collagen matrices (up to a collagen concentration of 20 mg/ml). Furthermore, I discuss and show results for 1) the remodelability of the dense collagen by human umbilical vein endothelial cells (HUVECs), 2) our preliminary *in vitro* tumor angiogenesis model, and 3) our methods used to fabricate a functional microfluidic network within a 10 mg/ml (1%) collagen matrix. Finally I discuss the implications and ongoing work of integrating microfluidic control within these collagen scaffolds as a tool to study spatial and

temporal signaling during tumor angiogenesis and vascularization of tissue engineered constructs.

2-2 Three dimensional cell culture

Three dimensional (3-D) scaffolds have been used for developing functional tissues for regenerative medicine [2-5], studying basic tissue scale biology [6-8], and studying 3-D tissue development [9]. The creation and characterization of *in vitro* 3-D microenvironments have been a focus in the vascular cell biology community towards the effort to mimic the *in vivo* microenvironment of cells. We are interested in 3-D scaffolds for use in endothelial cell (EC) biology, specifically EC network formation and invasion [10] as well as tumor angiogenesis[11].

As related to our primary interest in vascular biology studies, 3-D scaffolds have been used to study the mechanisms of tumor metastasis[12], chemical signaling during tumor angiogenesis[13, 14], and the vascularization of tissue engineered implants[15, 16]. The extracellular matrix (ECM) chemistry and mechanics significantly influence cell differentiation, proliferation, migration, shape, cell-cell communication, biosynthetic activity, and tissue morphogenesis [11, 17-22]. Mimicking the *in vivo* ECM is challenging because it is not trivial to incorporate micro-scale physiological details without compromising cellular remodelability of the material.

Besides type I collagen, there are many different types of natural and synthetic materials used for 3-D cell culture. Table 2-1 lists a number of natural materials used for 3-D cell culture. Previously, our lab has created a microfluidic network within calcium alginate hydrogels to spatially and temporally control the delivery of signaling factors to cells [23]. This enabling tool has advanced 3-D cell culture scaffolds capabilities; however, the calcium alginate is not remodelable by tissue cells. Therefore, we have focused on developing a similar technology in type I collagen

matrices. In the follow section, I describe a number of different types of collagen scaffolds from the literature and how they have been used.

Table 2-1. Natural materials that are commonly used for 3-D cell culture

Material	Source
Calcium alginate[24] [25]	seaweed (cell walls of brown algae)
Matrigel [26, 27]	basement membrane from mouse sarcoma
Type IV collagen [28]	component of basement membrane
Agarose [29]	polysaccharide from algae cell walls
Agarose-gelatin[30]	mixture of agarose and denatured collagen
Fibrin[16, 31, 32]	fibrillar protein made from fibrinogen.
Elastin[33]	fibrillar protein in ECM
Chitosan[34]	from chitin (arthropod exoskeletons)
Hyaluronic Acid[35]	glycosaminolglycan (GAG) in mammalian tissue and fluid

2-3 Historical preparations and applications of type I collagen

Collagen is abundant, cheap and has been used extensively in many different forms for cell culture and tissue engineering applications for many years [36, 37]. The size and shape of the collagen molecule in solution is well elucidated [36, 38, 39]. The primary building block of native collagen is the tropocollagen molecule, a rod-like particle ~280 nm in length, 1.5 nm in diameter and of a molecular weight of 300,000 Da. The tropocollagen is composed of three left-handed helix polypeptide chains which wrap around each other to form a right-handed helix which is the native fibril. These fibers further aggregate to form larger bundles of fibers.

Collagen is commonly used in its native form; however, many different cross-linking and other denaturing processes have been used to change the mechanical properties of the scaffold, control the microstructure or macroscopic shape, or provide

additional binding sites (like RGD) or signaling cues for cells. When collagen is denatured, it is called gelatin [28, 40]. The denaturing process causes the helixes to unwind and depending on the degree of denaturation, the specific peptide motifs may or may not remain intact. This degree of denaturation depends on the severity of the denaturing method, for example, whether it is heated, dried, or chemically altered.

Elsdale and Bard were pioneers in reporting a method to produce a cell-embedded native collagen gels which they called a hydrated collagen lattice (HCL) [37]. Soon thereafter, Piez et al. began the primary investigation of collagen structure and fibril formation [36, 41]. Since then, further characterization of the mechanical [1, 42, 43] and structural properties of native collagen gels has been performed [44].

There have been developments towards using type I collagen for tissue engineered substitutes; however, as I mentioned previously, a drawback to using native collagen gels for tissue engineering applications is the weak mechanical properties of the material. Contraction of the gel by constituent cells is significant, and its fragility makes molding constructs into desired shapes nearly impossible. Due to these limitations, crosslinking methods have been used to alter collagen scaffolds, and many have performed both chemical and mechanical modifications of collagen by addition of glycosaminoglycans (GAGs), fibrin, and other materials [42, 45-47]. Crosslinked collagen-GAG coprecipitates have been used to create collagen membranes for skin tissue engineering [45] and as membranes for cell support with perfusion [48]. Dehydrothermal cross-linking (severe dehydration) of collagen-GAG coprecipitates have been performed to create collagen fibers for tendon reconstruction[49] and scaffolds for cartilage tissue engineering[50].

Despite the weak mechanical properties of native collagen gels, they are being used extensively for specific applications. Nerve[51] and heart muscle repair [52], vascular invasion and vasculogenesis assays [53-55], fibroblasts and gel contraction

assays [56], and tumor biology studies[57] are all being carried out in conventional low concentration native type I collagen gels.

High concentration collagen scaffolds have been made via centrifugation [58] and evaporation methods [59] for studies related to diffusion and transport in tumors and fibroblast traction and migration, respectively. These higher concentration collagen scaffolds have been shown to hold microstructure and have been used to study perfusion across an endothelial cell-lined microchannel [60, 61]. A variety of methods of microfabrication of 3-D structures in soft materials have been described [62]. Specifically, Bissell et al. have developed a micromolding method to construct 3-D microscale cavities in type I collagen gels [9].

2-4 Preparation of hydrated, native, dense collagen scaffolds

High weight percent native collagen matrices are not typically used and have not been well characterized (either cellularly or mechanically). We believe a dense, native collagen matrix would be an ideal substrate for vascular biology studies and an innovative new microfluidic biomaterial. In this section, I will describe our methods for preparing dense collagen matrices.

To prepare the dense collagen scaffolds, collagen was extracted from rat tails [63, 64] as described in Appendix A-4. The acidic collagen solution was then lyophilized, and the dry mass was determined. The collagen was resuspended in 0.1% acetic acid at four different stock solution concentrations: 8mg/ml, 15 mg/ml, 20 mg/ml, and 30 mg/ml. Resuspension of the high mass fraction stock solutions were agitated daily to aid in dissolving. After 3 days in solution, the majority of the collagen was dissolved; however, a clump of undissolved collagen (seen as an opaque mass) remained in the center of the solution. After 5 days in solution (with agitation), the thick collagen solution was uniform and clear and free from visible opaque collagen masses. These collagen stock solutions were used for all experiments and results presented.

We performed SDS-PAGE on multiple collagen solutions (Figure 2-1) to verify that we retained collagen monomers after lyophilization and resuspension in acetic acid. By running purchased rat tail type I collagen (BD Biosciences) alongside our collagen preparations, we could compare our collagen with the collagen used by most other researchers. In Figure 2-1, lane 2 shows the protein separation of the purchased type I collagen from BD Biosciences. Lanes 3, 4, and 5 are collagen preparations that had been lyophilized and resuspended to 30mg/ml or 15 mg/ml in acetic acid. We can see that the separations in all of these lanes look similar. To verify that lyophilization process didn't change the collagen structures, we ran an acidic collagen solution that had not been lyophilized in lane 6. We see that there are numerous bands in all of the lanes; however, there appears to be the same bands in each lane. We point out the

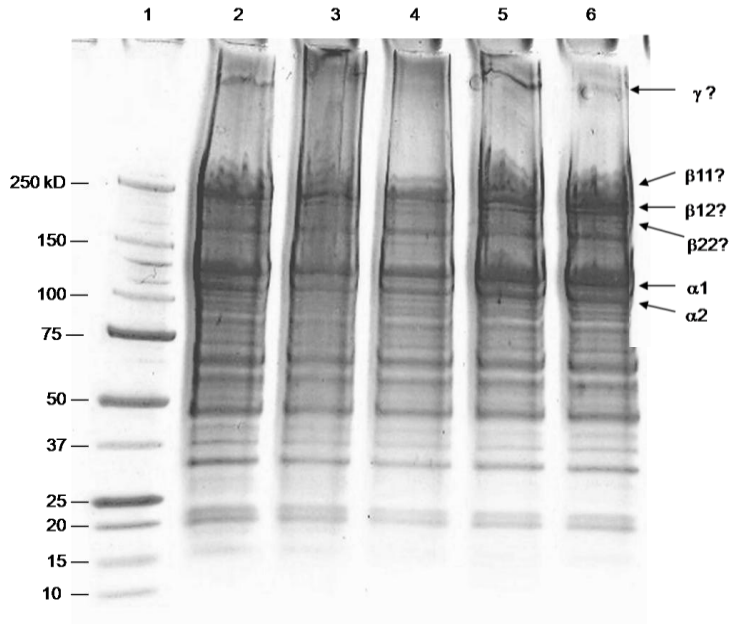

Figure 2-1. SDS-PAGE of multiple collagen solutions on a 4-15% gradient Tris-HCl Ready Gel (Biorad). ~ 53 µg protein/lane. *Lane 1*: Precision Plus Protein Standard, *Lane 2:* BD Bioscience type I rat tail collagen, *Lane 3*: 30mg/ml lyophilized/ resuspended stock, *Lane 4*: 30 mg/ml lyophilized/resuspended stock, *Lane 5*: 15 mg/ml lyophilized/resuspended stock, *Lane 6*: 4.7 mg/ml stock (never lyophilized).

presence of bands at ~ 120 and 130 kDa which are the approximate sizes of the α2 and α1 helices, respectively. The collagen molecule contains one, α2 helix and two, α1 helices which explains the darker α1 band. We also see significant bands at ~240-250 kDa, which may represent a collagen molecule that has been incompletely denatured and contains two α helices. These bands are labeled as β12, β11, or β22. Finally we label a γ band near the top of the gel which may be the full 300 kDa collagen molecule due to incomplete degradation.

2-5 Fluorescently labeling collagen fibers

To visualize collagen fibers with confocal fluorescence microscopy and to analyze a collagen gel's structural properties, tetramethylrhodamine isothiocyanate (TRITC)-labeled collagen was prepared by reacting pure collagen with TRITC following a standard labeling protocol [65]. Specifically, dry collagen (extracted from rat tails and centrifuged as described in Appendix A-4) was resuspended at 20 mg/ml in 0.1M sodium bicarbonate buffer at pH 9.0 by agitating for 8 hours at 4°C. A 10mg/ml TRITC solution in DMSO was added to the collagen at a molar ratio of 3:1, dye: protein [65] and was then agitated at 4°C for 24 hours in the dark. Free dye molecules were removed using dialysis in 0.1% acetic acid for at least 72 hours in the dark at 4°C using dialysis tubing with a pore size of MWCO 25,000. The labeled collagen was kept at 4°C in the dark until used.

2-6 Structural analysis

Confocal fluorescence and reflectance microscopy of the TRITC-labeled collagen were both performed on unfixed, hydrated samples (Fig 2-2). Confocal reflectance microcopy requires no staining and collects the back-scattered light from the collagen fibers [66]. We used our fluorescently labeled collagen fibers [65] to directly compare the resolution of the two visualization methods, and we collected the reflected light and the fluorescence channel simultaneously on the same sample

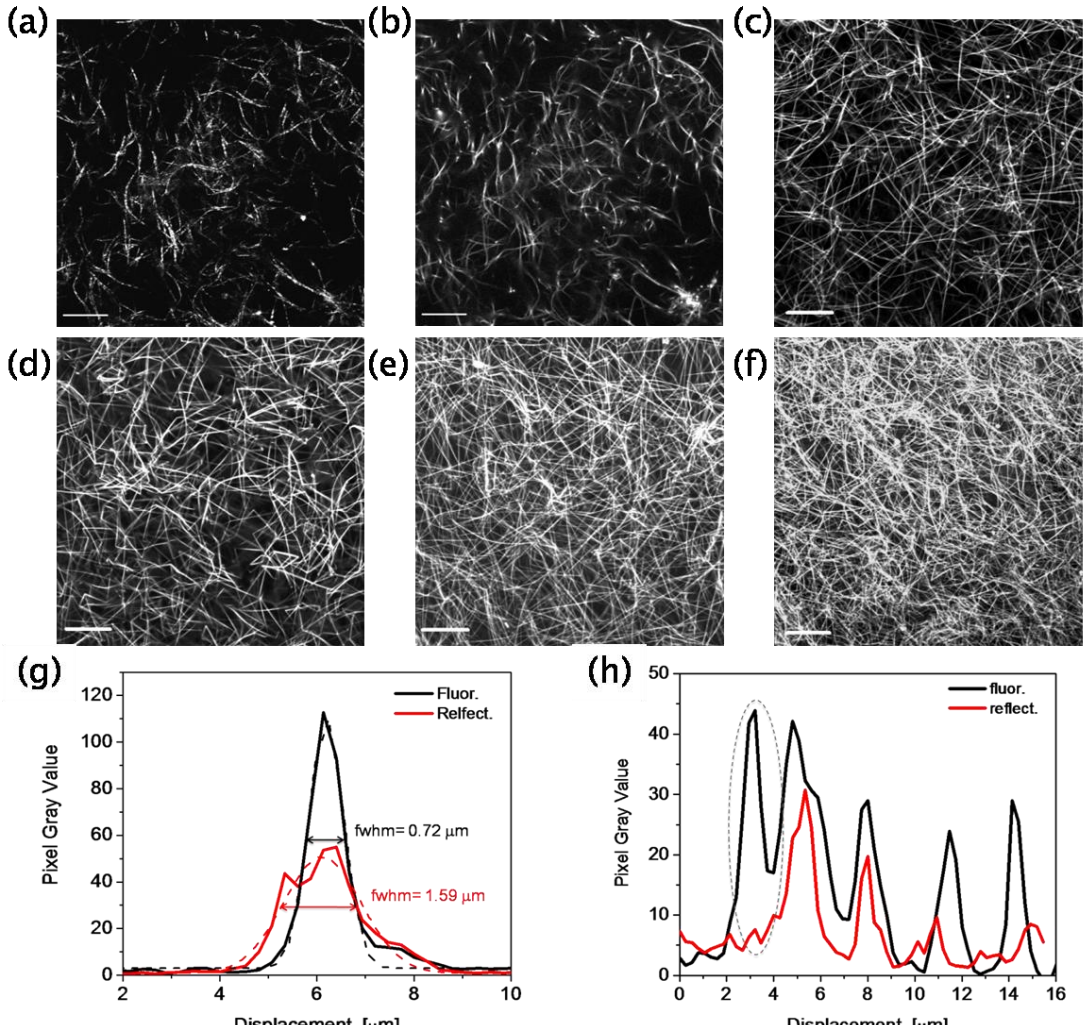

Figure 2-2. Reflectance (a) and fluorescent (b-f) confocal images of TRITC-labeled collagen fibers at collagen concentrations of 3 mg/ml (a, b), 8 mg/ml (c), 10 mg/ml (d), 15 mg/ml (e), and 20 mg/ml (f). Images are a single plane in a hydrated collagen gel using a 63x 1.4 NA oil immersion lens with pinhole = 1 Airy unit. Scale bars = 20 microns. (g) Quantification of the resolution of reflectance and fluorescence images in (a) and (b) with a single fiber line scan. (h) Linescan across five essentially parallel fibers at the same location in images (a) and (b). The dotted oval over the first peak indicates the absence of a peak in the reflectance image when a collagen fiber is present and can be detected in the fluorescent image.

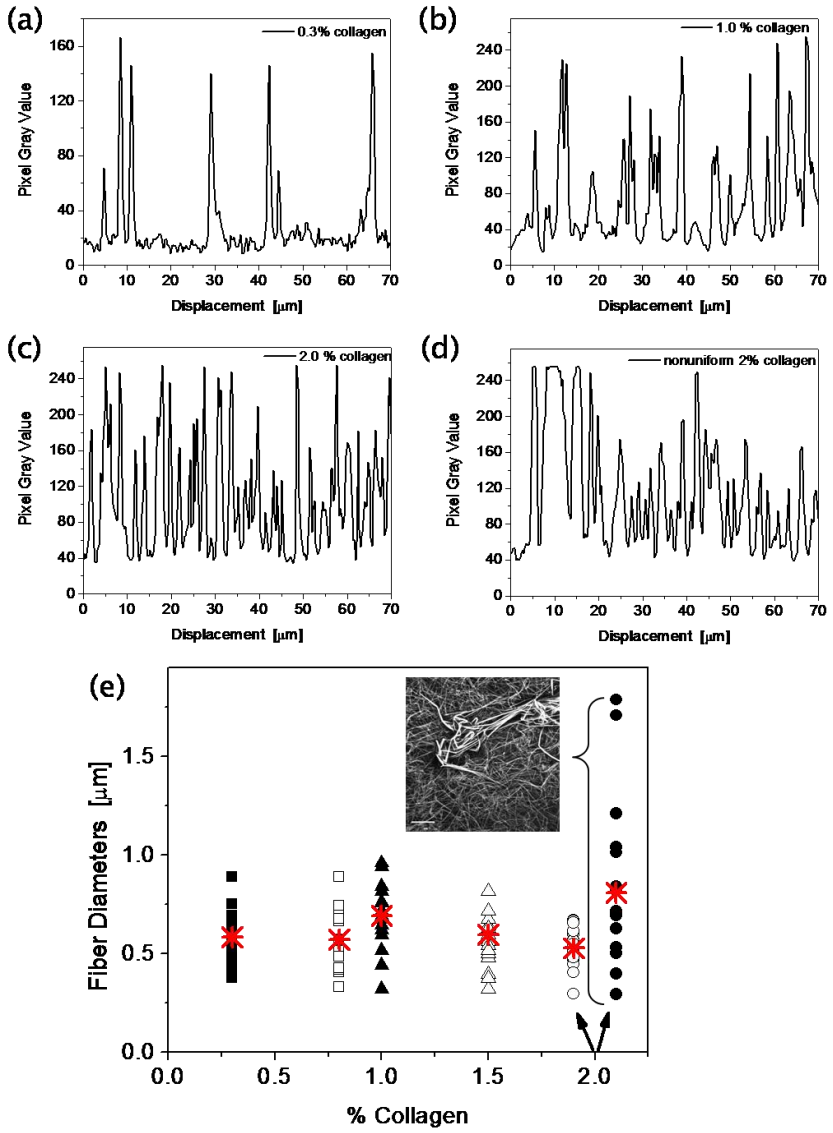

Figure 2-3. Collagen fiber density and diameter analysis. Representative line scans across a 70 μm length of confocal fluorescence images in Figure 1 for 0.3% collagen (a), 1.0% collagen (b), 2.0% collagen (c), and a non-uniform 2.0% collagen gel (d). (e) Summary of single fiber linescans used to determine the average fiber diameter (red cross point) for all collagen concentrations and a non-uniform 2.0% collagen gel (inset image). n= 120.

(Figure 2-2a and 2-2b). Line scans across the same fibers in the reflectance (Figure 2-2a) and fluorescence (2-2b) were performed and the full width at half maximum was determined by fitting to a Gaussian distribution (Figure 2-2g). Fluorescence shows better detail in resolution. Using line scans across small sections from Figure 2-2a and 2-2b, it is apparent that more fibers are visible in the fluorescent images (dotted circle in Figure 2-2h); thus fluorescence shows better sensitivity than reflectance.

70 μm line scans across the images (~ perpendicular to fibers) in Figure 2-2 are shown in Figure 2-3 a-d, and single fiber diameters were measured using Image J software (Figure 2-3e). Based on these measurements, the average fiber diameter in well- mixed collagen gels at all concentrations is ~ 500 μm (Figure 2-3e). This measured diameter is probably not set by the point-spread function (psf) of the objective since the 63x, 1.4NA oil objective used in confocal mode with a pinhole of 1 Airy unit has a higher resolution than 500 μm. It is interesting both mechanically and biologically that the fiber diameter does not depend on collagen concentration. This constant fiber diameter indicates that the stronger mechanical properties of denser collagen gels (described in the next section) is due to the meshwork and collective physical gel rather than the properties of the individual fibers. Notice that if the high concentration collagen is inadequately mixed or if the lyophilized collagen had not been completely dissolved (<5 days in acetic acid) (Figure 2-3e inset) the fiber size is inhomogeneous and large fibers exist.

Based on measurements from the images in Figure 2-2b-f, we calculate the average pore radius to range from ~1 μm to ~15μm. Extracting quantitative measurements of pore size based on a 2-D plane of a 3D filamentous network is not trivial[67]. Our 2-D estimate is may be somewhat unreliable due to the fact that the pores have interconnected irregular shapes rather than discrete voids, and thus, the definition of a single pore is subjective.

2-7 Mechanical properties of dense collagen scaffolds

We use confined compression to characterize the mechanical properties of collagen gels. Transient compression-stress relaxation experiments were performed on hydrated acellular collagen gels. Collagen disks 2 mm thick and 8 mm in diameter were made using a PDMS mold. Gels with a final concentration of 3, 8, 10, 15, and 20 mg/ml were made from concentrated collagen stock solutions of 8, 10, 20, 20, and 30 mg/ml, respectively. Acidic collagen stock solution was diluted to the desired final collagen concentration while on ice by the addition of 0.1 volume fraction (with respect to the final volume of solution) of 10x concentrated Medium 199 and the amount of 1x Medium 199 to obtain the required final volume (See Appendix A-5 for an example formulation). The solution was titrated to neutral pH with the addition of 1N NaOH and mixed on ice. Neutralized collagen solution was immediately placed in the PDMS mold and was allowed to polymerize at 37 °C at 5% CO_2 for 20 minutes. By submerging the entire PDMS mold in phosphate buffered saline (PBS) and peeling the PDMS free from the collagen, gels simply floated off the mold into PBS without direct physical contact to the collagen. Because the low concentration collagen gels are extremely fragile and can collapse upon touching, gentle handling of the collagen discs was crucial to maintain the integrity of the gels. Gels were mechanically tested within 24 hours of polymerization.

The compression-stress relaxation experiments were done with an Enduratec ELF-3200 test system (Bose EnduraTEC, Minnetonka, MN) using a 250-g load cell (Honeywell Sensotec, Columbus, OH). See Appendix A-8 for our testing protocol. Briefly, the collagen discs were placed in an impermeable cup with the same dimensions as the sample resulting in radially-confined compression. A polyethylene porous plug was placed on the submerged sample, and the displacement actuator was brought into contact with the porous plug. As load was applied to the sample, PBS

could only exit through the porous plug. Gels were compressed in increments of 3% strain up to 30% strain. After each 3% compression, the sample thickness was held constant for 20 minutes until the stress relaxed to a new equilibrium (Figure 2-4).

Using a custom MATLAB(The Mathworks, Natick, MA) code developed by the Bonassar Lab at Cornell, stress relaxation data (example in Figure 2-4) was fit to a

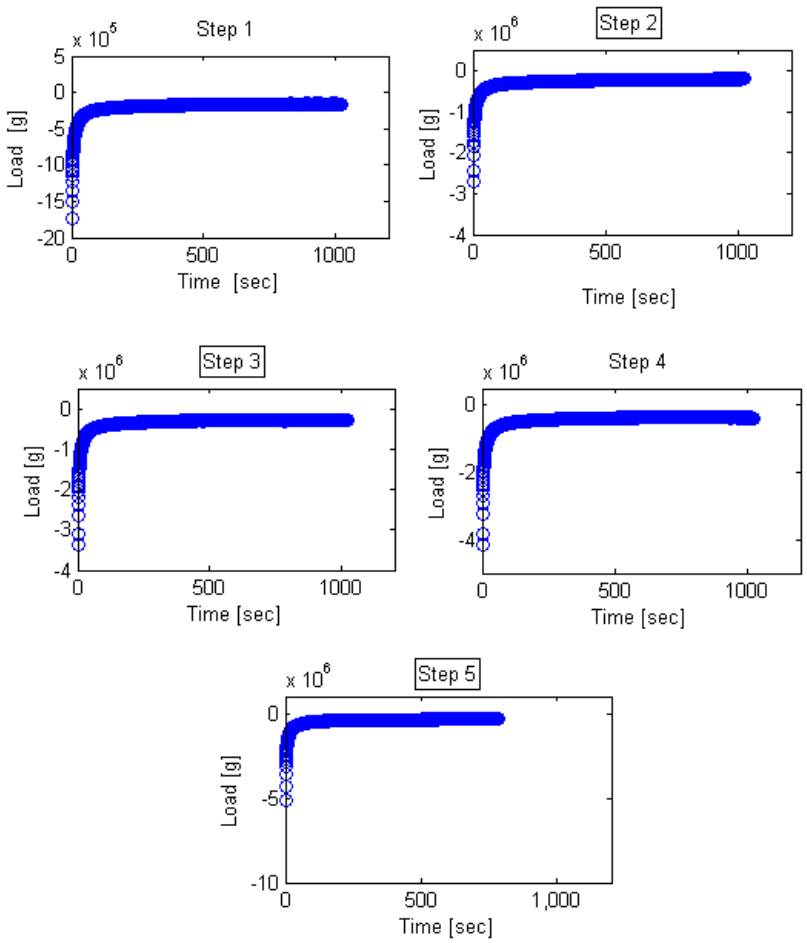

Figure 2-4. Raw data of confined compression stress-relaxation experiment. Gels were compressed in increments of 3% strain up to 30% strain. After each compression step, the sample was allowed to relax for ~ 20 minutes (until equilibrium was reached). Note the change in scale on the y axis.

poroelastic model of material behavior using the equation:

$$\sigma_{eq} = A\left(1 - e^{t/\tau}\right) + B \qquad [1]$$

where $A + B$ is the equilibrium stress [Pa] and B is the instantaneous stress [Pa], t is time [s], and τ [$1/s$] is the exponential time constant[68]. We make the assumption, following others [1] that the gel matrix responds like an isotropic, elastic material. The transient stress relaxation and final equilibrium stress data were recorded and an equilibrium stress-strain curve was generated for each sample (Figure 2-5).

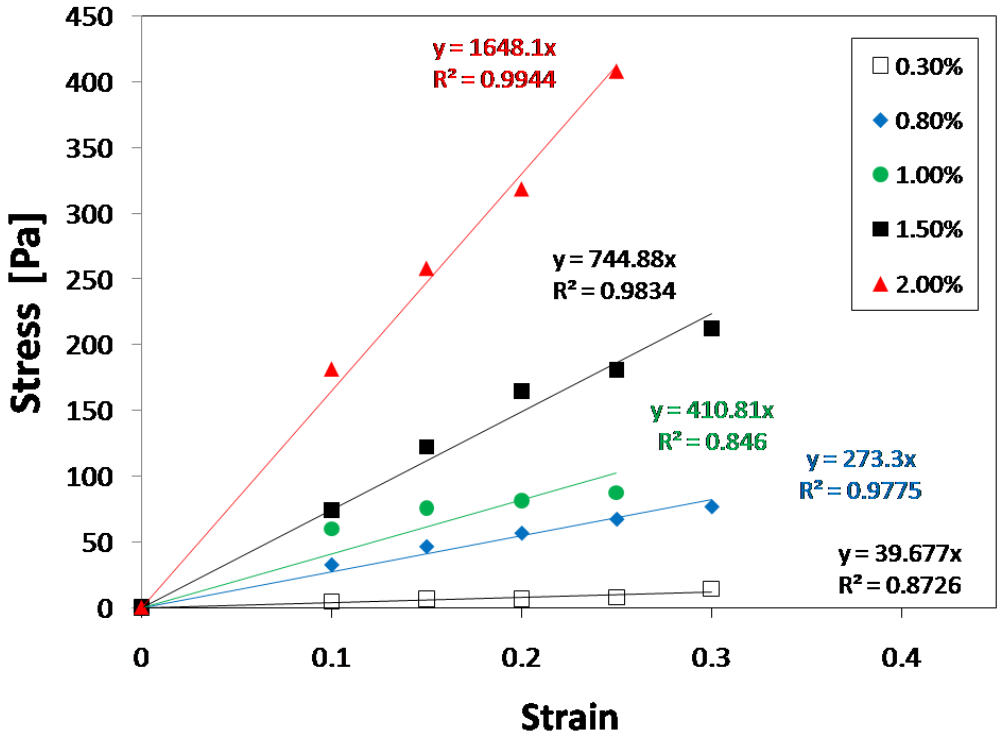

Figure 2-5. Example of equilibrium stress versus compressive strain for a single sample at each collagen concentration.

The longitudinal equilibrium modulus, M_{eq} [Pa] was calculated from the slope of the stress-strain curve. Note that this equilibrium modulus is related to the shear modulus, G, the Young's modulus, E, and the Poisson's ratio, η by the following

expressions[69]:

$$\eta = \frac{3M_{eq} - 2G}{6M_{eq} + 2G} \quad [2]$$

$$E = 2G(1+\eta) \quad [3]$$

The transient relaxation data was used to calculate the hydraulic permeability where,

$$\tau = \frac{\delta^2}{\pi^2 * \mathrm{M}_{eq} * k} \quad [4]$$

where δ [*m*] is the thickness of the sample, and, *k* [m^2/Pa*s] is the hydraulic permeability[1]. 3-5 collagen discs were tested for each collagen concentration. Each sample was compressed to 30% strain only once. A summary of the mechanical testing results can be found in Figure 2-6. Here we can see that there is a significant increase in modulus from 0.3% to 2.0% collagen and that permeability decreases exponentially with concentration over three decades (Figure 2-6b).

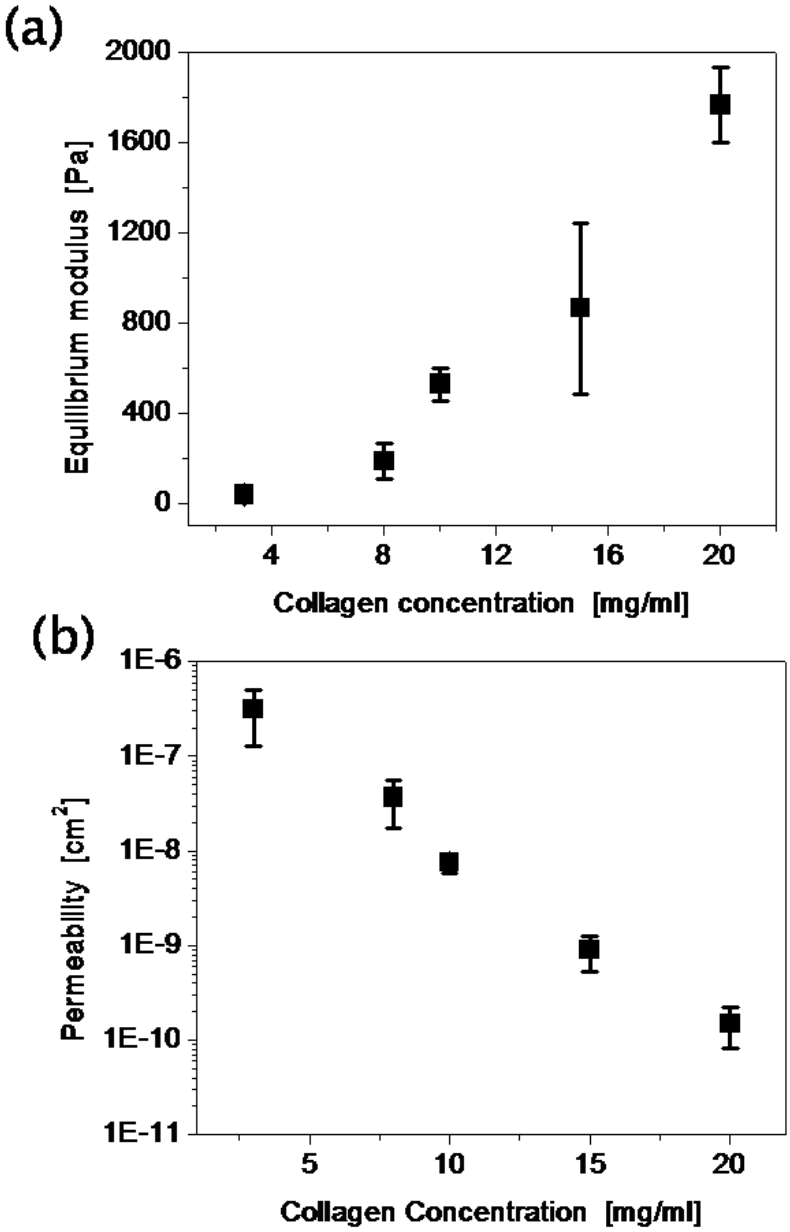

Figure 2-6. Equilibrium modulus (a) and specific permeability (b) versus collagen concentration. Error bars represent the 95% confidence intervals from three samples compressed in increments of ~ 3% strain up to ~ 30% strain. Note logarithmic scale in (b). The permeability was obtained from the measured stress relaxation time constant and the equilibrium modulus, following reference [1].

2-8 Hydraulic radius calculations

The confined compression testing allowed us to measure the hydraulic permeability (Figure 2-6b), so we use the Carman-Kozeny equation to relate the hydraulic permeability, *k,* and the mean hydraulic radius, r_H (reported in Table 2-1) as described by [70]:

$$k = \varepsilon * r_H^2 / k_{geo} \quad [3]$$

where $\varepsilon = (1-\phi)$ is the porosity, where ϕ is the volume fraction of collagen, and k_{geo} is a geometric factor which depends on the tortuosity. The geometric factor is separated in its parallel and normal components with respect to flow coordinates. For cylinders (which in our case represent fibers) perpendicular to the flow,

$$k_{\parallel} = 2\varepsilon^3 * \left\{(1-\varepsilon) * \left[\ln\left(1/1-\varepsilon\right) - 3 + 4*(1-\varepsilon) - (1-\varepsilon)^2\right]\right\} \quad [4]$$

and for cylinders (fibers) parallel to the flow,

$$k_{\perp} = 2\varepsilon^3 * \left\{(1-\varepsilon) * \left[\ln\left(1/1-\varepsilon\right) - (1-(1-\varepsilon))^2/(1+(1-\varepsilon)^2)\right]\right\} \quad [5]$$

For cylinders (fibers) oriented randomly in 3-D the geometric factor is given by,

$$k_{geo} = (2k_{\perp} + k_{\parallel})/3 \quad [6]$$

Table 2-2. Hydraulic pore radius, r_H was calculated using Carman-Kozeny model(Eq. 3) [70, 71]. The geometric factor, k_{geo}, depends on the channel shape and the tortuosity. The average pore radius, *a,* was measured using confocal images of a single plane of fluorescently labeled fibers.

Collagen[mg/ml]	volume fraction, ϕ	porosity, ε	k ∥	k ⊥	k_{geo}	r_H [μm]	a [μm]	stdev (a)
3.0	0.006	0.994	157.965	83.1	108.1	58.7	14.5	3.7
8.0	0.015	0.985	100.932	39.6	60.0	15.0	9.5	4.3
10.0	0.019	0.981	95.736	33.7	54.3	6.5	7.1	1.9
15.0	0.028	0.972	95.772	25.2	48.7	2.0	2.2	0.7
20.0	0.038	0.962	110.847	20.7	50.7	0.9	1.1	0.5

We calculate the hydraulic pore radius and compare to our 2-D pore size estimate based on image analysis (Table 2-2). The model treats the gel as an array of cylinders (which are fibers in our case) assumed to be randomly oriented in 3-D. The geometric factor (Table 2-2) calculated for randomly oriented cylinders in 3-D is a function of the material's tortuosity. The porosity is related to the volume fraction, ϕ, of collagen by $\varepsilon = 1-\phi$, where ϕ is the collagen concentration multiplied by the effective specific volume of collagen (protein + bound water), previously reported in [72].

Note that the two measures of structure (r_H and a) very different for low mass fractions (Table 2-2). Our 2-D pore estimation from image analysis gives a much smaller estimate of pore diameter. As mentioned above, extracting quantitative measurements of pore size based on a 2-D plane of a 3-D filamentous network is not trivial[67]. Our 2-D estimate is may be low due to the fact that the pores have interconnected irregular shapes rather than discrete voids, and the definition of a single pore is subjective.

2-9 Pore replication

To determine the lower limit of collagen concentration that can retain microstructure, we replicated micro pores in collagen concentrations of 0.15%, 0.3%, 0.6% and 1.0%. Soft lithography [73] was used to generate a PDMS stamp as a master on which to pattern collagen with microstructure[23]. Specifically, a layer of SU8-2100 (Microchem Corp.) was spun, exposed, and developed to generate a mold of 400 μm height pore structure with a diameter of 50, μm. (poly)-dimethylsiloxane (PDMS) (Sylgard® 184, Dow Corning, Midland, Michigan) was molded over the SU8 structures, and arrays of PDMS pillars were replicated with various diameters and 400 μm height. A PDMS overlayer with cylindrical wells coinciding with the PDMS

pillars was treated with 1% poly(ethyleneimine) (PEI) solution for 10 minutes followed by 0.1% glutaraldehyde for 30 minutes. This treatment made the PDMS. overlayer adherent to collagen.

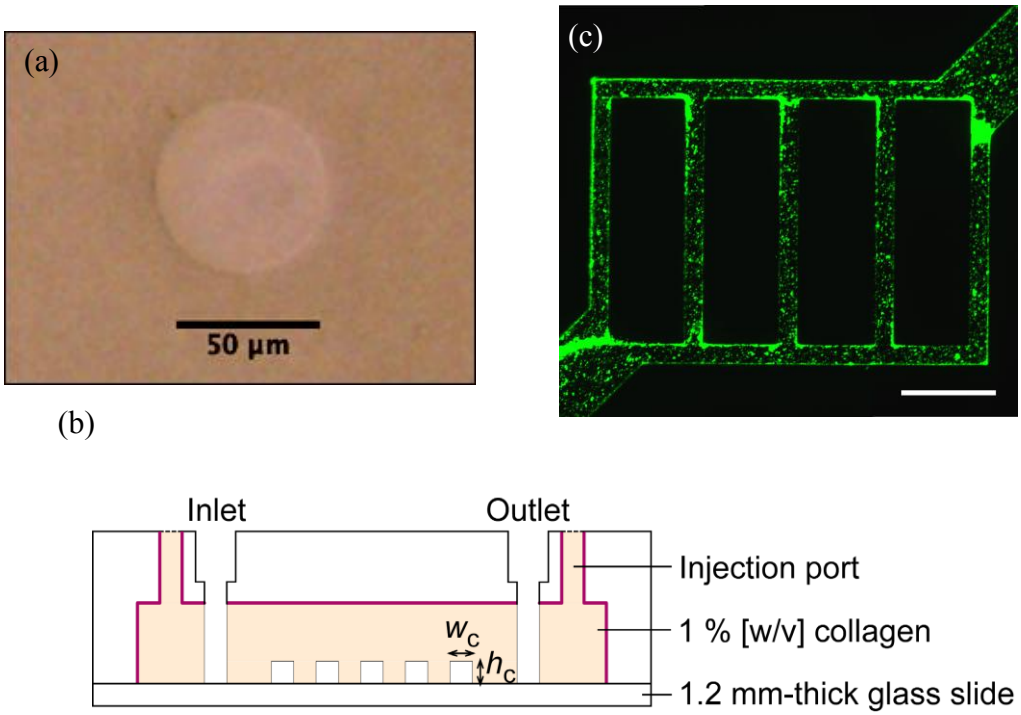

Figure 2-7. Microfabrication in dense collagen. (a) Replication of simple micro pores can be achieved at a low collagen concentration of 0.3% (b) Schematic illustration of fabricated and sealed microfluidic collagen. (c) Fluorescence micrograph of functional microfluidic 1 % [w/v] collagen during the delivery of green-fluorescent latex microbeads (~ 1 µm in diameter) via microchannels (scale bar = 500 µm; flow speed ~ 1 mm/s). Microchannel width, w_c = microchannel height, h_c = 100 µm.

After thorough washing of both the PDMS stamp and the PDMS overlayer, collagen of various concentrations (0.15%, 0.3%, 0.6%, 1%, and 2%) were prepared from the concentrated stock solutions as described above and gelled in the wells of the PDMS stamp by incubating at 37 °C with 5% CO_2 for 30 minutes. Because the collagen adhered to the PEI/GA coated overlayer, the molded collagen could be peeled

away from the PDMS stamp by handling only the PDMS overlayer and without direct handling the collagen gel. Gels were then imaged on a Nikon Eclipse TS100 microscope with an Olympus DP70 Camera using DP Controller software.

Circular pores with a diameter of 50 μm could be molded into 0.3% collagen matrices cleanly and reproducibly (Fig 2-7a); however, they could not be molded into 0.15% collagen matrices (data not shown).

2-10 Microfluidic device fabrication and operation

We are able to replicate microchannels using soft lithography and create a functional microfluidic device in a cellular remodelable material. The microfluidic device created from native type I collagen is a new generation *in vitro* tumor model and a platform for creating vascularized tissue engineered scaffolds.

Microfluidic collagen was fabricated similar to our previous approach presented in Choi, et al. [23]: 1) uncross-linked collagen was injected into a closed mold where a micropatterned PDMS (Sylgard® 184, Dow Corning, Midland, Michigan) stamp was inserted, and 2) cross-linked collagen with an imprinted microfluidic network was then pressure-sealed against a 1.2 mm-thick glass slide (Ted Pella, Inc., Redding, California) as illustrated in Figure 2-7b.

Functionality of microfluidic collagen was examined by delivering green-fluorescent latex microbeads (Fluoresbrite™ Carboxylate YG 1.0 micron Microspheres; Polyscience, Inc., Warrington, Pennsylvania) suspended in PBS via microchannels. To operate the microfluidic device, a gravity driven flow of the fluorescent microbeads was used. Flow rate was estimated by tracking beads over time as they flowed through the channels.

Note that the collagen was molded using custom jig, and the device was pressure sealed to glass leaving a 3-sided collagen channel (Figure 2-7b). A device using 0.6% collagen was attempted and failed. Specifically, only a portion of the microfluidic

network formed a seal with the bottom glass slide. Flow was introduced at 1 μL/min which resulted in a flow speed of ~ 1 mm/s. There was significant leakage at the inlet and outlet and after 15 minutes of flow, the initially sealed portion of the network began to leak. The modulus of the 0.6% collagen is low enough that the gel deforms and collapses easily during device assembly and even just by flow.

We determined that 1.0% is the lower limit to create a sealed microfluidic device (Figure 2-7c). The 1.0% collagen network formed a tight seal with the bottom glass boundary and functioned with flow in an incubator for more than three weeks. Successful microfluidic devices were fabricated in 1.5% and 2.0% collagen concentrations and maintained flow and sterility in a cell culture incubator without leaking for over three weeks.

2-11 Cell culture

Human umbilical vein endothelial cells (HUVECs) were purchased from Lonza (Walkersville, MD) and were used in passages 3-10. Cells were cultured in growth media as described in Appendix A-3. This growth media was changed every 2-3 days. Oral squamous cell carcinoma (OSCC-3) cells (a gift from Peter Polverini, University of Michigan) were cultured as described [74].

2-12 Remodelability of dense collagen by endothelial cells

We aim to determine the threshold collagen concentration that permits cellular invasion and endothelial network formation while still able to support microfabrication. We study *in vitro* vascular network formation within collagen matrices (Figs. 2-8, -2-9) and cellular invasion into collagen matrices (Figs. 2-12).

Vasculogenesis: To set up the vasculogenesis/network formation assays, cells at 75-95% confluency were washed with HEPES buffered saline solution, removed from culture flasks with trypsin-EDTA, neutralized with growth media, centrifuged, and resuspended at $6x10^6$ cells/ml. Cell-seeded collagen gels were prepared from a

concentrated, acidic stock collagen solution. The final volume of gels/cells was first determined by the recipe in Appendix A-5.

Briefly, a 0.1 volume fraction (with respect to total final volume) of 10x concentrated Medium 199, 1x M199, and 1N NaOH was mixed in an eppendorf tube on ice. The desired mass of collagen was placed in a separate eppendorf tube and kept on ice. The M199/NaOH solution was slowly mixed on ice into the acidic collagen solution using a small spatula. Once the collagen solution was a neutral pH (determined from phenol red dye in media), the appropriate volume of concentrated cell suspension (at $6x10^6$ cells/ml) was mixed into the neutralized collagen solution. Final collagen concentrations were made to 3, 8, 10, 15, or 20 mg/ml, and a final cell seeding density of $1x10^6$ cells/ml was used in all vasculogenesis assays.

Cell-seeded gels were either pipetted (for 3mg/ml and 8mg/ml concentrations) or injected with a 250 μl syringe into 4 mm diameter PDMS wells that were set, one per well, in 48-well plates and were allowed to gel at 37° C and 5% CO_2 for 30 minutes. The top surfaces were not flush with the top of the wells. 300 μl of vasculogenesis media (Appendix A-3) was added to each well in the 48-well plate. Vasculogenesis assays were kept at 37° C and 5% CO_2 for 3, 7, 14, or 21 days before fixing and staining. Cultures were re-fed with the above assay media every 48-72 hours.

Invasion: To set up the invasion assays, collagen gels were prepared from concentrated stock solutions as described above and either pipetted (for 3mg/ml and 8mg/ml collagen concentrations) or injected with a 250 μl syringe into 4 mm diameter PDMS wells that were set, one per well, in 48-well plates and were allowed to gel at 37° C and 5% CO_2 for 30 minutes. HUVECs ($200cells/mm^2$) were then seeded on top of the gel and allowed to attach for 30 minutes before placing 300 μl vasculogenesis media into the wells.

Staining and Microscopy: At the designated time points during the invasion and

vasculogenesis assays and co-culture experiment, gels and cells were fixed and stained (described in more detail in Appendix A-7) with a 1:100 dilution of Alexa Fluor 488 phalloidin or Alexa Fluor 568 phalloidin and 1:1000 dilution of 4',6-diamidino-2-phenylindole (DAPI) (368/461) or YOYO-1 iodide (491/509). For the co-culture experiment endothelial cells were also stained with CD-31 mouse anti-human/AlexaFluor 488 goat anti-mouse. With the exception of the permeabilization step, all incubations were conducted at room temperature with agitation.

Confocal images of the invasion and vasculogenesis assays and co-culture experiments were obtained using a Zeiss 510 Meta confocal microscope (Zeiss, Welwyn Garden City, United Kingdom) with a 63x, NA 1.4 oil immersion objective, a 40x, NA 1.3 oil immersion objective, or a 40x, NA 1.2 water immersion objective with a pinhole of one Airy Unit. Image stacks were accumulated with a z-step between each successive optical slice of 2 to 4 μm. Cross sections of the z-stack were rendered in the Zeiss Image Browser.

2-13 Collagen degradation

3-D vasculogenesis assays have been used to identify and characterize angiogenic promoters and inhibitors[75] and to study capillary tube formation[76]. For dense collagen matrices to be useful as a tumor model or a pre-vascularized scaffold for tissue engineering, endothelial cells must be able to remodel the material and undergo tube formation. Tube formation within dense collagen has not been demonstrated.

With confocal reflectance microscopy, we can see that cell have degraded circular voids into the collagen[10] at all concentrations by three days (Figure 2-8). The circular voids are lined by cells and are a cross-section of an open tube. By 21 days, significant degradation and cell lumens are seen at all concentrations; however, there are only differences in the collagen structure around the voids (lighter regions as compared to the bulk) at the low mass fractions (0.3, 0.6, and 1.0%).

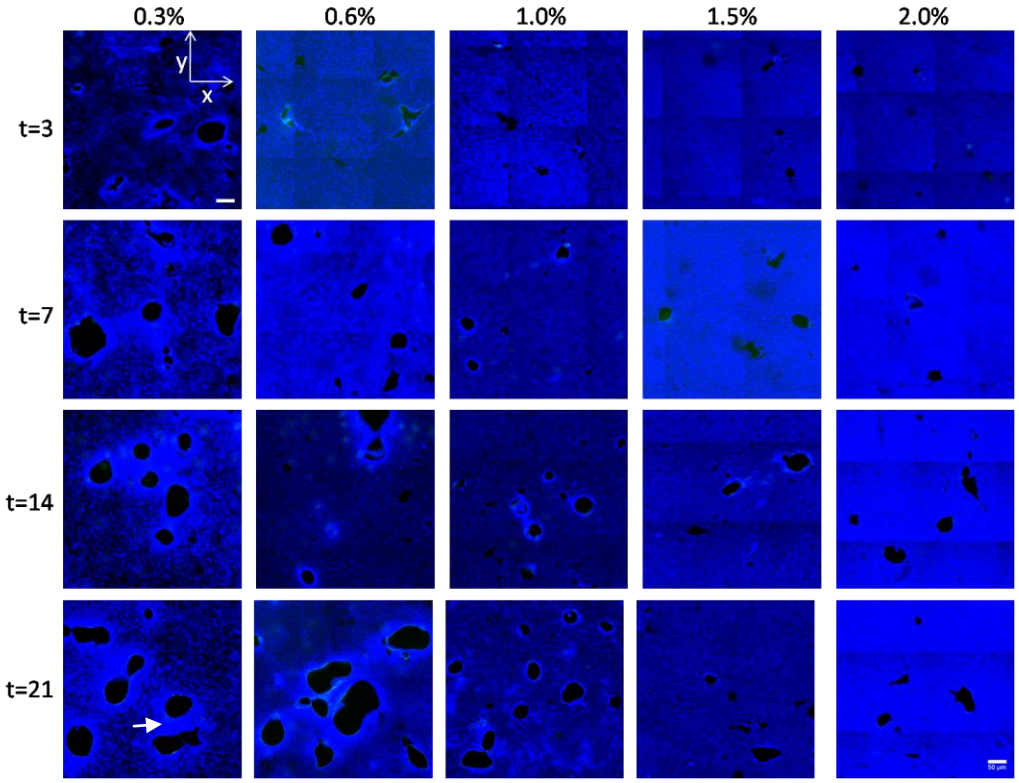

Figure 2-8. Confocal reflectance images showing matrix-free lumens at all collagen concentrations. Images show a single x-y plane ~ 20 μm above the adherent, bottom boundary at days 3, 7, 14, and 21. The arrow indicates collagen remodeling between void areas. Void areas are cell lumens and areas of matrix degradation. Using a 40x 1.3 NA oil immersion objective with a pinhole of 1 Airy Unit, a 3x3 array of images was taken using the automatic tile-scan function of the confocal microscope. Microscope software stitched the images together to form a single image. Scale bar = 50 μm.

The lighter areas in the collagen around the degraded voids are denser regions of collagen and could be either collagen deposition by the endothelial cells or collagen that has been pulled or gathered in towards the cells due to their traction forces. Because we can see this denser collagen between cell-created voids (arrow in Figure 2-8, 0.3%, 21 days) and cells gather fluorescent microspheres that are attached to the collagen into their structures (Figure 2-9), we believe the cells have used their traction forces to pull and align the collagen around the lumens.

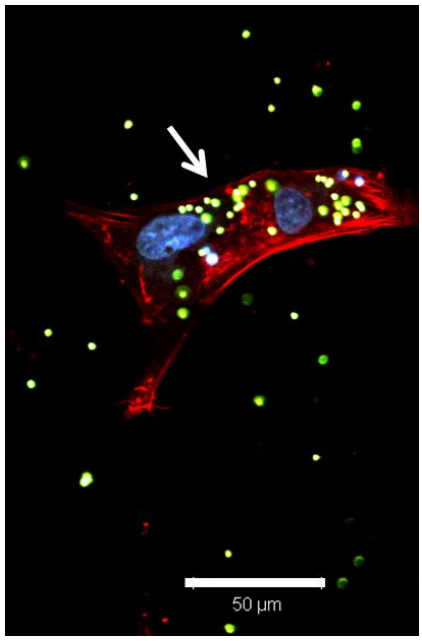

Figure 2-9. Microspheres near cellular structures. Embedded microspheres (Fluoresbrite™ Carboxylate YG 1.0 micron Microspheres; Polyscience, Inc., Warrington, Pennsylvania) were physisorbed to the collagen matrix by mixing with the collagen-cell solution before collagen gelation at t=0. After 72 hours, a fixed and stained 3-D sample is imaged using confocal fluorescent microscopy and microspheres can be seen pulled in towards cells. (Red=actin, blue=nuclei, green/yellow = microspheres) Scale bar = 50 µm.

2-14 Cellular networks in dense collagen

After staining the f-actin network and the nuclei of the endothelial cells, we used confocal fluorescence microscopy to visualize the cellular structures. Visible lumen formation in the *xy* plane can be seen at all collagen concentrations by day 3. (Figure 2-10). We captured a *z*-stack of images at each concentration and time point and were able to generate *xz* planes to visualize the extent of network formation from the boundary into the bulk (Figure 2-11) and see the differences in morphology at the different mass fractions. A 3-D connected network (an open, continuous tube that is supported in the *z*-direction) with many connections can be seen in the 0.3% collagen

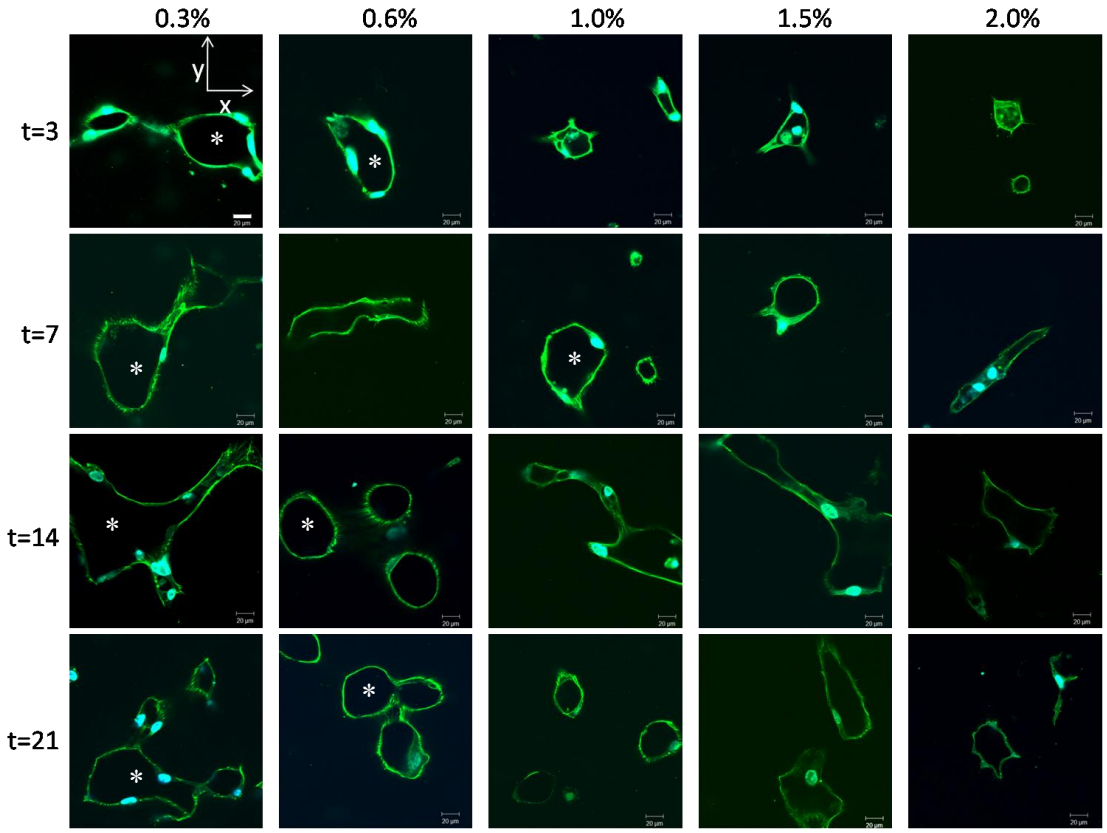

Figure 2-10. Endothelial cell lumen size and frequency versus collagen concentration and time for 3D vasculogenesis assays Confocal fluorescent images of a single *xy* plane ~ 20 microns above the bottom boundary at days 3,7,14, and 21. Cells were stained with Alexa Fluor-488 phalloidin and DAPI nuclear stain. All circular structures are open lumens. Asterisks indicate a few examples of these open lumens free of collagen. Scale bar = 20 μm

at 3 days, in the 0.8 % at 7 days, and in the 1.0% collagen at 21 days (Fig 2-11). We can see that networks emerge from the bottom boundary substrate suggesting that a multicellular network may need a stiff surface to extend into the collagen. Another reason for the emergence of structure at the boundary may be due to an increase of cell density at the boundary due to the cells' preference to adhere and spread on a stiff

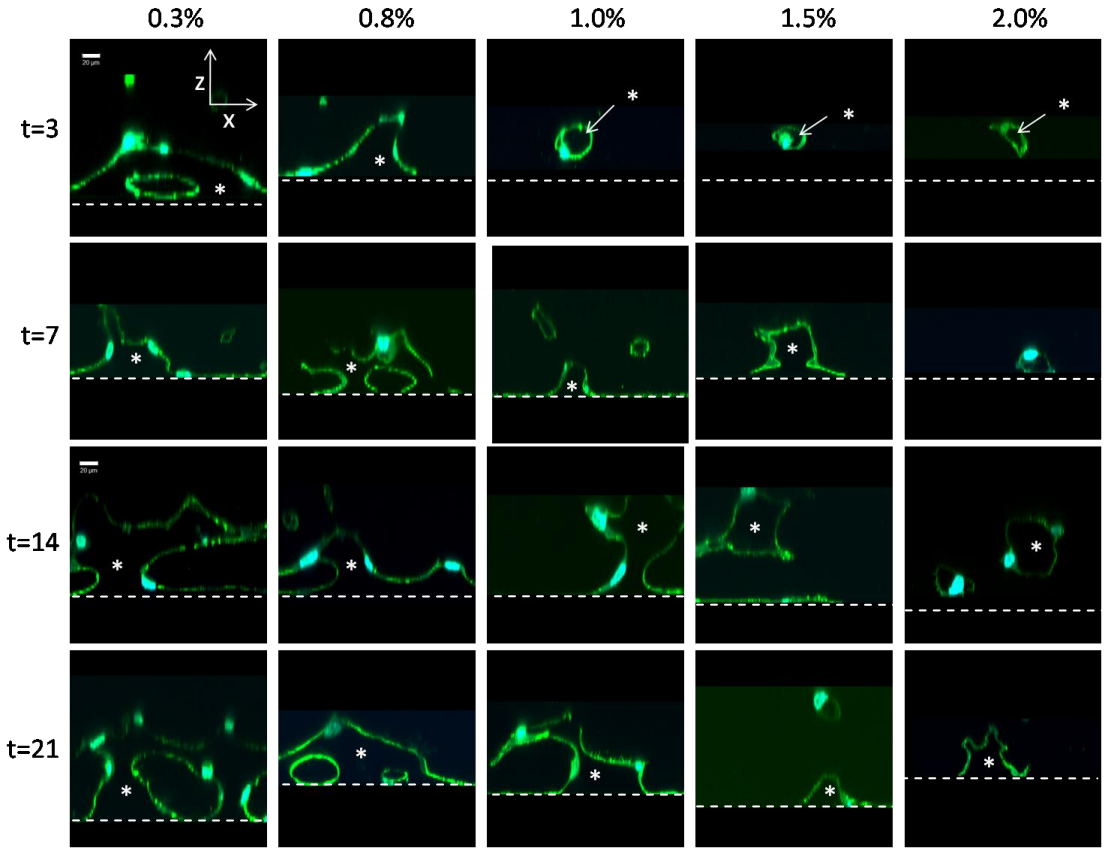

Figure 2-11. Endothelial cell lumen size and frequency in the xz plane versus collagen concentration and time for 3D vasculogenesis assays Confocal *xz* cross-sections rendered from *z*-stacks through the collagen matrices at days 3, 7, 14, and 21 for each collagen concentration. Cells were stained with Alexa Fluor-488 phalloidin and DAPI nuclear stain. Dashed horizontal lines represent the location of the bottom boundary. Asterisks (*) indicate matrix-free lumens. Scale bar = 20 μm.

substrate. Additional studies need to be performed to understand this behavior.

We quantify lumen area and frequency for the different collagen concentrations (Figure 2-12). In general, lumen density and area increase with time and decrease with an increase in collagen concentration. At the low mass fractions, lumen frequency decreases slightly from day 3 to day 7 (Figure 2-12b) indicating possible tube regression; however, this decrease is not statistically significant.

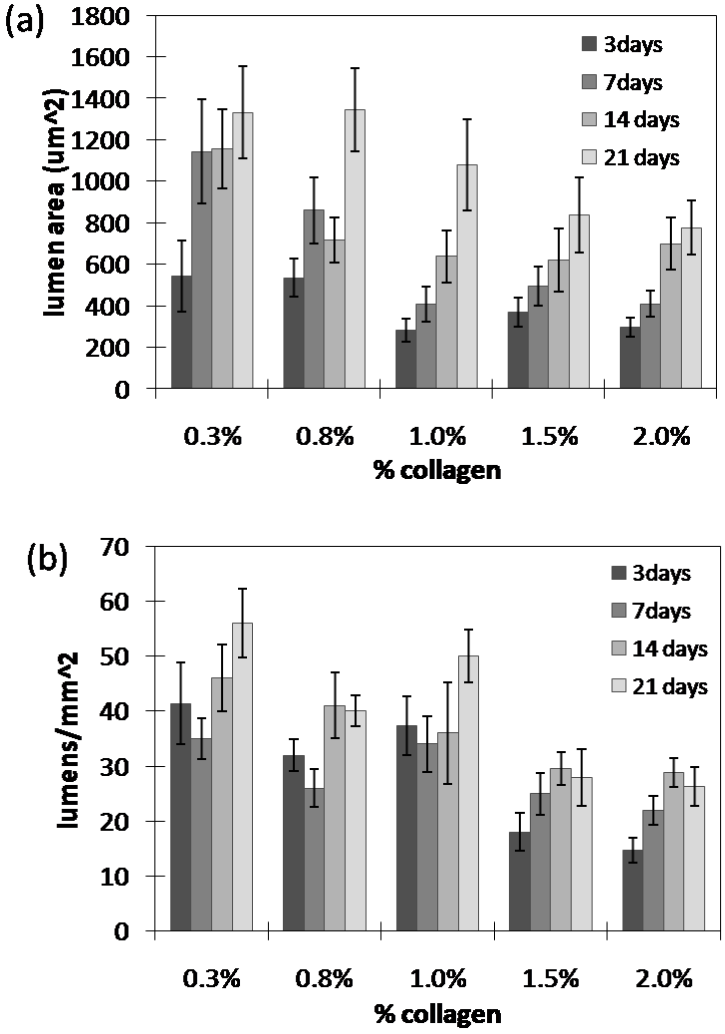

Figure 2-12. Quantification of lumen area and frequency. Average lumen area (a) and lumen frequency (b) in the bulk ~20 microns from bottom boundary vary over time and with collagen concentration. Collagen free lumens were quantified using confocal reflectance images with a total area of 0.25 mm^2. Images were made binary and lumen number and area were calculated using Image J. Error bars represent the standard deviation. n= 3-5 gels for each time point and condition.

2-15 Cellular invasion in dense collagen

HUVEC invasion experiments are commonly used to study the development of capillary sprouts and tubes[53]. These experiments monitor endothelial cell invasion into low weight percent collagen gels (usually ~0.25%) over the course of usually about 2-3 days. We perform similar invasion experiments only we use collagen

concentrations up to 20 mg/ml. Based on the collagen structure and pore size at higher concentrations (Figure 2-2), the dense collagen presumably provides significantly more steric hindrance for cells, so we allow the invasion assays to culture for up to three weeks.

HUVECs form a monolayer on top of collagen (blue nuclei stain in Figure 2-13a), and cells invade over time. As expected, invasion distance and frequency decrease with increasing collagen concentration (Figure 2-12b,c) at early times. Very little invasion can be seen in 2% collagen even after 21 days of culture (arrow in Figure 2-12(a) points to a cell structure that has invaded ~ 20 μm). Invasion distance steadily increases during the first 14 days of culture for 0.3, 0.6 and 1% collagen gels. At these early times, the length of the invasions scales like 1/[Collagen] (invasions in 0.6% are half as long as in 0.3% and so on). This observation is compatible with the hypothesis that degradation is the rate limiting step during the invasion process [10]. Invasion distance continues to increase for the 0.6% and 1% collagen gels until day 21; however, does not continue to increase in the 0.3% gels. Significant tube regression in 0.25% collagen gels has been reported[77] which may explain the absence of further invasion in the 0.3% gels. Invasion frequency peaks at ~ 7 days in the 0.3% collagen and at day 21 for the higher concentration collagen matrices. Again, MMP-regulated tube regression may explain the earlier peak for the lower concentration gels. Note that the vasculogenic activity (Figure 2-12) is much less heavily suppressed by increasing mass fraction than invasion (Figure 2-13).

The results pertaining to concentration- and time-dependent vasculogenesis and invasion of endothelial cells is important information consider for applications using this dense collagen as a host for invasion *in vivo* and *in vitro*.

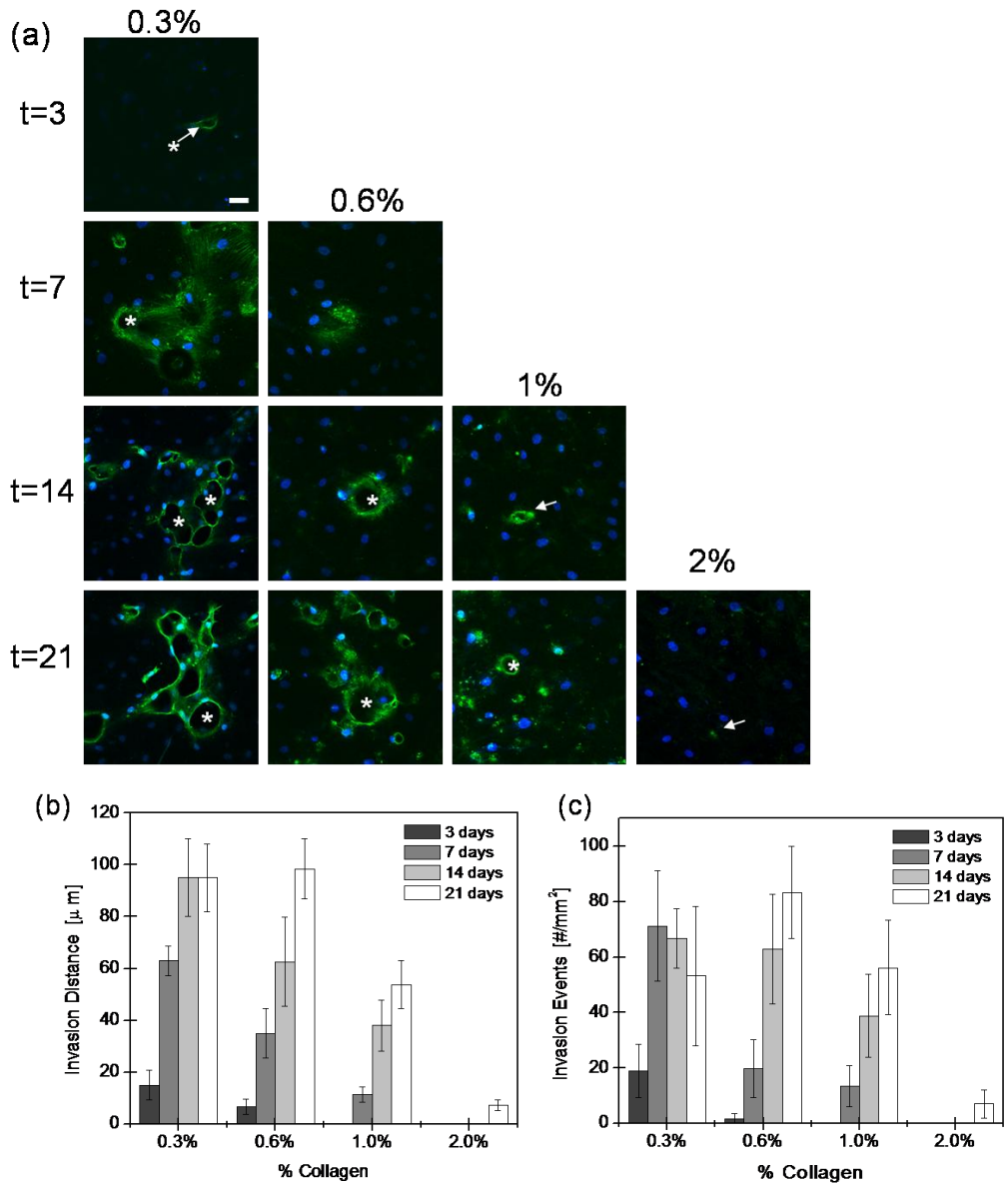

Figure 2-13. Endothelial cell invasion distance and frequency versus collagen concentration and time. **(**a) Confocal fluorescent images of single *xy* planes at z = -10 μm below the HUVEC monolayer at various time points for 0.3, 0.6, 1.0, and 2.0% collagen. Cells were stained with AlexaFluor 568 Phalloidin and YOYO-1 Iodide nuclear stain. Asterisks indicate open lumens. Arrows point to cellular structures. No images are included for the early time points for 0.6, 1.0%, and 2.0% collagen because no significant invasion had occurred. Invasion depth (b) and frequency (c) into the collagen bulk at 3, 7, 14, and 21 days as a function of collagen concentration. All images in this figure were taken using 20x objective with a pinhole of 1 Airy Unit. Scale bar = 50 μm. Error bars represent the standard deviation n=3-5 gels for each time point and condition. These experiments performed by Ying Zheng, a post doc in our lab who is continuing aspects of my research.

2-16Tumor angiogenesis model

Here we describe our preliminary work in creating an *in vitro* tumor angiogenesis model by co-culturing oral squamous cell carcinoma (OSCC-3) cells into the bulk of a high mass fraction collagen gel and seeding HUVECs on the matrix surface permitting invasion towards the cancer cells. Similar to the vasculogenesis assays described above, oral squamous cell carcinoma (OSCC-3) cells were seeded in 6.75 mg/ml collagen gels at a concentration of $2x10^7$ cells/ml into molded into PDMS wells and allowed to gel at 37° C and 5% CO_2 for 30 minutes. OSCC-3-containing gels were then top-seeded with HUVECs at a density of 300 cells/mm^2. Co-cultures were maintained for 3 days the HUVEC growth media (Appendix A-3), supplemented with 50ug/ml L-ascorbic acid and 50 ng/ml TPA.

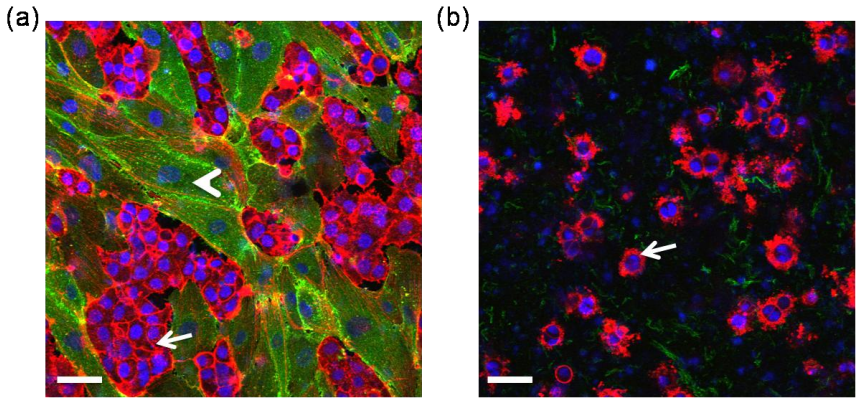

Figure 2-14. HUVEC and OSCC-3 co-culture at t= 3 days. (a) Confocal fluorescence image at the surface of an OSCC-3 cell-seeded collagen gel. Collagen was top-seeded with HUVECs at a density of 300 cells/mm^2. Arrows indicate OSCCs and arrow head indicates the HUVEC monolayer. (b) Confocal image ~ 20 μm below the HUVEC monolayer in the bulk of the 0.625% collagen gel. Samples are fixed and stained with DAPI, AlexaFluor 568 phalloidin, and CD-31 mouse anti-human/AlexaFluor 488 goat anti-mouse. Scale bars = 20 μm. Image taken by Scott Verbridge in Dr. Claudia Fischbach's lab at Cornell University.

HUVECs form a confluent monolayer (arrow head in Figure 2-14a) and tumor cells begin to proliferate towards the top of the gel. (arrow in Figure 2-14a). Tumor cells survive and proliferate (measured by DNA assay- data not shown) while embedded within the dense collagen matrix (Fig 2-12b).

2-17 Conclusions and future applications

We have demonstrated that dense collagen matrices are mechanically robust while maintaining the ability to be remodeled by cells. The modulus and permeability values measured for our dense collagen matrix are physiological relevant (Figure 2-6). For example, tumor and stromal cells have been shown to produce and assemble a dense matrix of collagens and other molecules that hinder the transport of macromolecules within tumors with collagen content between 1 and 4%[78]. The elastic modulus of four types of tumor ranges from 5-300 mm Hg which converts to ~ 700 Pa – 40 kPa[79]. Our 1.0%, 1.5%, and 2.0% collagen matrices fall within this range.

We have shown that simple microstructure can be replicated in 0.3% collagen, which is the standard concentration of angiogenesis and invasion assays. We determined that the threshold collagen concentration that permits cellular invasion and endothelial network formation while still able to support microfabrication is 1%. Most cell-remodelable materials are not mechanically robust enough to be microfabricated. Because the dense collagen can be both microfabricated and remodeled by cells, there is potential to control the spatial and temporal chemistry and fluid mechanics seen by endothelial cells and cells in the bulk within these scaffolds.

Currently, our lab is endothelializing the channels within the collagen microfluidic network and is using it as a platform to study tumor angiogenesis. Because the microfluidic device fabrication is cell friendly, we plan to seed other types of cell, like pericytes, into the bulk collagen material that makes up the channels

in order to study pericyte stabilization of vessels.

The endothelialized microfluidic collagen scaffold is an advanced *in vitro* tumor model that nicely mimics *in vivo* conditions including: ECM density, a vascular network with flow, and tumor cell signaling from the bulk. It has the potential to be used as an *in vitro* platform for tumor metastasis or leukocyte extravasation and intravasation[80]. Finally, these dense collagen scaffolds are currently being implanted into mice to study *in vivo* cellular invasion and biocompatibility.

REFERENCES

1. Quinn, T.M. and A.J. Grodzinsky, *Longitudinal Modulus and Hydraulic Permeability of Poly(Methacrylic Acid) Gels - Effects of Charge-Density and Solvent Content.* Macromolecules, 1993. **26**(16): p. 4332-4338.

2. Yannas, I.V., *Tissue regeneration by use of collagen-glycosaminoglycan copolymers.* Clin Mater, 1992. **9**(3-4): p. 179-87.

3. Seal, B.L., T.C. Otero, and A. Panitch, *Polymeric biomaterials for tissue and organ regeneration.* Materials Science & Engineering R-Reports, 2001. **34**(4-5): p. 147-230.

4. Griffith, L.G., *Emerging design principles in Biomaterials and scaffolds for tissue engineering.* Reparative Medicine: Growing Tissues and Organs, 2002. **961**: p. 83-95.

5. Nelson, C.M. and M.J. Bissell, *Modeling dynamic reciprocity: engineering three-dimensional culture models of breast architecture, function, and neoplastic transformation.* Semin Cancer Biol, 2005. **15**(5): p. 342-52.

6. Smalley, K.S.M., M. Lioni, and M. Herlyn, *Life isn't flat: Taking cancer biology to the next dimension.* In Vitro Cellular & Developmental Biology-Animal, 2006. **42**(8-9): p. 242-247.

7. Schindler, M., et al., *Living in three dimensions - 3D nanostructured environments for cell culture and regenerative medicine.* Cell Biochemistry and Biophysics, 2006. **45**(2): p. 215-227.

8. Pedersen, J.A. and M.A. Swartz, *Mechanobiology in the third dimension.* Annals of Biomedical Engineering, 2005. **33**(11): p. 1469-1490.

9. Nelson, C.M., et al., *Tissue geometry determines sites of mammary branching morphogenesis in organotypic cultures.* Science, 2006. **314**(5797): p. 298-300.

10. Davis, G.E. and D.R. Senger, *Endothelial extracellular matrix - Biosynthesis, remodeling, and functions during vascular morphogenesis and neovessel stabilization.* Circulation Research, 2005. **97**(11): p. 1093-1107.

11. Fischbach, C., et al., *Engineering tumors with 3D scaffolds.* Nat Methods, 2007. **4**(10): p. 855-60.

12. Fidler, I.J., *Critical factors in the biology of human cancer metastasis: twenty-eighth G.H.A. Clowes memorial award lecture.* Cancer Res, 1990. **50**(19): p. 6130-8.

13. Ferrara, N., *VEGF and the quest for tumour angiogenesis factors.* Nat Rev Cancer, 2002. **2**(10): p. 795-803.

14. LeCouter, J., et al., *Identification of an angiogenic mitogen selective for endocrine gland endothelium.* Nature, 2001. **412**(6850): p. 877-84.

15. Levenberg, S., et al., *Engineering vascularized skeletal muscle tissue.* Nat Biotechnol, 2005. **23**(7): p. 879-84.

16. Griffith, C.K., et al., *Diffusion limits of an in vitro thick prevascularized tissue.* Tissue Eng, 2005. **11**(1-2): p. 257-66.

17. Discher, D.E., P. Janmey, and Y.L. Wang, *Tissue cells feel and respond to the stiffness of their substrate.* Science, 2005. **310**(5751): p. 1139-43.

18. Sieminski, A.L., R.P. Hebbel, and K.J. Gooch, *The relative magnitudes of endothelial force generation and matrix stiffness modulate capillary morphogenesis in vitro.* Exp Cell Res, 2004. **297**(2): p. 574-84.

19. Reinhart-King, C.A., M. Dembo, and D.A. Hammer, *Cell-cell mechanical communication through compliant substrates.* Biophys J, 2008. **95**(12): p. 6044-51.

20. Lo, C.M., et al., *Cell movement is guided by the rigidity of the substrate.* Biophys J, 2000. **79**(1): p. 144-52.

21. Nakagawa, S., P. Pawelek, and F. Grinnell, *Long-term culture of fibroblasts in contracted collagen gels: effects on cell growth and biosynthetic activity.* J Invest Dermatol, 1989. **93**(6): p. 792-8.

22. Fischbach, C., et al., *Cancer cell angiogenic capability is regulated by 3D culture and integrin engagement.* Proc Natl Acad Sci U S A, 2009. **106**(2): p. 399-404.

23. Choi, N.W., et al., *Microfluidic scaffolds for tissue engineering.* Nat Mater, 2007. **6**(11): p. 908-15.

24. Lee, C.S., et al., *Integration of layered chondrocyte-seeded alginate hydrogel scaffolds.* Biomaterials, 2007. **28**(19): p. 2987-93.

25. Novikova, L.N., et al., *Alginate hydrogel and matrigel as potential cell carriers for neurotransplantation.* J Biomed Mater Res A, 2006. **77**(2): p. 242-52.

26. Ambrosi, D., Bussolino, F., Preziosi, L., *A Review of Vasculogenesis Models.* 2004.

27. Deroanne, C.F., C.M. Lapiere, and B.V. Nusgens, *In vitro tubulogenesis of endothelial cells by relaxation of the coupling extracellular matrix-cytoskeleton.* Cardiovasc Res, 2001. **49**(3): p. 647-58.

28. Ingber, D.E. and J. Folkman, *Mechanochemical Switching between Growth and Differentiation During Fibroblast Growth Factor-Stimulated Angiogenesis Invitro - Role of Extracellular-Matrix.* Journal of Cell Biology, 1989. **109**(1): p. 317-330.

29. Balgude, A.P., et al., *Agarose gel stiffness determines rate of DRG neurite extension in 3D cultures.* Biomaterials, 2001. **22**(10): p. 1077-84.

30. Sakai, S., I. Hashimoto, and K. Kawakami, *Synthesis of an agarose-gelatin conjugate for use as a tissue engineering scaffold.* J Biosci Bioeng, 2007. **103**(1): p. 22-6.

31. Helm, C.L.E., et al., *Synergy between interstitial flow and VEGF directs capillary morphogenesis in vitro through a gradient amplification mechanism.* Proceedings of the National Academy of Sciences of the United States of America, 2005. **102**(44): p. 15779-15784.

32. Vailhe, B., et al., *The formation of tubular structures by endothelial cells is under the control of fibrinolysis and mechanical factors.* Angiogenesis, 1998. **2**(4): p. 331-44.

33. Ito, S., S. Ishimaru, and S.E. Wilson, *Inhibitory effect of type 1 collagen gel containing alpha-elastin on proliferation and migration of vascular smooth muscle and endothelial cells.* Cardiovasc Surg, 1997. **5**(2): p. 176-83.

34. Suh, J.K. and H.W. Matthew, *Application of chitosan-based polysaccharide biomaterials in cartilage tissue engineering: a review.* Biomaterials, 2000. **21**(24): p. 2589-98.

35. Gamini, A., et al., *Structural investigations of cross-linked hyaluronan.* Biomaterials, 2002. **23**(4): p. 1161-7.

36. Williams, B.R., et al., *Collagen fibril formation. Optimal in vitro conditions and preliminary kinetic results.* J Biol Chem, 1978. **253**(18): p. 6578-85.

37. Elsdale, T. and J. Bard, *Collagen substrata for studies on cell behavior.* J Cell Biol, 1972. **54**(3): p. 626-37.

38. Piez, K.A., *The structure of the collagen fibril.* Suppl Thromb Haemost, 1978. **63**: p. 111-22.

39. Piez, K.A. and A. Miller, *The structure of collagen fibrils.* J Supramol Struct, 1974. **2**(2-4): p. 121-37.

40. Haudenschild, F.a., *Angiogenesis in vitro.* Nature, 1980. **288**: p. 551-556.

41. Gelman, R.A. and K.A. Piez, *Collagen fibril formation in vitro. A quasielastic light-scattering study of early stages.* J Biol Chem, 1980. **255**(17): p. 8098-102.

42. Lee, C.R., A.J. Grodzinsky, and M. Spector, *The effects of cross-linking of collagen-glycosaminoglycan scaffolds on compressive stiffness, chondrocyte-mediated contraction, proliferation and biosynthesis.* Biomaterials, 2001. **22**(23): p. 3145-54.

43. Chandran, P.L. and V.H. Barocas, *Microstructural mechanics of collagen gels in confined compression: poroelasticity, viscoelasticity, and collapse.* J Biomech Eng, 2004. **126**(2): p. 152-66.

44. Mickel, W., et al., *Robust pore size analysis of filamentous networks from three-dimensional confocal microscopy.* Biophys J, 2008. **95**(12): p. 6072-80.

45. Yannas, I.V. and J.F. Burke, *Design of an artificial skin. I. Basic design principles.* J Biomed Mater Res, 1980. **14**(1): p. 65-81.

46. Brinkman, W.T., et al., *Photo-cross-linking of type I collagen gels in the presence of smooth muscle cells: mechanical properties, cell viability, and function.* Biomacromolecules, 2003. **4**(4): p. 890-5.

47. Helm, C.L., A. Zisch, and M.A. Swartz, *Engineered blood and lymphatic capillaries in 3-D VEGF-fibrin-collagen matrices with interstitial flow.* Biotechnol Bioeng, 2007. **96**(1): p. 167-76.

48. Vernon, R.B., et al., *Native fibrillar collagen membranes of micron-scale and submicron thicknesses for cell support and perfusion.* Biomaterials, 2005. **26**(10): p. 1109-17.

49. Wang, M.C., G.D. Pins, and F.H. Silver, *Collagen fibres with improved strength for the repair of soft tissue injuries.* Biomaterials, 1994. **15**(7): p. 507-12.

50. Nehrer, S., et al., *Chondrocyte-seeded collagen matrices implanted in a chondral defect in a canine model.* Biomaterials, 1998. **19**(24): p. 2313-28.

51. Ceballos, D., et al., *Magnetically aligned collagen gel filling a collagen nerve guide improves peripheral nerve regeneration.* Exp Neurol, 1999. **158**(2): p. 290-300.

52. Eschenhagen, T., et al., *Three-dimensional reconstitution of embryonic cardiomyocytes in a collagen matrix: a new heart muscle model system.* FASEB J, 1997. **11**(8): p. 683-94.

53. Davis, G.E., S.M. Black, and K.J. Bayless, *Capillary morphogenesis during*

human endothelial cell invasion of three-dimensional collagen matrices. In Vitro Cell Dev Biol Anim, 2000. **36**(8): p. 513-9.

54. Bayless, K.J. and G.E. Davis, *Sphingosine-1-phosphate markedly induces matrix metalloproteinase and integrin-dependent human endothelial cell invasion and lumen formation in three-dimensional collagen and fibrin matrices.* Biochem Biophys Res Commun, 2003. **312**(4): p. 903-13.

55. Ng, C.P., C.L. Helm, and M.A. Swartz, *Interstitial flow differentially stimulates blood and lymphatic endothelial cell morphogenesis in vitro.* Microvasc Res, 2004. **68**(3): p. 258-64.

56. Bell, E., B. Ivarsson, and C. Merrill, *Production of a tissue-like structure by contraction of collagen lattices by human fibroblasts of different proliferative potential in vitro.* Proc Natl Acad Sci U S A, 1979. **76**(3): p. 1274-8.

57. Mueller-Klieser, W., *Tumor biology and experimental therapeutics.* Crit Rev Oncol Hematol, 2000. **36**(2-3): p. 123-39.

58. Ramanujan, S., et al., *Diffusion and convection in collagen gels: implications for transport in the tumor interstitium.* Biophys J, 2002. **83**(3): p. 1650-60.

59. Helary, C., et al., *Dense fibrillar collagen matrices: a model to study myofibroblast behaviour during wound healing.* Biomaterials, 2006. **27**(25)

60. Golden, A.P. and J. Tien, *Fabrication of microfluidic hydrogels using molded gelatin as a sacrificial element.* Lab Chip, 2007. **7**(6): p. 720-5.

61. Chrobak, K.M., D.R. Potter, and J. Tien, *Formation of perfused, functional microvascular tubes in vitro.* Microvasc Res, 2006. **71**(3): p. 185-96.

62. Tien, J., C.M. Nelson, and C.S. Chen, *Fabrication of aligned microstructures with a single elastomeric stamp.* Proc Natl Acad Sci U S A, 2002. **99**(4): p. 1758-62.

63. Bornstein, M.B., *Reconstituted rattail collagen used as substrate for tissue cultures on coverslips in Maximow slides and roller tubes.* Lab Invest, 1958. **7**(2): p. 134-7.

64. Davis, G.E. and C.W. Camarillo, *An alpha 2 beta 1 integrin-dependent pinocytic mechanism involving intracellular vacuole formation and coalescence regulates capillary lumen and tube formation in three-dimensional collagen matrix.* Exp Cell Res, 1996. **224**(1): p. 39-51.

65. Hermanson, G., *Bioconjugate techniques*, ed. A. Press. Vol. 1. 1996, San Diego, CA: Elsevier Science.

66. Brightman, A.O., et al., *Time-lapse confocal reflection microscopy of collagen fibrillogenesis and extracellular matrix assembly in vitro.* Biopolymers, 2000. **54**(3): p. 222-34.

67. Mickel, W., et al., *Robust pore size analysis of filamentous networks from three-dimensional confocal microscopy.* Biophysical Journal, 2008. **95**(12): p. 6072-80.

68. Roy, R., A. Boskey, and L.J. Bonassar, *Processing of type I collagen gels using nonenzymatic glycation.* J Biomed Mater Res A, 2009.

69. Sokolnikoff, I., *Mathematical theory of elasticity* 2nd ed, ed. Krieger. 1983, Malabar FL.

70. Pluen, A., et al., *Diffusion of macromolecules in agarose gels: comparison of linear and globular configurations.* Biophys J, 1999. **77**(1): p. 542-52.

71. Levick, J.R., *Flow through Interstitium and Other Fibrous Matrices.* Quarterly Journal of Experimental Physiology and Cognate Medical Sciences, 1987. **72**(4): p. 409-438.

72. Levick, J.R., *Flow through interstitium and other fibrous matrices.* Q J Exp Physiol, 1987. **72**(4): p. 409-37.

73. Whitesides, G.M., et al., *Soft lithography in biology and biochemistry.* Annu Rev Biomed Eng, 2001. **3**: p. 335-73.

74. Kumar, P., et al., *Combination treatment significantly enhances the efficacy of antitumor therapy by preferentially targeting angiogenesis.* Lab Invest, 2005. **85**(6): p. 756-67.

75. Jain, R.K., et al., *Quantitative angiogenesis assays: progress and problems.* Nature Medicine, 1997. **3**(11): p. 1203-8.

76. Kamei, M., et al., *Endothelial tubes assemble from intracellular vacuoles in vivo.* Nature, 2006. **442**(7101): p. 453-6.

77. Davis, G.E., et al., *Matrix metalloproteinase-1 and -9 activation by plasmin regulates a novel endothelial cell-mediated mechanism of collagen gel contraction and capillary tube regression in three-dimensional collagen matrices.* Journal of Cell Science, 2001. **114**(5): p. 917-930.

78. Ramanujan, S., et al., *Diffusion and convection in collagen gels: Implications for transport in the tumor interstitium.* Biophysical Journal, 2002. **83**(3): p. 1650-1660.

79. Netti, P.A., et al., *Role of extracellular matrix assembly in interstitial transport in solid tumors.* Cancer Res, 2000. **60**(9): p. 2497-503.

80. Huttenlocher, A. and M.C. Poznansky, *Reverse leukocyte migration can be attractive or repulsive.* Trends Cell Biol, 2008. **18**(6): p. 298-306.

CHAPTER 3

COLLECTIVE CELL BEHAVIOR DURING 3-D VASCULOGENESIS *IN VITRO*

3-1 Introduction

Vasculogenesis is a dynamic process whereby large populations of individual endothelial precursor cells interact locally to build a globally connected network of functional vascular tubes [4, 5]. Motility-related cellular behaviors including migration[6], (chemotaxis, durotaxis, and haptotaxis), cellular convection by global tissue deformations [8], and extensive protrusion activity [8-10] have been observed to be critical during vasculogenesis both *in vivo* and *in vitro*. Other cell and tissue behaviors that are seen both *in vivo* and *in vitro* during vasculogenesis include cell-specific contact interactions[11-13], vacuole and tube formation [14], and local matrix degradation [15].

There are a variety of mechanical, chemical, and topographical cues that can direct the cell behaviors mentioned above. For example, VEGF signaling [10, 16-19] has been shown to be critical for *in vivo* vasculogenesis as well as ECM chemistry and mechanics [20] and integrin signaling [8]. Similarly, mechanisms guiding *in vitro* cellular dynamics and behaivors during vascular network formation include VEGF signaling [10, 21], cell density[21], ECM chemistry and mechanics [9, 22, 23], integrin signaling [24], and MMP activity [15, 25, 26]. The multitude of both chemical and mechanical mechanisms implicated in global cell organization during vasculogenesis make it a challenging puzzle, and the general principles guiding the morphogenesis of the primitive vascular system are still poorly understood. In this chapter, I describe our work towards understanding the physical mechanisms behind global, collective cellular self-organization during *in vitro* vasculogenesis.

3-2 Vasculogenesis in 3-D, type I collagen

We approach the study of global cellular organization with the following hypotheses: 1) the self-organization of endothelial cells into a plexus follows simple percolation theory, 2) the critical percolation density is defined by the length scale of cell-cell interactions, and 3) the extent of cell-cell interactions is based on long range interactions between cells. To test these hypotheses, we embed human umbilical vein endothelial cells (HUVECs) in three dimensional (3-D) type I collagen matrices (Figure 3-1). We vary cell seeding density to change initial cell-cell spacing in an attempt to define the length-scale over which interactions occur between cells.

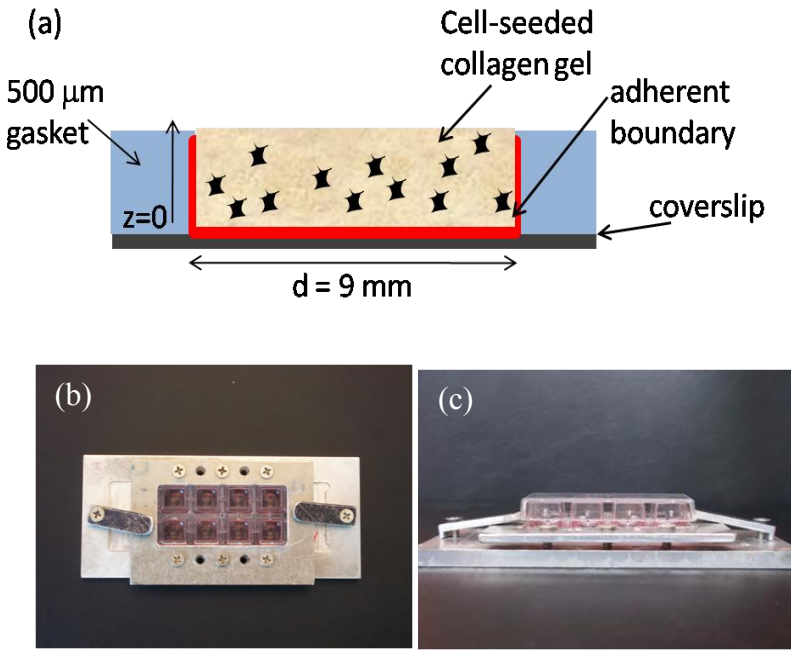

Figure 3-1. 3-D vasculogenesis assay experimental setup. (a) Human umbilical vein endothelial cells (HUVECs) are seeded into 0.3% type I collagen gels molded into disks of defined diameter and thickness. The cell-seeded matrix was covalently crosslinked to the bottom and side boundaries (Appendix A-6) and vasculogenesis media (Appendix A-3) was added above each culture. (b) Top view of clamping system used in experiments. (c) Side view of clamping system used in experiments.

To prepare the collagen matrix, collagen was extracted from rat tails [27, 28]. Our detailed protocol can be found in Appendix A-4. Cells at 75-95% confluency were washed with HEPES buffered saline solution, removed from culture flasks with trypsin-EDTA, neutralized with growth media, centrifuged, and resuspended at $6x10^6$ cells/ml. Cell-seeded collagen gels were prepared from a concentrated stock collagen solution by adding 1N sodium hydroxide (NaOH), 10x concentrated M199, 1x M199 to a final concentration of 3 mg/ml with various initial cell seeding densities (See Appendix A-5 for gelation protocol).

Figure 3-1 is a schematic of the experimental setup used for the vasculogenesis assays. A 500 μm thick Press-to-Seal® silicone gasket with eight, 9-mm diameter holes was placed on a 60x24 mm cover glass. The formed wells were then cleaned and treated chemically to covalently bind the collagen to the well boundaries (Figure 3-2). Adhering the collagen to the boundaries prevented cell-mediated gel contraction

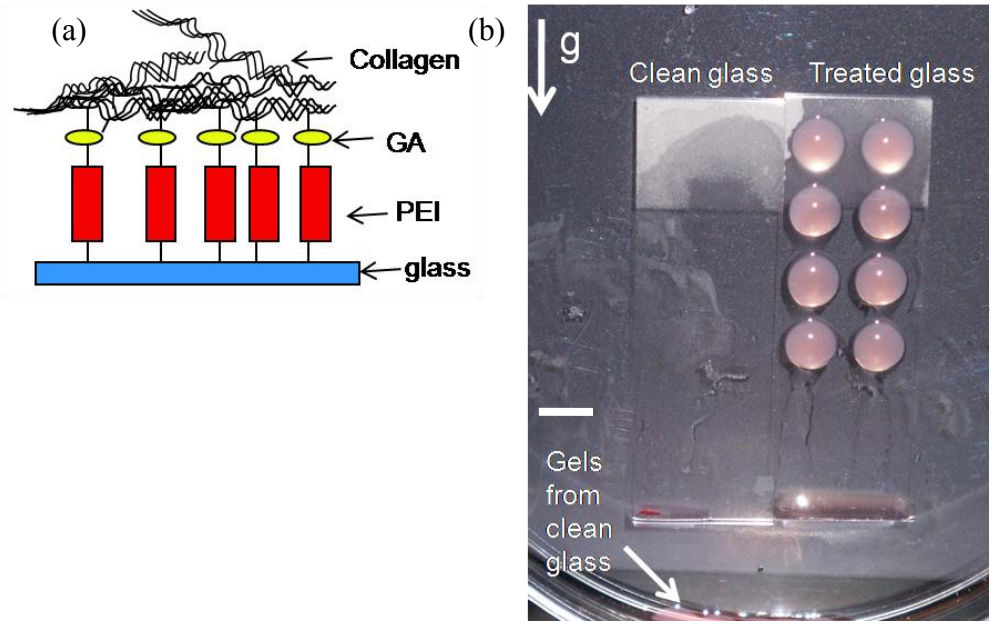

Figure 3-2. (a) Schematic of chemical treatment to make collagen adhere to a substrate. (b) Image showing collagen gels adhered to a treated (as in (a)) glass slide. "g" is the direction of gravity. Scale bar = 1 cm.

and allowed for open network formation at very high cell densities ($3x10^6$ cells/ml). The surface treatment method was adapted from [29] and details can be found in Appendix A-6. Cell-seeded collagen solutions were placed in the wells, and a sterile cover slip was placed on top to create a flat upper surface to the collagen gel. The collagen was allowed to polymerize in the wells at 37° C and 5% $C0_2$ for 20 minutes.

The top cover slip was carefully removed, and removable polycarbonate wells (LabTec Chamber Slides) were placed over the gasket. A custom made clamp was used to hold the wells in place and prevent media from leaking (Figure 3-1b,c). 300 μl of vasculogenesis media (formulation in Appendix A-3) was added to each well. We note that the growth media (Appendix A-3), which contains 20% FBS, is the base media for the vasculogenesis assay media. Reduced serum conditions [30] and high serum conditions [31] are both conducive to network formation; however the multitude of proteins and plasminogen inhibitors present in the high serum conditions used in this study could offset the balance between tube formation and tube regression[32]. Because we are investigating the collective cell behavior during the initial network formation (<72 hrs) and we are not particularly concerned with identifying the specific mechanisms of tube regression, we do not believe the high serum concentration is a problem for our study.

After 72 hours in culture, gels and cells were fixed and stained (as described in Appendix A-7) with Alexa Fluor 568 phalloidin, 4',6-diamidino-2-phenylindole (DAPI) (368/461) or YOYO-1 iodide nuclear stain (491/509). Confocal images of the stained 3-D cultures were obtained using a Zeiss 510 Meta confocal microscope (Zeiss, Welwyn Garden City, United Kingdom) with a 63x, NA 1.4 oil immersion objective, a 40x, NA 1.3 oil immersion objective, or a 40x, NA 1.2 water immersion objective (Zeiss) using a pinhole of 1 Airy Unit.

The 3-D vasculogenesis assay described above mimics the *in vivo* process of

vasculogenesis remarkably well. We have demonstrated endothelial cells are able to form a globally interconnected network with open lumen. It is important to note that these networks only form under certain chemical and mechanical conditions. For example, the culture is maintained in vasculogenesis media (formulation in Appendix A-3) which is a "homemade" tumor-conditioned medium known to promote endothelial cell invasion and tube formation[30]. In addition, initial cell-seeding density significantly changes the extent of network formation. In the next section, we discuss our use of cell-seeding density to determine the length scale over which cell-cell interactions occur during network formation.

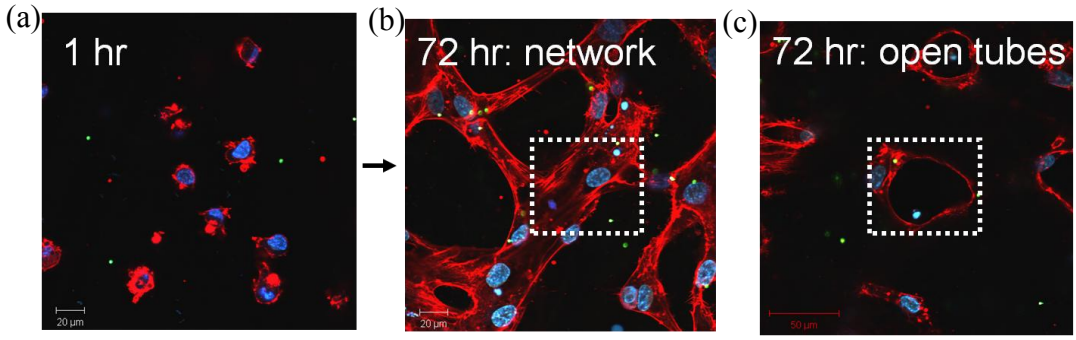

Figure 3-3. Vasculogenesis *in vitro.* Confocal fluorescent images of fixed and stained ECs with AlexaFluor 568 Phalloidin (red=actin) and DAPI (blue=nuclei). (a) The cells are isotropically seeded (at $1x10^6$cells/ml) in the 3-D collagen matrix. Scale bar = 20 μm. (b) After 72 hours of culture, the endothelial cells form a globally connected vascular network near the adherent boundary. Scale bar = 20 μm. (c) In the bulk of the collagen gel, the network contains open tube-like lumens. Same scale as (a) and (b) but scale bar = 50 μm.

3-3 Percolation theory and cell seeding density

The two-dimensional (2-D) percolation threshold for HUVECs that has previously been demonstrated in experiment and modeling is ~ 200 cells/mm^2 [21, 33]. In this cellular 2-D case, the percolation threshold, ρ_c [number of cells/m^2], is the cell density at which a fully connected network occurs in a finite area (Figure 3-4). For all $\rho>\rho_c$, one has a cluster extended from one side of the system to the other. According

to percolation theory, the percolation threshold is the concentration at which an infinite network occurs in an infinite lattice [34], so, because we are dealing with finite systems, the percolation threshold is not sharply defined, and threshold values need to be extrapolated

Using Equation (1),

$$\Delta x_{cells} = \left(\frac{1}{\rho_{cell}} \right)^{1/2} \qquad [1]$$

we calculate that the initial 2-D plating density of 200 cells/mm^2 corresponds to a linear separation between cells of approximately 70 μm implicating a critical length scale of interaction (Figure 3-4). Note that plating cells on top of a substrate like gelatin, fibrin, or collagen at this critical density yields an interconnected network of endothelial cell chords [35-39] which typically do not contain 3-D open lumens.

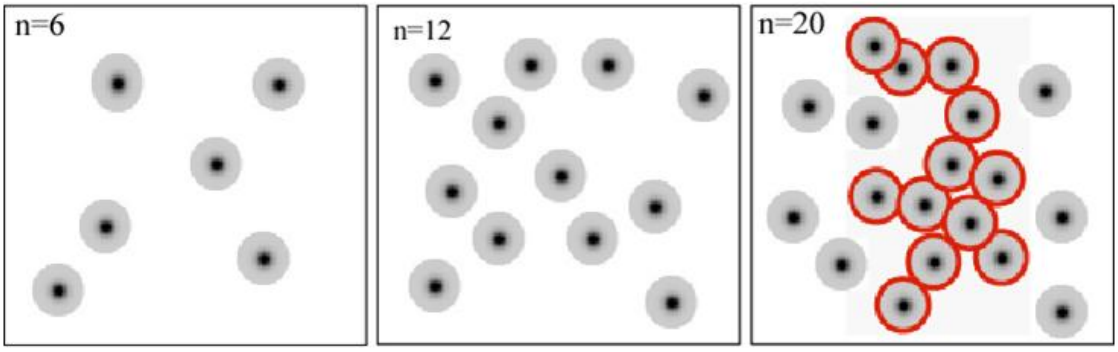

Figure 3-4. Cell density and the percolation threshold. The black circles represent cells and the grey surrounding the cells represents the distance a cell can communicate through its matrix. Percolation theory illustrates the importance of the number of cells in the space and the "radius of action" of each cell for the emergence of a connected network. The percolation threshold implicates a local length scale of cell interaction.

We perform a functional assay of the organization process by altering the cell-seeding density within a 3-D collagen matrix (Figure 3-5). The initial approximate cell-cell spacing can be calculated by

$$\Delta x_{cells} = \left(\frac{1}{\rho_{cell}} \right)^{1/3} \qquad [2]$$

where ρ_{cell} is the cell density [cells/cm^3]. At the start of the vasculogenesis assay (Figure3-5), cells are uniformly distributed throughout the matrix. After 72 hours, networks emerge from the boundary in which the collagen is attached to the glass coverslip (Figure 3-6a). The adherent boundary prevents radial gel contraction even at high cell densities, but cellular traction forces compact the matrix significantly in the axial (z) direction (Figure 3-6). This axial compaction would change the cell

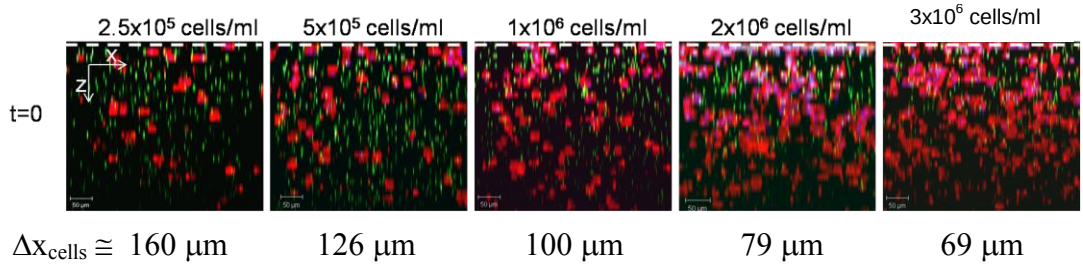

Figure 3-5. Cell density at t=0 . *xz*-plane of fixed and stained endothelial cells (red= actin, blue = nuclei) seeded at different densities in collagen with embedded microspheres (green) at t=0 hours. Dashed white line on the top of each image indicates the adherent boundary. Cells and beads are uniformly distributed throughout the gel at t=0. The fluorescent signal decays as we move into the bulk of the gel (~ 400 microns). Scale bar = 50 μm.

density as well as change the mechanics of the collagen gel over time. For example, the z compaction in gels initially seeded with 5x10^5 cells/ml was 35 ± 10% (Figure 3-6b). At this density at t=0 cell-cell separation would be ~ 126 μm based on Equation [2]; however, at t=72 hours, with the gel compaction taken into account, cell-cell separation would be reduced to ~ 103 μm. Similarly, the z compaction at 2x10^6 cells/ml initial seeding density was 72 ± 5% (Figure 3-6b) which could result in cell-

cell separations of as close as 52 μm. The changing local cell density and matrix mechanics over time in this system make elucidating the exact mechanisms of cell-cell communication during collective cell behavior quite challenging. Therefore, we simply aim to extract an approximate length scale over which cells interact to form a 3-D percolating network and will try to elucidate the mechanisms of cell interactions in the next chapter. Like the 2-D percolation analysis described above, I describe our image analysis to define a percolation threshold for a globally connected 3-D network.

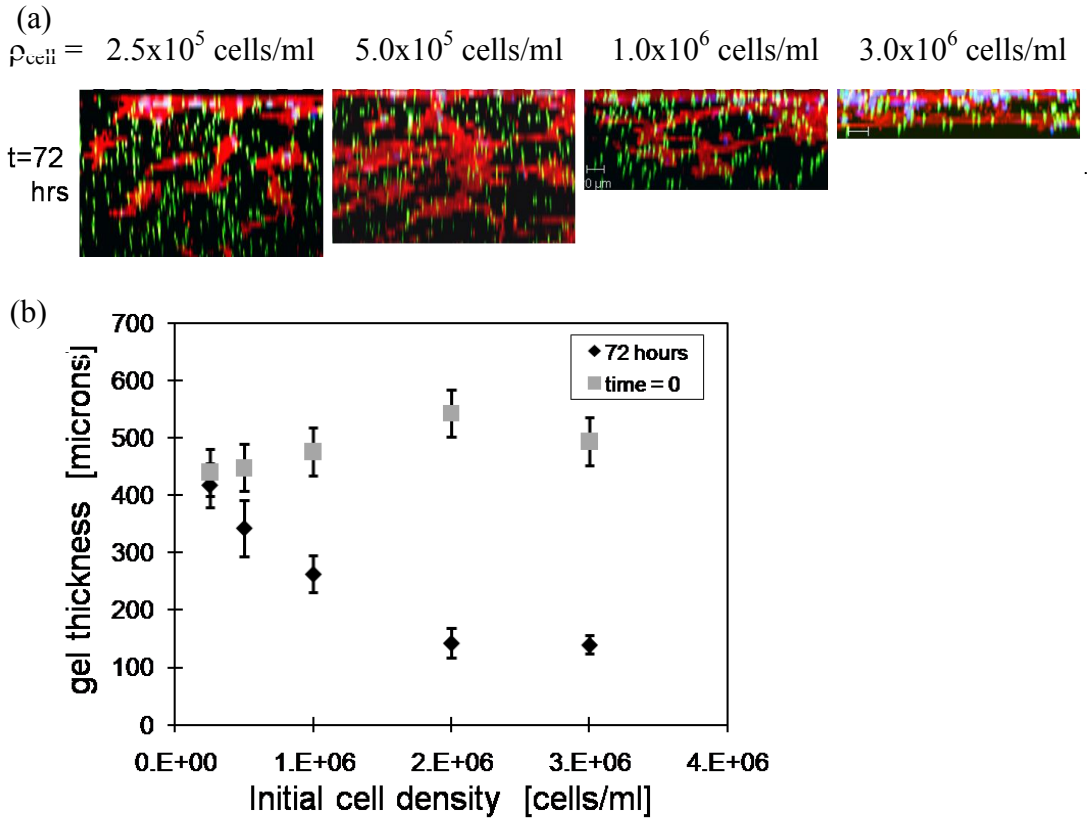

Figure 3-6. Cell density and gel compaction at t=72 hours. (a) *xz*-plane of fixed and stained endothelial cells (red= actin, blue = nuclei) seeded at different densities in collagen with embedded microspheres (green) at t=72 hours. The top of each image indicates the adherent boundary. Scale bar = 50 μm. (b) Quantification of *z*-compaction of collagen gels after 72 hours of culture. Thicknesses were measured using confocal microscopy. Each data point represents at least 5 gels. Error bars represent the standard deviation.

3-4 Percolation analysis and length scale of interaction

The analysis of the *xy* percolation threshold was performed on a single confocal image at the interface of the gel with the bottom glass boundary ($z = 0$). The total area of investigation for *xy* percolation was 2×2 mm^2. 2-D networks were analyzed on the rigid adherent boundary where cells could stretch more due to anchor points and form a semi-2-D network (Figure 3-7a). AlexaFluor 568 phalloidin was used to fluorescently label the F-actin in 72-hour fixed 3D cell-seeded collagen cultures (Figure 3-7a). The images were uniformly thresholded to create a binary image (Figure 3-7b). Image-J was used to identify the following physical properties: number of clusters, area of clusters, void area, void area bounded by the largest structure, and the chord length of the largest cluster before (Figure 3-7b) and after (Figure 3-7c) filling the 'voids'.

We defined the following terms in order to determine if a network percolates a region of interest[34]. A *cluster* was defined as two or more connected cells. The *connectivity parameter* was defined as the area of the largest cluster divided by the total area of the field of view (this is essentially the fraction of the image that is covered by a single connected network). The *percent void area of the largest structure* was defined as the void area bound by the largest cluster. This parameter is an important so as not to count a monolayer as a percolating 'network'. As the network gets more dense, the void area decreases, but should not go to zero if it is to be considered a network. A *percolating network* was defined as a connected cell structure that spanned the system. In the *xy* percolation analysis in the *xy*-plane, system that can be percolated corresponds to the field of view (4 mm^2). In the *z* percolation analysis in the *yz* plane, the system that can be percolated corresponds to the total working distance of the objective (200 μm). The *percolation length* was defined as the greatest chord distance from one edge of a cluster to the other in the

field of view. The *percolation parameter* was defined as the percolation length divided by the maximum percolation length possible (in plane of interest). The percolation parameter, therefore, defines the fractional extent of percolation in the field of view. If the percolation parameter =1 for an *xy* image, the image is percolating in both x and y (since the max length is the diagonal). Percolation occurs

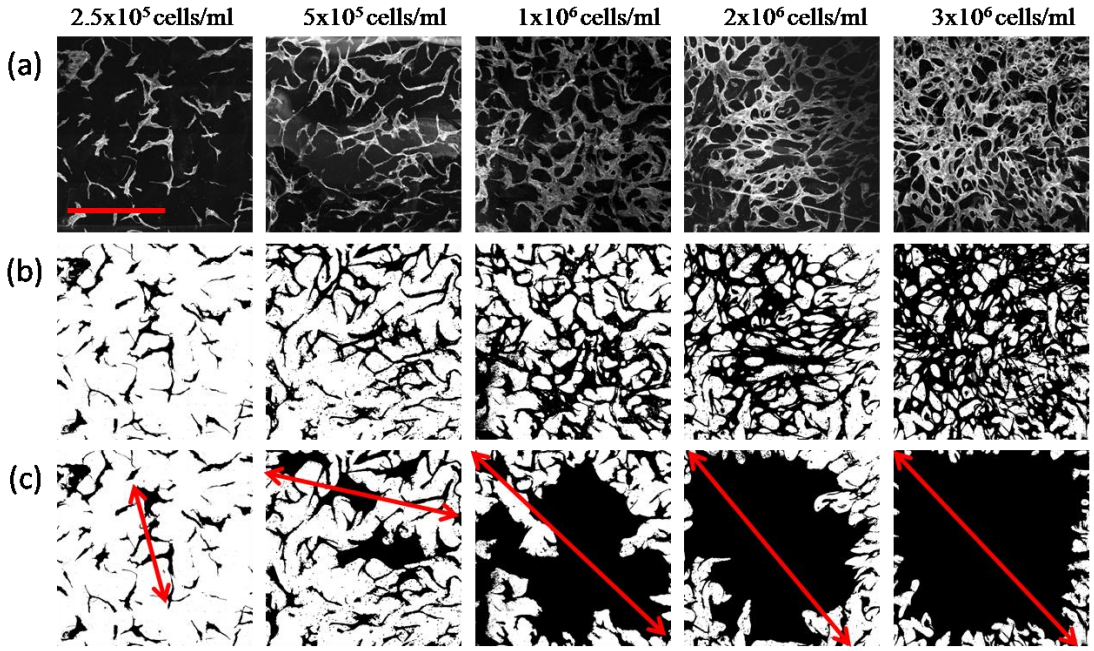

Figure 3-7. 2-D percolation analysis of vascular networks. (a-c) Fluorescence confocal images of ECs seeded in ~500 μm thick collagen gels (attached to bottom boundary) at seeding densities of: $2.5x10^5$, $5.0x10^5$, $1.0x10^6$, $2.0x10^6$, and $3.0x10^6$ cells/ml, shown in columns left to right. Images were captured at the gel-glass interface using a 40x oil immersion lens with a pinhole of 1.0 Airy units. Scale bar = 1 mm. Green and red channels of fluorescence images are shown in (a). Thresholded versions of the images in (a) are shown in (b); thresholded images allow for the automation of the percolation and connectivity analysis and were obtained by thresholding the intensities of the sum of the red and green channels. The largest connected structure identified in the thresholded images (filled in with black) is shown in (c); the maximum chord length of these structures was used to determine the percolation length and parameter.

in *either* x or y (not both) when the percolation parameter = $1/\sqrt{2}$. Connectivity analysis was also performed (data not shown).

The *z* percolation threshold analysis was performed on *z*-projections of a series of images taken at different *z* planes starting at *z* = 0 (cover slip) and moving up to *z* = 0.2mm (working distance of 40x objective) in step sizes of 3-6 μm (Fig 5a). Analysis was performed as described above with Image J (Fig 5b,c), and the parameters defined for the 2D/*xy* percolation analysis above were applied to the 3-D image stack. If a connected network spanned the entire z direction (thickness of gel; percolation parameter ≥ 1), the network was considered percolated in the *z* direction. If a 3-D cell seeded scaffold contained an actin network that percolated in both the 2D/*xy* plane and the *z* plane, it was considered to be a 3-D percolating structure.

Image and percolation analysis show that *xy* percolation (over an area of 4mm^2) occurs when at least 5.0×10^5 cells/ml are seeded into a collagen matrix (left

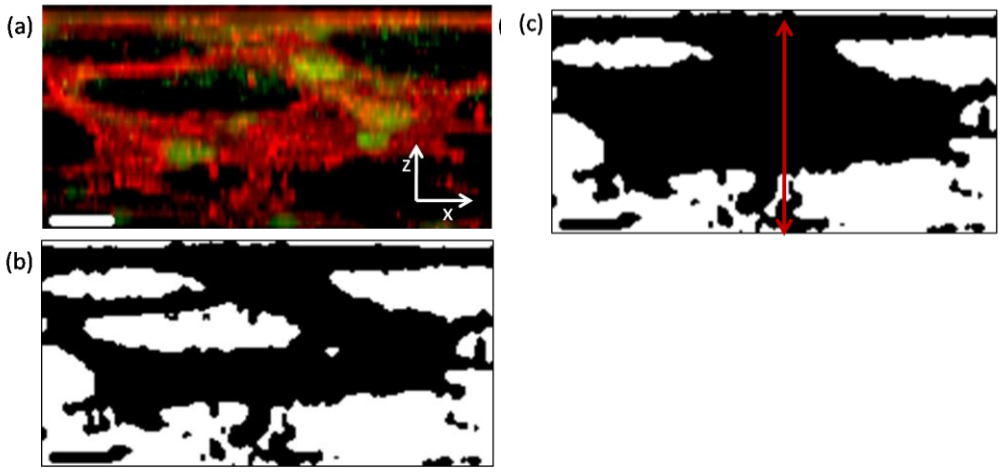

Figure 3-8. *z* percolation analysis for network formation within 0.3% collagen matrices. (a) A *yz* plane (adherent boundary is at the top of the image) from a confocal *z*-stack of an initially 500 μm thick collagen gel seeded with 2×10^6 cells/ml. Scale bar = 20 μm. (b) *z* percolation was measured as described in Figure 3-7 except by analyzing the *yz*-plane instead of the *xy*-plane. (c) The *z* percolation length was determined by measuring the length of the largest connected structure in the *z* direction. (1-D in nature).

shaded region in Figure 3-9). *z* percolation of an initially ~500 μm thick gel (Figure 3-8) occurs when the initial seeding density is $2.0x10^6$ cells/ml (right shaded region in Figure 3-9). The *z* percolation threshold of $2x10^6$ cells/ml initial seeding density implicates a length scale of local cell-cell interactions within the bulk of the soft 3-D collagen gel to be ~79 microns or less (Eq. 2)

Note that the *xy* and *z* percolation analyses are not equivalent in that the *z*-analysis is essentially 1-D, and the *xy* analysis is 2-D. We are primarily concerned with the fully 3-D percolation threshold which would occur when both the *xy* and *z*-percolation thresholds are met. Due to factors mentioned above such as gel compaction (Figure 3-6) we can only estimate the relevant length scale of interaction for 3-D percolation to be within the range of 50-100 μm.

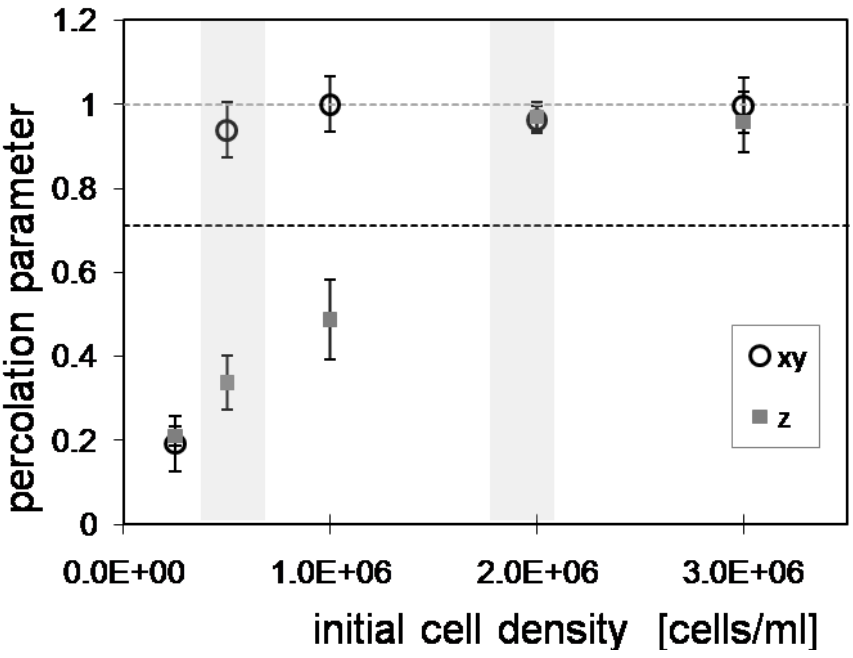

Figure 3-9. Percolation thresholds in *xy* and *z*. Percolation occurs in either the *x* or *y* plane when the percolation parameter = $1/\sqrt{2}$ (black dashed line). Percolation occurs in three-dimensions when both *xy* and *z*-percolation parameters = 1 (grey dashed line). Data represent average ± the standard deviation for at least 3 different gels.

3-6 The effects of tetradecanoyl phorbol acetate (TPA) (a.k.a. phorbol-12-myristate-13-acetate (PMA))

To study the percolation threshold in 3-D collagen matrices as described above, we culture the 3-D cell cultures in a vasculogenesis (Appendix A-3) media which is a "homemade" tumor-conditioned media. (The full list of ingredients of this media can be found in Appendix A-3.) The growth factor components of the media include VEGF, bFGF, and a molecule called tetradecanoyl phorbol acetate (TPA) (which is also known by the name phorbol-12-myristate-13-acetate (PMA)). Unlike VEGF, if we omit TPA from our vasculogenesis media, no network formation takes place (Figure 3-10). VEGF and FGF are well-known tumor secreted growth factors that stimuli angiogenesis; however, TPA is a less well-known molecule. Interestingly, it is a plant-derived molecule that promotes tumorgenesis. Because it is the critical soluble factor that we add to our experiments, we did a background study on the molecule, TPA. In this section, we describe how TPA was discovered, its effects, and the possible molecule mechanisms behind the tumor promoting agent.

In 1941, Berenblum[40] discovered that croton oil (from the seed of Croton tiglium L.) is a potent tumor promoter. He showed that it markedly augments carcinogenesis when applied at weekly intervals to the skin of mice, and over the next several years, croton oil was used for studying the mechanisms of carcinogenesis[41, 42]. Many attempts were also made to isolate, purify, and identify the active compounds responsible for the oil's tumor enhancing ability. Van Durren et al. first isolated and determined the structures of the two main active materials in the purified crystalline material obtained from the croton seed. The main product obtained from the tumor-enhancing fraction of the croton resin was a fatty acid ester of a polyphenol. [43, 44]. This phorbol ester was then made into the final purified form, phorbol

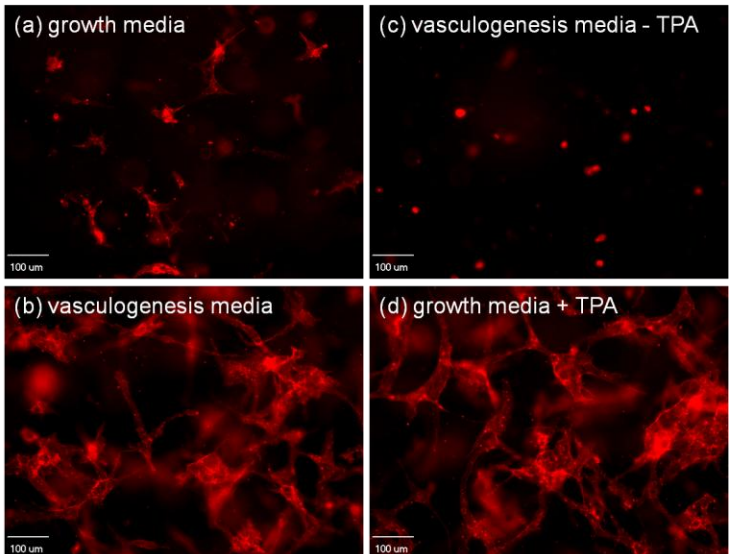

Figure 3-10. TPA and network formation. Confocal fluorescent images of fixed and stained ECs with AlexaFluor 568 Phalloidin (red=actin) at 72 hours. Cells were seeded at a density of $1x10^6$cells/ml in the 3-D collagen matrix. Scale bar = 100 μm. (a) When cultured in just growth media (no VEGF, FGF or TPA) no network forms. (b) In complete vasculogenesis media, a network forms. (c) When cultured in just vasculogenesis media without the TPA but with VEGF and FGF, no network forms. (d) When only TPA is added to growth media, networks form similar to (b).

myristate acetate (PMA), by treating with acetic anhydride and myristoyl chloride[45]. PMA was shown to cause epidermal inflammation, hyperplasia and tumor promotion in treated skin.

In 1970, Troll et al. demonstrated that specific inhibitors of proteases suppressed the promotion of tumors by PMA, indicating that proteases may be important in the mechanisms of carcinogenesis and phorbol esters [46]. In light of Troll's findings, Weinstein and Wigler[47] tested the effects of PMA on plasminogen activator (PA) levels in cells *in vitro*. They show that PMA induces plasminogen activator, also known as tPA. Interestingly, many transformed cell lines are high producers of plasminogen activator, and tPA production leads to increased cell migration and loss of anchorage dependent growth.

Based these initial findings by Weinstein and Wigler and Troll et al., others

began investigating tPA and collagenase production by cultured endothelial cells, and the effects that phorbol esters had on protease activity[48-51]. Results showed that addition of the tumor promoting PMA (also called tetradecanoyl phorbol acetate, TPA) to the culture medium stimulated the secretion of collagenase and tPA activity by 5-30 fold.

It had been known that an important event during angiogenesis is the invasion of the ECM by sprouting endothelial cells (ECs). To investigate the role of proteases in EC invasiveness *in vitro*, Orci et al., treated (ECs) grown on a layer of collagen with PMA/TPA. They verified that the phorbol ester increased collagenase and tPA activity, and showed that this increased production of proteases allowed the ECs to invade the collagen and form an extensive network of tube-like structures[52].

Extensive work has been performed in order to determine the molecular mechanisms behind tumor promoting agents including commonly known growth factors, VEGF and bFGF, and also phorbol esters. In 1980, Nishizuka published a review in Nature that described the roles of protein kinase C (PKC) in tumor promotion[53]. PKC was discovered in 1977 as a proteolytically activated kinase in many tissues. It was shown that it was a calcium activated phospholipids-dependent enzyme, and diacylglycerol (DAG) greatly increased the affinity of PKC for calcium, effectively activating PKC. DAG is not normally found in membranes but is transiently produced from inositol phospholipids in response to extracellular signals.

PKC has been shown to be a target for phorbol esters [7, 54]. TPA has a diacylglycerol-like structure and can substitute for diacylglycerol (the activating component for PKC) (Figure 3-11).

It has also been established that phorbol esters and VEGF[55] both activate the MAPK pathway in cells. The MAPK pathway plays a prominent role in regulating

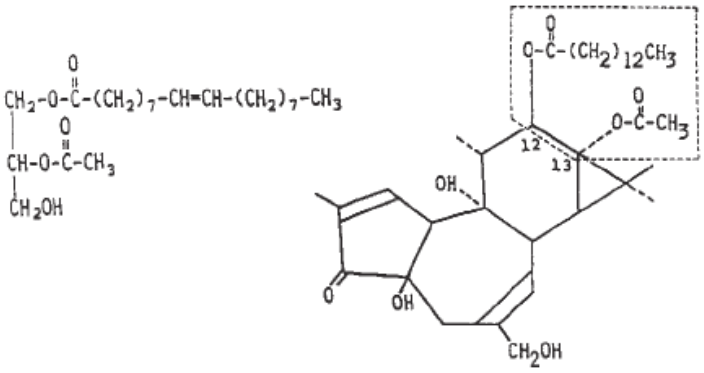

Figure 3-11. Structures of synthetic diacylglycerol (left) and TPA (right). TPA has a diacylglycerol-like structure and can substitute for diacylglycerol and increase PKC's affinity of calcium, thus activating PKC. (image from [7]).

many cellular processes that are important during vascular development including migration, chemotaxis, cell survival, cell shape, cell polarity, and proliferation. Several routes lead to the activation of MAPK[2, 3] (Figure 3-12). Koh et al[1]. showed TPA activates PKC, which in turn regulated Pak2 and Pak4 phosphorylation, promoting lumen and tube formation. It is not clear if the Pak2 and Pak4 go on to activate the MAPK pathway or influence cell behavior through a different mechanism.

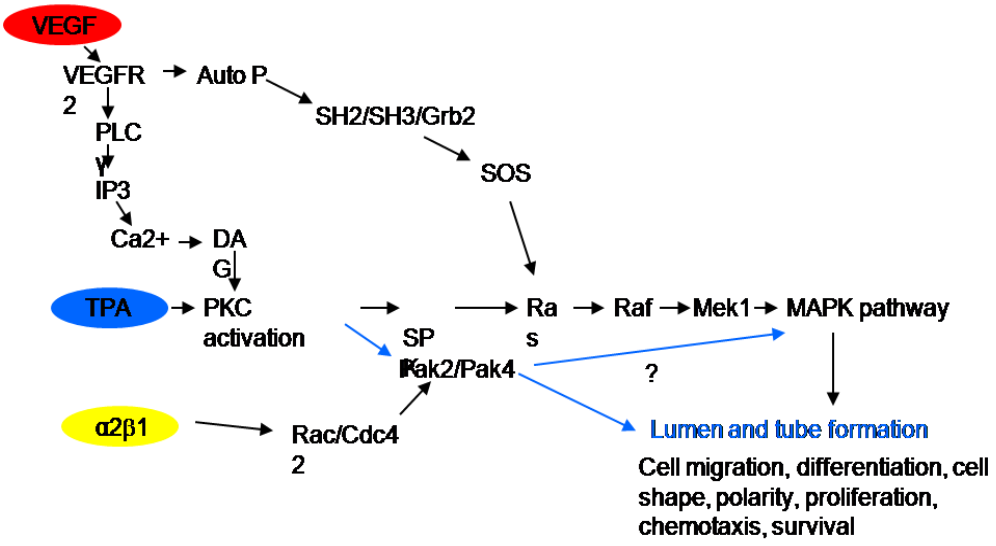

Figure 3-12. TPA signaling pathway based on [1-3]. MAPK: mitogen-activated protein kinase. DAG: diacylglycerol. PLC: phospholipase C. IP3: inositol triphosphate.

3-5 Mechanics and tensegrity perspective

In this section, we briefly describe how our endothelial cell networks possess characteristics of tensegrity structures [56, 57]. As you can see in Figure 3-13, a network attached to an adherent edge (like a spider web) is under tension. If released from the adherent edge, it retracts. A true tensegrity structure has cords which are the tensile elements and struts which are the compressive elements that can carry a mechanical load [58] (Figure 3-14a). We believe the cells act as the cords and the adherent boundary, whether the *xy* plane (3-14b,c) or simply an edge (as in Figure 3-13), acts as the mechanical component in a tensegrity model.

Recall that at very high seeding densities we see a large degree of axial compaction of the matrix (Figure 3-6). Interestingly, only at these high seeding densities, do we begin to see networks extending into the *z* direction (Figure 3-14b), indicating that the compacted matrix, like a tent pole (Figure 3-14c), could be serving

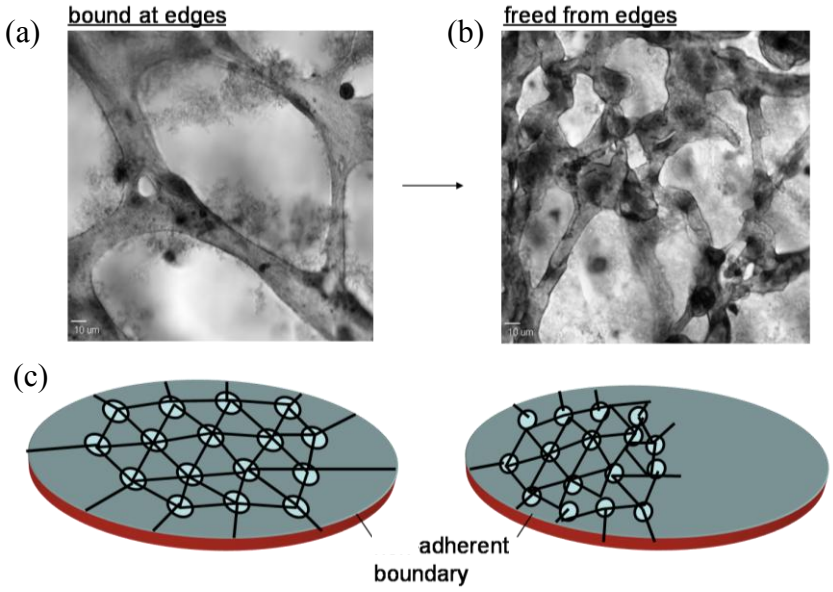

Figure 3-13. A cellular network under tension. (a) Multicellular network that is attached at the edges and not in the xy plane. (b) When manually freed from the adherent edge (with a pipette tip), the network retracts. (c) Schematic of network retracting.

as the mechanical component, or strut, holding up the network. In fact if we quantify the global mechanics of the system with confined compression (Chapter 2) we can extract an equilibrium modulus of our gels both before and after the cells compact them. Initially the modulus of a cell-seeded 0.3% collagen gel is ~ 50 Pa (Chapter 2) whereas after 72 hours, the modulus increases to ~ 1000 Pa (data not shown) Based on traction force microscopy measurements[9], endothelial cells in 2D exert about 1000 Pa on their surroundings indicating that the matrix in its final state would be strong enough to support a 3-D network under tension.

Our ideas presented above regarding vascular networks at tensegrity structures are preliminary and require further investigation and testing.

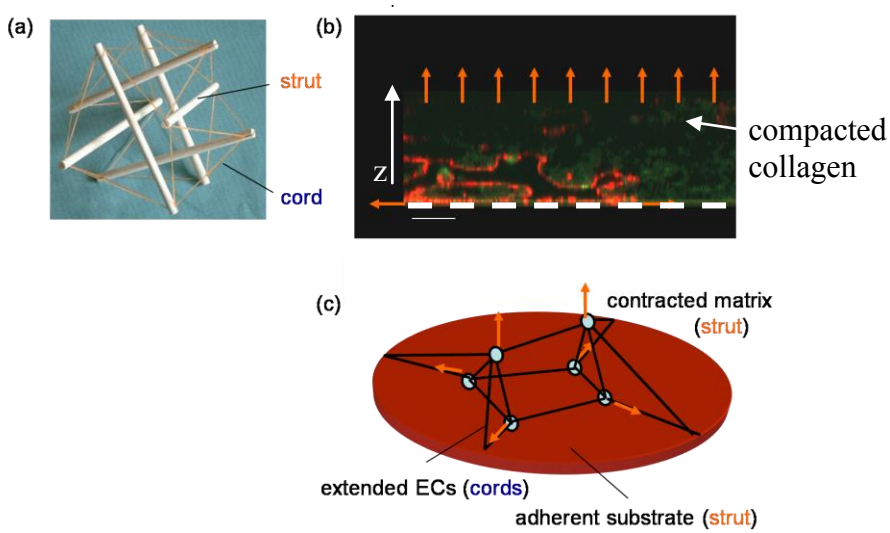

Figure 3-14. 3-D network as a tensegrity structure. (a) A physical model of a tensegrity structure with struts (compressive elements) and cords (tensile elements). (b) ECs were seeded in type I collagen at $3x10^6$ cells/ml and cultured for 72 hours. Cells were fixed and F-actin was stained using Alexa Fluor 568 phalloidin. Scale bar = 50 μm. Significant *z* direction compaction of the collagen matrix occurred during the 72 hour culture time. The image in (b) shows a confocal *yz* plane of a 3-D vascular network emerging from an adherent bottom boundary(dashed white line). Red arrows indicate that the compacted collagen matrix and the adherent substrate could be acting as compressive elements (struts) a while the cell network is acting as the element under tension. (c) Schematic representation of (b).

3-6 Conclusions

By altering the cell-seeding density within 3-D collagen matrices, we have performed a simple assay of the cellular self-organizational process. We used the concepts from general percolation theory and estimated a 3-D percolation threshold cell density by analyzing the global connectivity of the vascular network that formed in both the *xy*- and *z*- planes of our system. The *xy* percolation threshold was performed on the network that organized on the adherent bottom boundary. At this boundary, a semi-2-D plexus formed (Figure 3-7). The network contained open lumen structures in the third dimension, and the entire network emerged from the boundary into the bulk of the matrix. Interestingly the extended and connected network on this boundary formed only when the collagen was physically adhered to the bottom boundary. A critical seeding density of $5x10^5$ cells/ml (this density corresponds to ~ 126 μm cell center to cell center initial separation) was required for a percolating network (Figure 3-9).

We then analyzed the *z*-plane to determine the seeding density at which a network would span the entire thickness of the matrix and found an initial seeding density of $2x10^6$ cells/ml required for a network to span the *z* plane (gel thickness) (Figure 3-8 and 3-9). We defined the 3-D percolation threshold to be the cell seeding density at which both a *xy* and *z* percolating network exists; thus, our estimate for 3-D percolation corresponds to an initial cell-cell separation of ~ 79 μm.

This percolation threshold implicates a local length scale associated with the cell-cell interactions through the matrix. With only endpoint experiments, as presented in this chapter, this length scale of cell-cell interactions is not well defined. The cell-cell separation of ~ 79 μm could be associated with the extent of cell migration, the amount a cell can stretch, or an "action-at-a-distance" mechanism that propagates through the collagen matrix. The work reported in this chapter leads us to

additional experiments, reported in Chapters 4 and 5, designed to determine the origin(s) of this length scale.

In addition to providing a starting point for studying the mechanisms of cell-cell interactions, our percolation structural analysis allows us to quantify connected structures and to evaluate the potential of our network to perform as a functional transport system. To engineer a useful vascular network for tissue engineering purposes, the *in vitro* plexus must possess, at minimum, the following physical characteristics: 1) a percolating network with a high density of intersections, 2) the mechanical stability and geometry necessary for perfusion, and 3) open lumen. Once a flow has been introduced, the open lumens provide the means for convective mass transfer, fluid mechanics, and global scale communication throughout a system, all of which are crucial for delivery within and maturation of a vascular plexus.

Our percolation assay is a critical first step towards advancing these criteria as the 3-D tube formation assay has conventionally been used as a system in which chemicals are simply interrogated with respect to their angiogenic activation or suppression potential. The conventional, relatively low seeding density used in these assays is sufficient to ask these types of "yes" or "no" questions. Our 3-D percolation analysis has shown that the conventional seeding density ($1x10^6$cells/ml) is inadequate for the purpose of creating an interconnecting network, and thus, inadequate for creating a functional microvascular system.

In addition to the percolation threshold, we hypothesize that the *xy* rigid adherent boundary acts as a 2-D mechanical strut (Figure 3-14) which supports the extensive 2-D network observed under that condition (Figure 3-7). It appears that a percolating network is under tension (Figure 3-13), and a network under tension would need a mechanical component to keep from collapsing. We propose that the *xy* percolating vascular plexus resembles a tensegrity structure whereby the cell network

is the tensile element and the adherent bottom boundary acts as the mechanical strut. Likewise, we believe that the contracted, mechanically robust matrix (Figure 3-6) acts as the compressive element for the 3-D network observed at the high cell densities.

The collective cell behavior we have observed and have begun to characterize is an elegant and interesting example of cellular self-organization. The mechanisms of how individual cells communicate to form a globally organized network remain unclear. One of the most basic outstanding questions is whether or not cells interact at a distance through their extracellular matrix. A simple "yes" or "no" answer to this question may not be reasonable, and thus, the relative importance of "action-at-a-distance" as compared to cell-cell contact may be a more realistic question to ask. In the following chapter, we begin to address these questions by turning to assays which utilize a low cell-seeding density and live cell imaging so we can observe cell behaviors in real time. Then in Chapter 5, we extend beyond the basic question of action at a distance and work to determine the specific mechanisms that may be influence cell-cell communication.

REFERENCES

1. Koh, W., R.D. Mahan, and G.E. Davis, *Cdc42- and Rac1-mediated endothelial lumen formation requires Pak2, Pak4 and Par3, and PKC-dependent signaling.* J Cell Sci, 2008. **121**(Pt 7): p. 989-1001.

2. Tallquist, M.D., P. Soriano, and R.A. Klinghoffer, *Growth factor signaling pathways in vascular development.* Oncogene, 1999. **18**(55): p. 7917-32.

3. Taylor, C.J., K. Motamed, and B. Lilly, *Protein kinase C and downstream signaling pathways in a three-dimensional model of phorbol ester-induced angiogenesis.* Angiogenesis, 2006. **9**(2): p. 39-51.

4. Risau, W. and I. Flamme, *Vasculogenesis.* Annu Rev Cell Dev Biol, 1995. **11**: p. 73-91.

5. Drake, C.J., *Embryonic and adult vasculogenesis.* Birth Defects Res C Embryo Today, 2003. **69**(1): p. 73-82.

6. Coffin, J.D. and T.J. Poole, *Endothelial cell origin and migration in embryonic heart and cranial blood vessel development.* Anat Rec, 1991. **231**(3): p. 383-95.

7. Yamanishi, J., et al., *Synergistic functions of phorbol ester and calcium in serotonin release from human platelets.* Biochem Biophys Res Commun, 1983. **112**(2): p. 778-86.

8. Rupp, P.A., A. Czirok, and C.D. Little, *alphavbeta3 integrin-dependent endothelial cell dynamics in vivo.* Development, 2004. **131**(12): p. 2887-97.

9. Reinhart-King, C.A., M. Dembo, and D.A. Hammer, *Cell-cell mechanical communication through compliant substrates.* Biophys J, 2008. **95**(12): p. 6044-51.

10. Gerhardt, H., et al., *VEGF guides angiogenic sprouting utilizing endothelial tip cell filopodia.* J Cell Biol, 2003. **161**(6): p. 1163-77.

11. Bach, T.L., et al., *VE-Cadherin mediates endothelial cell capillary tube formation in fibrin and collagen gels.* Exp Cell Res, 1998. **238**(2): p. 324-34.

12. Carmeliet, P., et al., *Targeted deficiency or cytosolic truncation of the VE-cadherin gene in mice impairs VEGF-mediated endothelial survival and angiogenesis.* Cell, 1999. **98**(2): p. 147-57.

13. Vittet, D., et al., *Targeted null-mutation in the vascular endothelial-cadherin gene impairs the organization of vascular-like structures in embryoid bodies.* Proc Natl Acad Sci U S A, 1997. **94**(12): p. 6273-8.

14. Kamei, M., et al., *Endothelial tubes assemble from intracellular vacuoles in vivo.* Nature, 2006. **442**(7101): p. 453-6.

15. Davis, G.E., W. Koh, and A.N. Stratman, *Mechanisms controlling human endothelial lumen formation and tube assembly in three-dimensional extracellular matrices.* Birth Defects Res C Embryo Today, 2007. **81**(4): p. 270-85.

16. Poole, T.J., E.B. Finkelstein, and C.M. Cox, *The role of FGF and VEGF in angioblast induction and migration during vascular development.* Dev Dyn, 2001. **220**(1): p. 1-17.

17. Bautch, V.L. and C.A. Ambler, *Assembly and patterning of vertebrate blood vessels.* Trends Cardiovasc Med, 2004. **14**(4): p. 138-43.

18. Drake, C.J., et al., *VEGF regulates cell behavior during vasculogenesis.* Dev Biol, 2000. **224**(2): p. 178-88.

19. Roman, B.L. and B.M. Weinstein, *Building the vertebrate vasculature: research is going swimmingly.* Bioessays, 2000. **22**(10): p. 882-93.

20. Czirok, A., B.J. Rongish, and C.D. Little, *Extracellular matrix dynamics during vertebrate axis formation.* Dev Biol, 2004. **268**(1): p. 111-22.

21. Serini, G., et al., *Modeling the early stages of vascular network assembly.* Embo J, 2003. **22**(8): p. 1771-9.

22. Ingber, D.E., *Mechanical signaling and the cellular response to extracellular matrix in angiogenesis and cardiovascular physiology.* Circ Res, 2002. **91**(10): p. 877-87.

23. Namy, P., J. Ohayon, and P. Tracqui, *Critical conditions for pattern formation and in vitro tubulogenesis driven by cellular traction fields.* J Theor Biol, 2004. **227**(1): p. 103-20.

24. Davis, G.E. and C.W. Camarillo, *An alpha 2 beta 1 integrin-dependent pinocytic mechanism involving intracellular vacuole formation and coalescence regulates capillary lumen and tube formation in three-dimensional collagen matrix.* Experimental Cell Research, 1996. **224**(1): p. 39-51.

25. Davis, G.E. and W.B. Saunders, *Molecular balance of capillary tube formation versus regression in wound repair: role of matrix metalloproteinases and their inhibitors.* J Investig Dermatol Symp Proc, 2006. **11**(1): p. 44-56.

26. Davis, G.E. and D.R. Senger, *Endothelial extracellular matrix - Biosynthesis, remodeling, and functions during vascular morphogenesis and neovessel stabilization.* Circulation Research, 2005. **97**(11): p. 1093-1107.

27. Bornstein, M.B., *Reconstituted rattail collagen used as substrate for tissue cultures on coverslips in Maximow slides and roller tubes.* Lab Invest, 1958. **7**(2): p. 134-7.

28. Davis, G.E. and C.W. Camarillo, *An alpha 2 beta 1 integrin-dependent pinocytic mechanism involving intracellular vacuole formation and coalescence regulates capillary lumen and tube formation in three-dimensional collagen matrix.* Exp Cell Res, 1996. **224**(1): p. 39-51.

29. Ng, C.P. and M.A. Swartz, *Fibroblast alignment under interstitial fluid flow using a novel 3-D tissue culture model.* American Journal of Physiology-Heart and Circulatory Physiology, 2003. **284**(5): p. H1771-H1777.

30. Davis, G.E., S.M. Black, and K.J. Bayless, *Capillary morphogenesis during human endothelial cell invasion of three-dimensional collagen matrices.* In Vitro Cell Dev Biol Anim, 2000. **36**(8): p. 513-9.

31. Ng, C.P., C.L.E. Helm, and M.A. Swartz, *Interstitial flow differentially stimulates blood and lymphatic endothelial cell morphogenesis in vitro.* Microvascular Research, 2004. **68**(3): p. 258-264.

32. Davis, G.E., et al., *Matrix metalloproteinase-1 and -9 activation by plasmin regulates a novel endothelial cell-mediated mechanism of collagen gel contraction and capillary tube regression in three-dimensional collagen matrices.* J Cell Sci, 2001. **114**(Pt 5): p. 917-30.

33. Ambrosi, D., Bussolino, F., Preziosi, L., *A Review of Vasculogenesis Models.* 2004.

34. Stauffer, D., Aharony, A., *Introduction to Percolation Theory*. 2nd ed. 1992, Philadelphia, PA: Taylor and Francis, Inc.

35. Davis, G.E. and C.W. Camarillo, *Regulation of Endothelial-Cell Morphogenesis by Integrins, Mechanical Forces, and Matrix Guidance Pathways.* Experimental Cell Research, 1995. **216**(1): p. 113-123.

36. Haudenschild, F.a., *Angiogenesis in vitro.* Nature, 1980. **288**: p. 551-556.

37. Ingber, D.E. and J. Folkman, *Mechanochemical Switching between Growth and Differentiation During Fibroblast Growth Factor-Stimulated Angiogenesis Invitro - Role of Extracellular-Matrix.* Journal of Cell Biology, 1989. **109**(1): p. 317-330.

38. Tranqui, L. and P. Tracqui, *Mechanical signalling and angiogenesis. The integration of cell-extracellular matrix couplings.* C R Acad Sci III, 2000. **323**(1): p. 31-47.

39. Gamba, A., et al., *Percolation, morphogenesis, and burgers dynamics in blood vessels formation.* Phys Rev Lett, 2003. **90**(11): p. 118101.

40. Berenblum, I., *The cocarcinogenic action of croton resin.* Cancer Res, 1941. **1**(44).

41. Berenblum, I. and P. Shubik, *The persistence of latent tumour cells induced in the mouse's skin by a single application of 9:10-dimethyl-1:2-benzanthracene.*

Br J Cancer, 1949. **3**(3): p. 384-6.

42. Armuth, V. and I. Berenblum, *Phorbol as a possible systemic promoting agent for skin carcinogenesis.* Z Krebsforsch Klin Onkol Cancer Res Clin Oncol, 1976. **85**(1): p. 79-82.

43. Vanduuren, B.L., E. Arroyo, and L. Orris, *The Tumor-Enhancing and Irritant Principles from Croton Tiglium L.* J Med Chem, 1963. **6**: p. 616-7.

44. Vanduuren, B.L., L. Orris, and E. Arroyo, *Tumour-Enhancing Activity of the Active Principles of Croton Tiglium L.* Nature, 1963. **200**: p. 1115-6.

45. Vanduuren, B.L.a.O., L., *The Tumor-enhancing Principles of Croton tiglium L.* Cancer Res, 1965. **25**.

46. Troll, W., A. Klassen, and A. Janoff, *Tumorigenesis in mouse skin: inhibition by synthetic inhibitors of proteases.* Science, 1970. **169**(951): p. 1211-3.

47. Wigler, M. and I.B. Weinstein, *Tumour promotor induces plasminogen activator.* Nature, 1976. **259**(5540): p. 232-3.

48. Moscatelli, D., E. Jaffe, and D.B. Rifkin, *Tetradecanoyl phorbol acetate stimulates latent collagenase production by cultured human endothelial cells.* Cell, 1980. **20**(2): p. 343-51.

49. Gross, J.L., et al., *Plasminogen activator and collagenase production by cultured capillary endothelial cells.* J Cell Biol, 1982. **95**(3): p. 974-81.

50. Shi, G.Y., et al., *Plasmin and the regulation of tissue-type plasminogen activator biosynthesis in human endothelial cells.* J Biol Chem, 1992. **267**(27): p. 19363-8.

51. Gross, J.L., D. Moscatelli, and D.B. Rifkin, *Increased capillary endothelial cell protease activity in response to angiogenic stimuli in vitro.* Proc Natl Acad Sci U S A, 1983. **80**(9): p. 2623-7.

52. Montesano, R. and L. Orci, *Tumor-promoting phorbol esters induce*

angiogenesis in vitro. Cell, 1985. **42**(2): p. 469-77.

53. Nishizuka, Y., *The role of protein kinase C in cell surface signal transduction and tumour promotion.* Nature, 1984. **308**(5961): p. 693-8.

54. Castagna, M., et al., *Direct activation of calcium-activated, phospholipid-dependent protein kinase by tumor-promoting phorbol esters.* J Biol Chem, 1982. **257**(13): p. 7847-51.

55. Yoshiji, H., et al., *Protein kinase C lies on the signaling pathway for vascular endothelial growth factor-mediated tumor development and angiogenesis.* Cancer Res, 1999. **59**(17): p. 4413-8.

56. Ingber, D.E., *Tensegrity-based mechanosensing from macro to micro.* Prog Biophys Mol Biol, 2008. **97**(2-3): p. 163-79.

57. Wang, N., et al., *Mechanical behavior in living cells consistent with the tensegrity model.* Proc Natl Acad Sci U S A, 2001. **98**(14): p. 7765-70.

58. Ingber, D.E., *Cellular tensegrity: defining new rules of biological design that govern the cytoskeleton.* J Cell Sci, 1993. **104 (Pt 3)**: p. 613-27.

CHAPTER 4

LOCAL CELL-CELL INTERACTIONS AND DYNAMICS WITHIN 3-D COLLAGEN SCAFFOLDS

4-1 Introduction

In Chapter 3, we studied the collective behavior and self-organization of a large number of cells. In this chapter, we look further into the origins of this length scale of interaction defined through collective cell behavior to the mechanisms of local cell-cell interactions that occur during 3-D vasculogenesis *in vitro* using low seeding densities and live cell imaging.

Individual endothelial cells interact with each other and their extracellular matrix microenvironment during their organization into a vascular network. Chemical gradients [1], mechanical interactions [2], and cell-cell contact[3] have been implicated in vascular network formation, but the distinct roles and relative importance of these stimuli remain unclear.

Although the *in vivo* microenvironment of cells is three dimensional (3-D) in nature, most cell-cell interaction studies have been performed in two dimensions (2-D). Cells have been shown to behave very differently in a 2-D environment as compared to a 3-D environment. For example, studies primarily using fibroblasts [4, 5] and tumor cells [6, 7] embedded in 3-D collagen matrices have been used to show the effects of 3-D culture on cell migration, contact guidance, matrix degradation, and cell traction forces. Differences between 2-D and 3-D have been demonstrated in changes in cell morphology, adhesion, migration, and cell-cell communications as well as in cell contractility and cellular-induced matrix deformations[8]. Chemoattraction (specifically towards VEGF) has been implicated as a fundamental mechanism of endothelial cell-cell communication in 2-D [1], but, similar to the

transfer of stress through a 3-D matrix, the complicated nature of the transfer of mass through 3-D matrices makes understanding the biochemical signals that dictate cell behavior in 3-D is a significant challenge.

To investigate local cell-cell interactions in 3-D, we study the behavior of isolated cells and cell pairs embedded in a type I collagen matrix (Figure 4-1). In the following sections of this chapter, I will describe our use of live time-lapse microcopy and our analysis of migration and protrusions (Figure 4-1b) sent out by endothelial cells when cells are isolated and near another cell in order to define a critical length scale of interaction between cells. By subjecting the cells to different chemical conditions, we aim to determine if cells communicate via chemical gradients, mechanics, or contact.

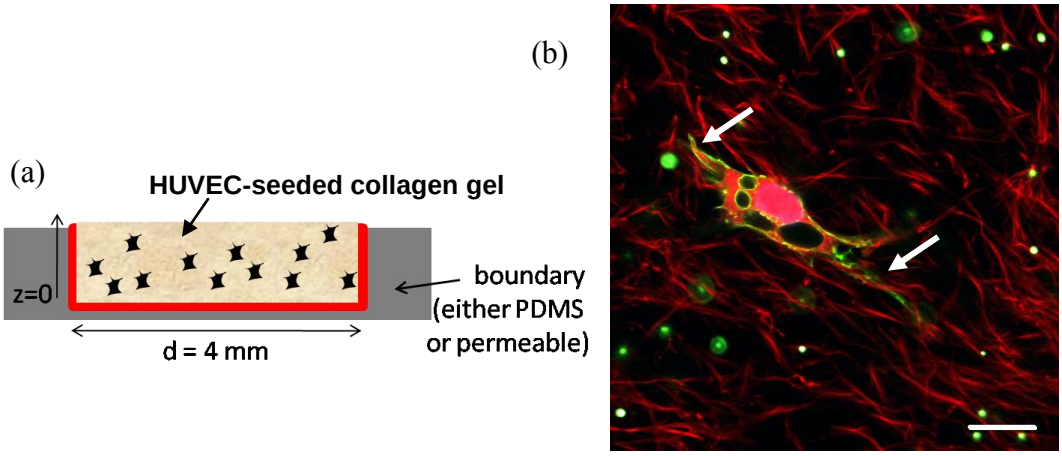

Figure 4-1. (a) Schematic diagram of system used for live imaging/protrusion analysis experiments. HUVEC-seeded constructs are polymerized in a well and submerged in vasculogenesis media (formulation in Appendix A) during culture. (b) A confocal fluorescent image of an isolated cell in a fluorescently labeled collagen matrix. Arrows indicate cellular protrusions. Actin is stained with Alexa Fluor phalloidin 488, and the nucleus is stained with DAPI. Scale bar = 20 μm

4-2 Platform for live cell imaging

To capture the behaviors of living cells within the collagen matrix, brightfield images were captured every 10 minutes using a Hamamatsu ORCA-ER camera

(Bridgewater, NJ) mounted on an Olympus IX81 microscope with a 40x LWD objective. A large humidified incubator mounted on the microscope stage (Weather Station by Precision Control) was used to maintain a temperature of 37°C. A smaller, custom-made Plexiglas chamber, lined with wet paper towels, was used in order to maintain humidity around the 3-D cell culture scaffold. A 5% CO_2 gas cylinder (mixed with air) was bubbled through a column of water and flowed directly into the small custom chamber. Flow rate was regulated to keep the small chamber around the cells at 5% CO_2.

4-3 Migration behavior of ECs in 3-D collagen matrix

To understand cell-cell interactions, we first worked to determine the primary strategy that the endothelial cells use to locate other cells in the 3-D matrix. The two general mechanisms that we investigated were cell migration and filopodial protrusion activity. The migration of endothelial precursor cells during embryonic development has been shown to be a key mechanism in the process of vascular development [9]; however, we wanted to use our live cell imaging to visualize and quantify if the cells in our 3-D system migrated significantly from their initial position. It has been suggested that there are two major strategies for migration through 3-D matrices [10]. Migrating cells 1) use highly localized and controlled proteolysis that cleaves matrix fibers so that the cell body can migrate, and/or 2) are able to migrate independent of proteolysis. In the latter case, if the pore size of a matrix is large and the meshwork of fibers has enough elasticity, shape change in the cell body is sufficient to overcome the steric hindrance of the matrix. Based on our collagen pore size analysis in Chapter 2, we suspect that the pore size of the 0.3% collagen matrix is large enough for degradation-free EC migration.

To track the migration of ECs, cells were seeded at both high ($1x10^6$ cells/ml) and at low density ($5x10^4$ cells/ml). We performed time-lapse imaging on both

seeding densities to see if migration behavior significantly changed between these two conditions. At the high cell density, a 10x objective was used to obtain a large field of view. At low cell density, a 40x objective was used. At this low density, in the time course of a given experiment, at least 10, *xyz* positions were set on the microscope stage so that multiple cells could be analyzed during a single experiment. The stage

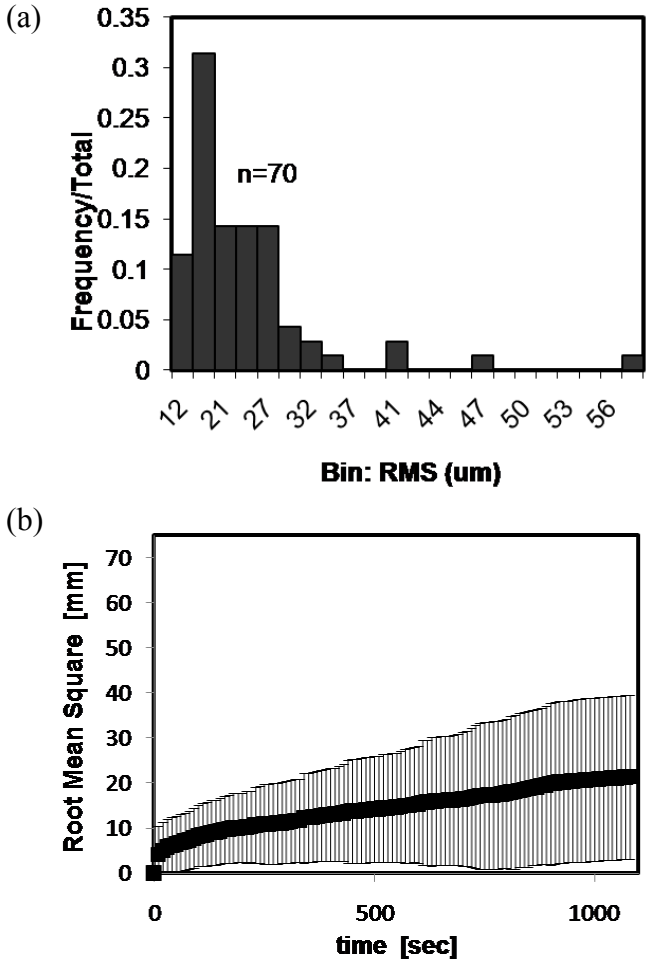

Figure 4-2. Migration behavior of endothelial cells in 3-D collagen matrices. (a) Tabulated frequencies the fraction of cells that exhibited the designated root mean squared displacement (RMS) over the course of 20 hours. n = 70. (b) The root mean squared displacement of a collection of isolated cells, n=24.

returned to those positions at every time point. A set of 3 images, spaced by 25 μm in the *z*, were collected at each position at each time point resulting in a *z*-stack (75 μm-deep) around the original center of every cell. Time course experiments were taken for at least 16 hours with manual re-focusing of the stage every 4-5 hours. At the conclusion of the 24 hour time lapse experiment, the plane at each time point that was in focus was used to generate a 2-D movie of cell movements over 24 hours.

The *xy* coordinates of the cell centers were identified using Image J software. We calculate the mean squared displacement of the cell nuclei for the high seeding density (Figure 4-2a), and we see minimal migration in the majority of cells. The cells that do migrate appear to be mobile from the beginning of our time-lapse experiments. Because in this study we investigate the early-time (< 24 hours) cell search, we assume significant levels of proteinases have not been secreted [11]. However, to test if protease-dependent migration is taking place, we added a global MMP inhibitor (GM6001) (data not shown) and there remains subset of cells that migrate a significant distance through the matrix, indicating a protease-independent migration strategy.

We also calculate the mean squared displacement of the cell nuclei for the high seeding density. Figure 4-2b shows the square root of the mean squared displacement for 24 cells. None of these cells migrated significantly (RMS over 20 hours is only ~ 30μm); however when cells are seeded at a low seeding density, there remains a subset of mobile cells.

The minimal migration seen here is not unexpected as the density of collagen fibers has a major effect on cell migration in collagen matrices. The proportion of cells that migration and the migration velocity has been shown to be reduced when fiber density is increased with an optimal collagen concentration of 1.5-2 mg/ml for migration[7]. Our 3 mg/ml collagen concentration may provide significantly more

steric hindrance and limit the migratory behavior of cells.

The most significant dynamic behavior seen during the live cell imaging is the extensive protrusive activity by the cells (Figure 4-3a) Based on the lack of migration and the prominence of protrusions, we hypothesize that protrusion activity is the primary search strategy used by our ECs in the collagen matrix. In the next section, I describe how we test this hypothesis and how we study the local cell-cell interactions by focusing on the behavior of cells that do not migrate significantly (Fig 4-2b). This strategy also helps us keep the cell in the field of view during live imaging.

4-4 Time-lapse microscopy for cell-cell interactions

Isolated cells and cell pairs with various initial separations were identified by scanning the collagen matrix with the microscope. Cells were seeded at low density ($5x10^4$ cells/ml) to avoid potential effects of local signaling by neighboring cells. Cells were selected only if they were at least 200 μm from a bottom boundary. As described above for the cell migration studies, in the time course of a given experiment, at least 10, *xyz* positions were set on the microscope stage so that multiple cells could be analyzed during a single experiment. The stage returned to those positions at every time point. A set of 3 images, spaced by 25 μm in the *z*, were collected at each position at each time point resulting in a *z*-stack (75 μm-deep) around the original center of every cell. Time course experiments were taken for at least 24 hours with manual re-focusing of the stage every 4-5 hours.

At the conclusion of the 24 hour time lapse experiment, the plane at each time point that was in focus was used to generate a 2-D movie of cell and matrix movements over 24 hours. The embedded microspheres (Fluoresbrite™ Carboxylate YG 1.0 micron Microspheres; Polyscience, Inc., Warrington, Pennsylvania), physisorbed to the collagen matrix, were used to observe deformation of the matrix.

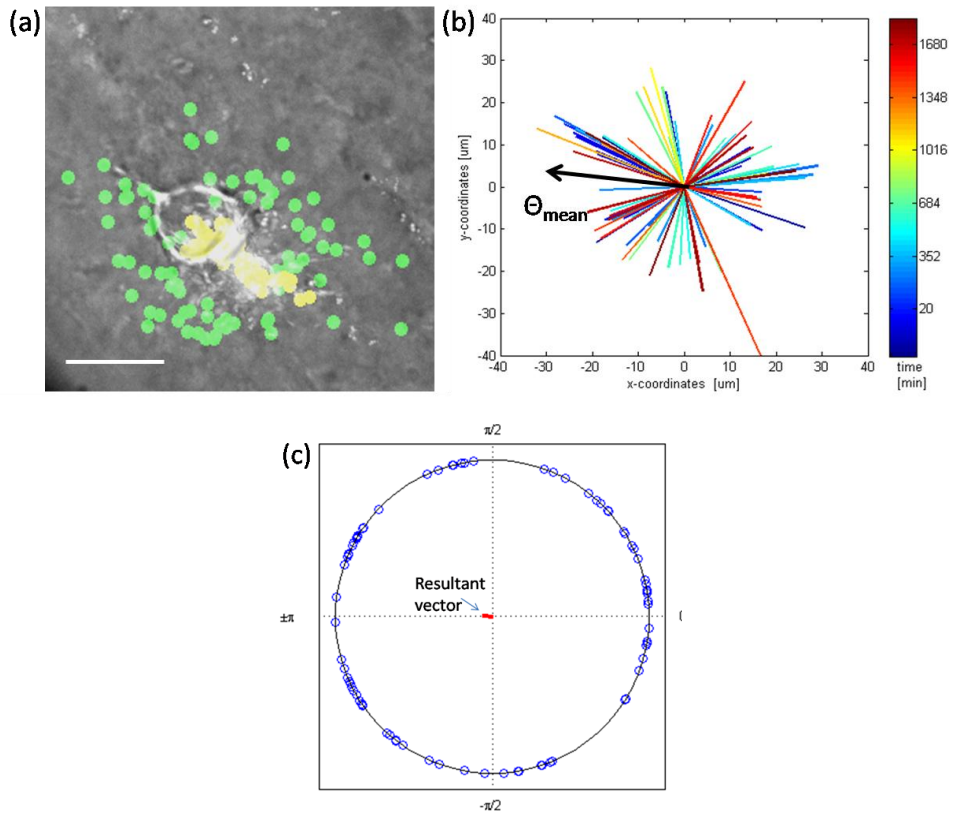

Figure 4-3. Protrusion dynamics analysis. (a) Bright field image formed by merging 72 frames captured at 10 minute intervals over 12 hours. Tracking was performed on protrusions at their maximum extension (green circles) and the cell center (yellow circles). Scale bar = 20 μm (b) Protrusion length and angle from the cell center in (a) with color-coded time information. The mean angle, Θ_{mean} defined by Equation is labeled. (c) The protrusions from (b) are plotted on a unit circle and the resultant direction and length is shown and labeled.

No deformation of the matrix was observed in association with the dynamics of protrusions. The *xy* coordinates of the cell centers and a reference microsphere (at least 200 μm from the cell of interest) were identified using Image J software (Figure4-3a).

4-5 Protrusion analysis

The protrusive behavior of endothelial cells in the 3-D collagen matrix is extremely dynamic and has been shown to be required for vascular network formation [12]. Therefore, in addition to just tracking cell centers and a reference bead, the *xy*

coordinates of the end of each protrusion at its maximum length were identified manually (Figure 4-3a). For instance, the *xy* coordinates of a protrusion that extended over the course of more than one time point only received one coordinate measurement. Using the *xy* coordinates of all of the above features (cell centers, reference beads, protrusions), a protrusion map was generated (Figure 4-3b) and the average protrusion frequency and length could be easily calculated. The mean angle and resultant vector were calculated based on a unit circle (Figure 4-3c) as described below.

We used circular statistics [13, 14] to find a mean resultant vector, $\bar{r}$, and its magnitude, *R*, and direction, Θ_{mean} (Figure 4-3b,c). We compute the mean direction of a collection of protrusions $\alpha = (\alpha_1, \ldots..\alpha_N)$ consisting of N protrusions, α_i . The directions are transformed to unit vectors by:

$$r_i = \begin{pmatrix} \cos\alpha_1 \\ \sin\alpha_1 \end{pmatrix} \quad [1]$$

$$\bar{r} = \frac{1}{N}\sum_i r_i \quad [2]$$

The mean angular direction, Θ_{mean} is calculated by transforming $\bar{r}$ using the four quadrant inverse tangent function[15].

4-6 Biochemical reagents to control cell behavior

Now that I have described our methods for visualizing and quantifying protrusive behavior, I will describe the reagents used to test cellular responses. All reagents were added to the assay media on top of the polymerized cell-seeded matrix at the concentrations listed in Table 4-1 immediately prior to the time course imaging. A monoclonal antibody against human VE-cadherin was added to prevent VE-cadherin mediated cell-cell specific interactions. The addition of VE-Cadherin (and not N-cadherin which was used as a control) to a monolayer of cells showed a

disruption of cell-cell contacts showing the utility of this molecule preventing cell-cell adhesion (Figure 4-4). Saturating amounts of recombinant human VEGF165 was used to eliminate any local gradients of VEGF that might be created by the cells[1]. The global matrix metalloproteinase (MMP) inhibitor, GM6001, was added to the system to inhibit any MMP-dependent matrix degradation. Finally soluble VEGFR-1 (sVEGF-R1) was used as a 'sink' for any bioavailable VEGF to eliminate or inhibit VEGF signaling[12].

Table 4-1. Experimental conditions used during live imaging to study cell-cell signaling mechanisms.

Condition	Description	Physical Parameter(s)	Communication mechanisms(s)
Pairs	Two cells	Separation between 0-130 μm	Cell-cell mechanical and chemical
Isolated	Single cell	isolated by > 200 μm	Autocrine
Anti-VE-cadherin	antibody against human VE-cadherin	10 μg/ml added to media	Cell-cell contact
Saturating VEGF	human recombinant VEGF 165	20nM added to media	VEGF signaling
sVEGF-R1	soluble VEGF-R1	15 ng/ml added to media	VEGF signaling
GM6001	MMP inhibitor	1 μM added to media	eliminating steric hindrance/integrins

4-7 Isolated cell and cell pair behaviors

In this section I describe how cells behave when they are by themselves or when they are near a single other cell. From our time-lapse experiments, we see that isolated cells (> 200 μm from another cell or boundary) use protrusive activity to search their local environment (Figure 4-5a). Performing a protrusion analysis as described in Figure 4-3 and section 4-4, the single cells send out protrusions with an average length of 20 μm at a frequency of ~ 4 protrusions/hr (Figure 4-6). By 3 hours, the cell begins to from a donut/lumen structure (Figure 4-5) which becomes stable by

24 hours. This isolated cell behavior is seen repeatedly, and we use this behavior as a control to compare to cell pair behaviors. To understand how cells interact with other cells, we imaged cell pairs at various initial cell-cell separations. In Fig 4-5b, c, and d, we show a cell pairs initially separated by ~ 79, 63, and 35 μm, respectively. In 4-5b, the cells behave indistinctly from isolated cells, i.e. they do not touch each other with protrusions and their protrusion length and frequency are not significantly different

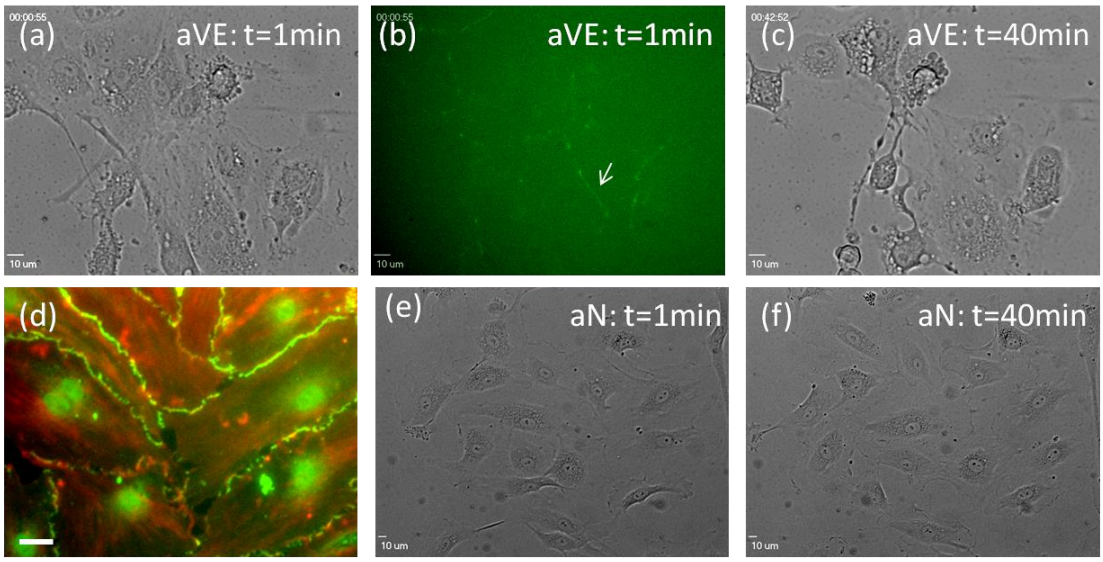

Figure 4-4. Addition of anti-VE-cadherin antibodies and anti-N-cadherin antibodies (10 μg/ml) to a monolayer of ECs on plastic. (a) ECs were plated on tissue culture plastic and allowed to attach for 24 hours. This brightfield image was taken ~ 1 minute after the addition of 10 μg/ml of anti-VE-cadherin antibodies (fluorescently labeled). (b) Here, the fluorescence signal of (a) is depicted and VE-cadherin junctions (arrow) can be seed between cells. (c) 40 minutes after the addition of anti-VE-cadherin, cell contacts are disturbed and cells detach from one another. (d) Upon removal of the anti-VE-cadherin, cells were fixed and stained with AlexaFluor Phalloidin 568 and fluorescently labeled anti-VE-cadherin. Scale bar = 20 μm (e) 1 minute after the addition of 10 μg/ml of anti-N-cadherin antibodies. (f) 40 minutes after the anti-N-cadherin treatment, cell-cell contacts remain.

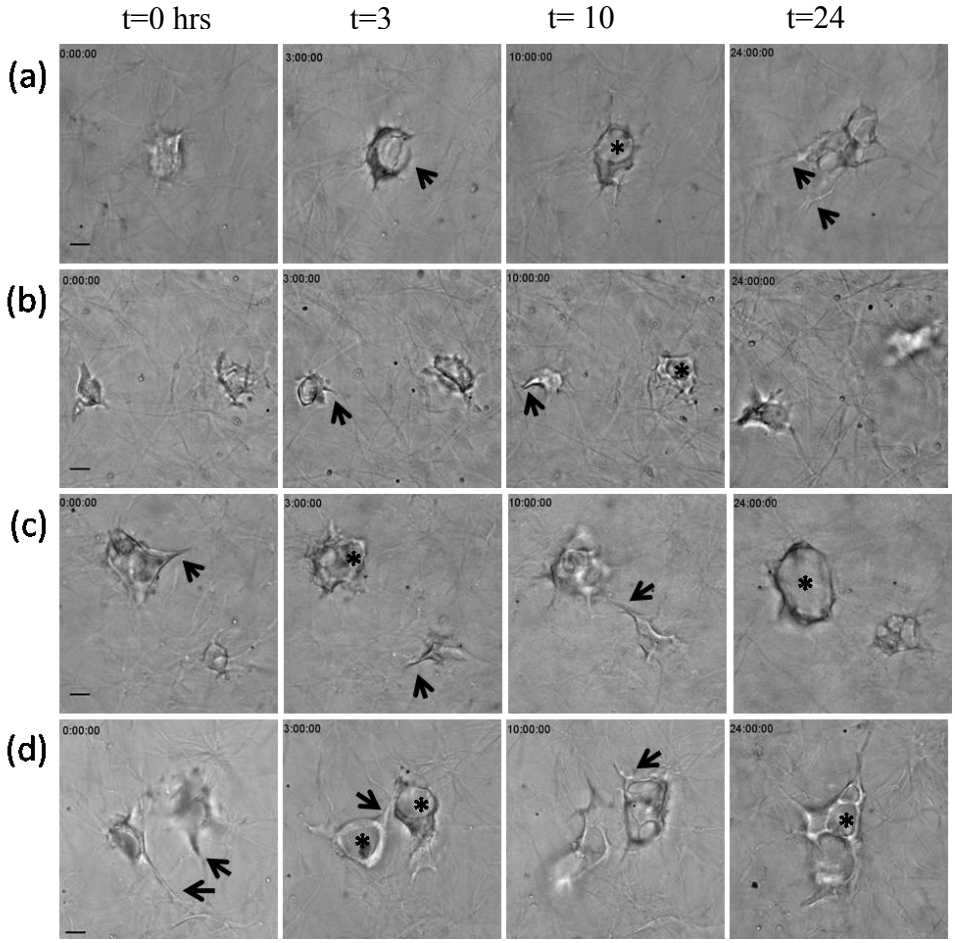

Figure 4-5. Time-lapse bright field images of a single plane of a 3D image stack of ECs in 3D collagen gels with no addition of biochemical reagents. (a) An isolated cell forms a single lumen after 24 hours. Arrows indicate protrusions and asterisks indicate open lumens. (b) A cell pair with an initial separation of 79 μm. The cells do not interact after 24 hours. (c) A cell pair with an initial separation of 63 μm. The cells touch and form stable, independent lumens after 24 hours. (d) A cell pair with an initial separation of 35 μm. The cells touch and connect to form a stable structure after 24 hours.

from isolated cells (Fig 4-6) In Figure 4-5c, the cells (initially ~ 63μm apart) touch each other repeatedly over the course of 24 hours; however, they end up forming separate independent lumen structures. We note that control cell pairs with a separation distance of between ~ 45-65 μm do not generally form a stable cell-cell connection (Figure 4-5c and 4-7a). The formation of a matrix-free path between the two cells and the cell's preference to crawl along a non-sterically hindered, two-

dimensional collagen surface could explain this observation. Note that two cells that touch but do not connect usually return near to their original location in the matrix after touching the other cell (Figure 4-5c).

In Figure 4-5d, the cells are very close (initially ~ 35μm apart) and the cells touch and connect to form a stable multicellular structure. Interestingly, the protrusion length of cells < 65 μm apart is significantly longer than isolated cells or pairs that are > 65 μm apart (Figure 4-6).

We plot cellular behaviors as a function of initial cell-cell separation in Figure 4-7. We define a *connection* to another cell if a protrusion is extended and does not get retracted. Note that when cells are connected and one cell moves, the other cell moves in the same direction. In addition, endpoint images with VE-cadherin staining shows VE-cadherin molecules present between connected cells (Figure 4-4d). We classify a pair of cells as having *no interactions* if there is no visible contact made.

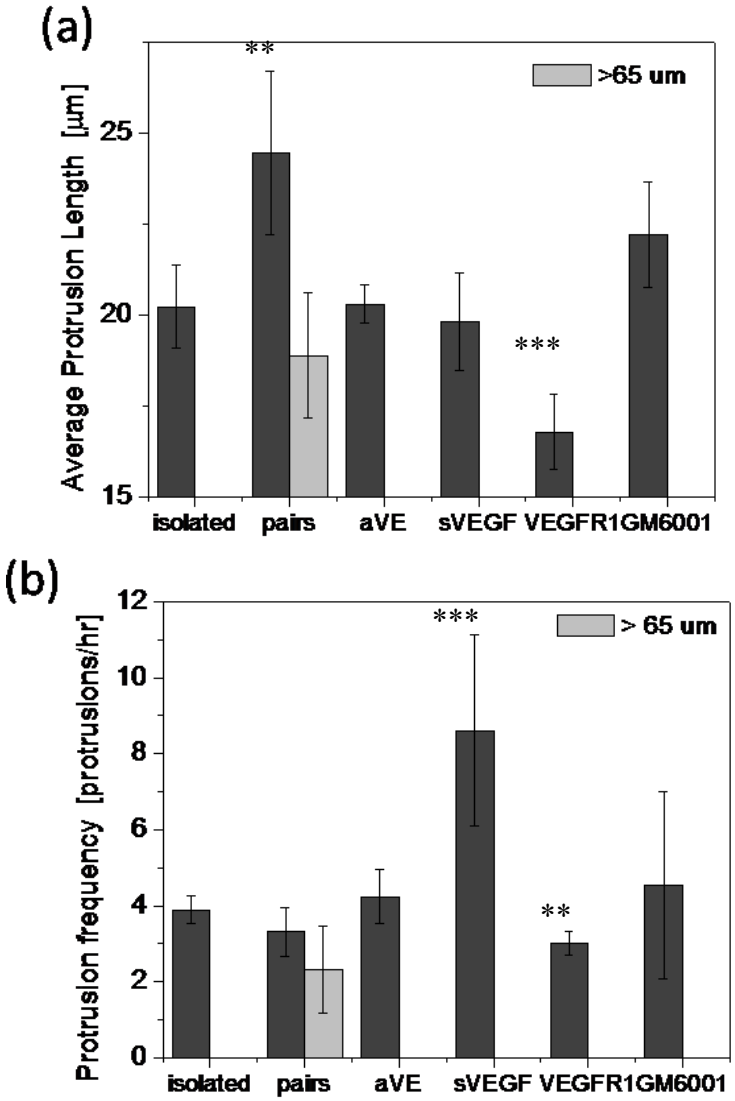

Figure 4-6. Protrusion frequency and length analysis for isolated cells, cell pairs, and various biochemical treatments. (a,b) VEGF signaling regulates protrusion length and frequency and some sort of cell-cell signaling (unidentified at this point) regulates protrusion length. *isolated* = single cell > 200 microns from another cell or boundary; *pairs* = two cells either <65 or > 65 μm (light gray bar) apart; *aVE* = cells treated with an anti-VE-cadherin antibody; *sVEGF*= cells treated with saturating amounts of VEGF in media; *VEGFR1*= cells treated with soluble VEGF receptor in media; *GM6001*= with MMP inhibitor in media. Error bars represent 99% confidence intervals. $p<0.01$ (**), $p<0.001$ (***). The number of cells and protrusion analyzed can be found in Tables 4-2 and 4-3.

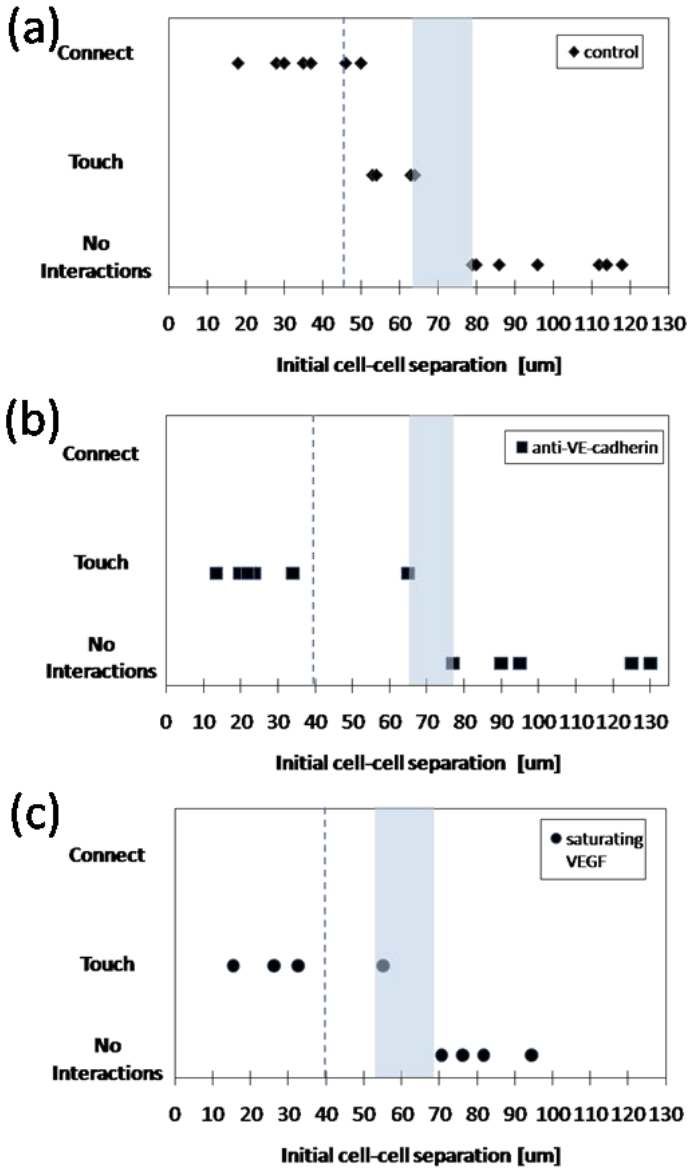

Figure 4-7. Cellular behaviors as a function of initial cell-cell separation. (a-c) Each point represents a pair of cells. The light blue bar highlights the critical region at which a cell begins to touch their neighboring cell. The vertical dashed line represents 2x the average protrusion length for cell-cell pairs (Figure 4-6). Conditions: (a) pairs of cells in control medium; (b) pairs of cells with addition of anti-VE-cadherin; (c) pairs of cells with the addition of saturating amounts of soluble VEGF.

Control pairs: The control case is when cells are cultured in the standard vasculogenesis media (Appendix A-3) and there are no additions of biochemical reagents. We see that cell behavior is a function of initial cell-cell separation (Figure

4-7). There is a critical cell-cell separation distance of ~ 60-70 μm (light blue bar) which is greater than 2x the average protrusion length (Figure 4-6). Note that we compare to 2x the protrusion length to give us a sense if the cells are communication via contact since two cells could simultaneously send out protrusions towards each other. For example, if each cell sent out a protrusion in the direction of the other cell simultaneously, on average, the protrusions would not touch the critical interaction distance of 60-70 μm since 2x the average protrusion length is 45 μm for the control case. This geometrical argument suggests that cell pairs may be communicating at a distance.

Anti-VE-Cadherin: To further test the notion of "action at a distance", we added anti-VE-cadherin to the culture media and monitored cell behavior and protrusion activity. We did not see a change in protrusion length or frequency as compared to isolated cells (Figure 4-6). When we plot the cell behavior as a function of initial cell-cell separation (Figure 4-7b), we show that cell pairs under the influence of anti-VE-cadherin do touch each other at a separation distance of ~ 60-70 μm, similar to the control cell pairs case. Twice the average protrusion length for anti-VE-cadherin cells of ~40 μm (Figure 4-6) is not statistically different than the control case, suggesting that VE-cadherin signaling and VE-cadherin specific contact is not a critical sensing mechanism for filopodial protrusions. In addition, in the behavior plot in Figure 4-7b, we can see that VE-cadherin (cell-specific contact) is necessary for a stable cell-cell connection to be made.

VEGF signaling: To over stimulate VEGF/VEGF receptor signaling and to potentially eliminate local gradients of VEGF, a saturating amount (20nM)[1] of human recombinant VEGF165 was added to the media. The excess VEGF led to an increase in endothelial cell protrusive activity (Figure 4-6) just as it does *in vivo* [12]. Also, as expected, the addition of the soluble VEGF receptor (which depleted the level

of bioavailable VEGF) decreased both protrusion length and frequency (4-6) [12]. Interestingly, while the critical length scale of interaction remained unchanged as compared to the control case, excess VEGF inhibited stable cell-cell connections (Figure 4-7c). This observation is not unexpected as VEGF is known to cause the internalization of VE-cadherin molecules [16].

MMP activity: We also show that protrusion length and frequency remain unchanged as compared to control conditions with the addition GM6001(Figure 4-6) which indicates that cells do not need to degrade their matrix for protrusion activity because GM6001 is a potent inhibitor of collagenase/MMP production [17]. The protrusions are similar in diameter as the collagen matrix pore size; thus, the protrusions could be sent out between collagen fibers or along the fibers without significant steric hindrance.

Based upon the analyses of cellular protrusion dynamics of isolated cell, cell pairs, and cells undergoing various biochemical treatments, we have shown the presence of another cell and VEGF signaling regulate protrusive activity and that VE-cadherin and MMP-activity do not.

4-8 Protrusion Clustering

The above results indicate that cellular protrusions are being used as a sensing mechanism. Because the 2x protrusion lengths are less than the cell-cell separation at which cells begin to touch each other, we believe there is action at a distance between cells. In this section, we describe our work quantifying the directionality of protrusions to see if protrusions show a bias in the direction of another cell. Again, we add our biochemical reagents to alter the system as a means to begin to sort out what signals protrusions may be sensing.

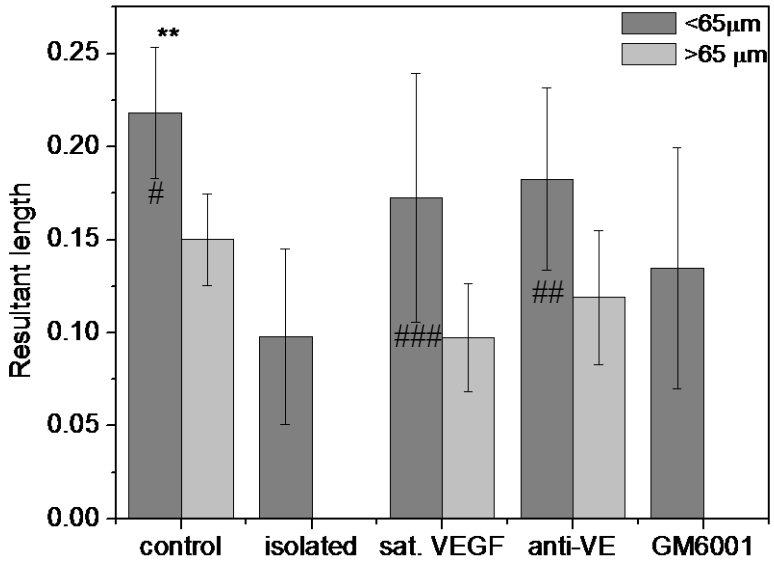

Figure 4-8. Resultant length. The resultant lengths were calculated from protrusion directions using a unit circle as described in Figure 4-3. The light bars (>65) indicate when a cell is > 65 μm from another cell. Dark bars (<65) indicate when a cell is < 65 μm from another cell. In the isolated condition, there can be no separation dependence, so the dark bar represents all isolated cells. We did not obtain data for > 65 μm in the GM6001 case. Data represent the average resultant length from at least 8 different cells. Error bars represent the 99% confidence intervals. Asterisks represent significant differences in resultant length compared to isolated cells. $p<0.001$ (***); $p<0.01$ (**); $p<0.05$ (*). See Table 4-2 and 4-3 for sample numbers. The V-test was used to determine if cell protrusions showed a bias in the direction of another cell $p<0.001$ (###); $p<0.01$ (##); $p<0.05$ (#) are shown.

clustering, we calculate the resultant length, R, which is the magnitude of the mean resultant vector:

$$R = \left| \overline{r} \right| \qquad [3]$$

This length is an indication of the relative dispersion or concentration of the protrusion directions. The resultant length approaches 1 under strong directedness but approaches 0 under circular uniformity.

Using Eq. [3], we calculated the magnitude of the resultant vector (resultant length). Similar to the protrusion length and frequency analysis, we separated our resultant length analysis based on cells pairs that were separated by the critical length scales of 65 μm for two cells to determine if there was any separation dependence on

protrusion clustering (Figure 4-8). When a cell is < 65 μm away from another cell there is significant protrusion clustering as compared to isolated cells. In contrast the protrusions of cell pairs in the presence of saturating amounts of VEGF, anti-VE-cadherin, or GM6001 (Figure 4-8) are not significantly more clustered than those for an isolated cell. These results suggest that cells could be sensing a soluble signal or a mechanical signal that is being transmitted through the collagen matrix from another cell that is < 65 μm away.

Note that the saturating VEGF condition would eliminate any local VEGF gradients around the cell, so because this condition does not elicit protrusion clustering, there may be other soluble factors (other than VEGF) that are being used as signaling molecules. Because the resultant length is a measure of the concentration of a circular data set and gives no information regarding a specific direction of the data set, in the next section, we turn to a circular statistical analysis to determine of the clustering is in the direction of the neighboring cell.

4-9 Protrusion directionality

We analyzed the specific directions of protrusions using the circular statistical V-test with the circular statistics toolbox for Matlab. The V-test allows one to test if the sample is oriented in a particular direction. We used the V-test to determine whether the protrusions were significantly clustered towards another cell or boundary. We specify a predicted direction, ϕ_A (direction of the neighboring cell or the boundary), and compute the test statistic, V_0, as follows:

$$V_0 = \sum_{i=1}^{n} \cos(\theta_i - \phi_A) = R\cos(\theta_{mean} - \phi_A) \quad [4]$$

V_0 represents the length of the projection of the resultant vector towards the predicted direction ϕ_A and is always less than or equal to than the resultant length, R. The ratio V_0/R represents how close the mean direction is to the predicted direction. V_0 ranges between -1 and +1. If the observed protrusion angles do not deviate much from the

predicted angle, V_0 approaches 1 and the protrusions are clustering around the predicted direction. Approximate critical values for the quantity:

$$\sqrt{2}/\sqrt{N} * V_0 \qquad [5]$$

can be obtained from the one tailed normal deviate $Z_{\alpha(1)}$. Using Table B.35 from [14], which lists the critical values of Eq. (9), given an N, V_0, and chosen significant level value), we can find the probability that the direction is random with respect to the predicted direction, ϕ_A. If that probability is > 95% (one minus that probability is < 0.05) the protrusions are considered significantly directed towards the predicted direction (Tables 4-2 and 4-3).

Table 4-2. Directionality of protrusions for cells < 65 μm from another cell.

Condition	nprotrusions	ncells	ncells ###p < 0.001	ncells## p < 0.01	ncells# p < 0.05	% sig. directed
control	331	12	4	3	4	91.7
anti-VE	749	14	8	3	--	78.6
Sat VEGF	690	6	5	--	--	83.3
isolated cells	313	6	2 (ϕ set to 0)	--	--	33.3

Table 4-3. Directionality of protrusions for cells > 65 μm from another cell.

Condition	nprotrusions	ncells	ncells ### p < 0.001	ncells## p < 0.01	ncells # p < 0.05	% sig. directed
control	217	6	1	1	--	33.3
anti-VE	299	6	--	--	--	0.0
saturating VEGF	860	8	1	1	--	25.0
isolated cells	313	6	2 (ϕ set to 0)	--	--	33.3

Again, cell pairs were separated into those which had initial separations of <65 from another cell (Table 4-2) and those which had an initial separation of >65 μm for another cell (Table 4-3). The protrusions of 32 cells that were near another cell were analyzed equaling a total of 1770 protrusions. Each of the cells' protrusions underwent the V-test. To apply this test, we set the predicted average direction of protrusions, ϕ_A, equal to the mean angle to the neighboring cell. For example, we determined the mean angle to the neighbor, $\Theta_{neighbor}$ by calculating the average vector

direction from the cell center to the shortest distance to the neighbor at each time point during the 24 hour time lapse experiment (just as when we calculated the mean angle of protrusions, $\Theta_{mean,}$ using Eqs. [1] and [2])

By applying the V-test, we determined if the protrusions were significantly directed towards another cell and if the directedness was dependent on initial separation. For the pairs <65μm from another cell under control conditions, 11 out of the 12 control cells analyzed, (or 91.7%) had their protrusions significantly ($p<0.05$, $p<0.01$, or $p<0.001$) directed towards the other cell (# in Figure 4-8 and Table 4-2). Similarly, (in the <65μm case) cell pairs in the presence of anti-VE-cadherin or saturating amounts of VEGF showed the majority (11/14 and 5/6, respectfully) (## and ### in 4-8 and Table 4-2) of cells' protrusion directed in the predicted direction. All of these statistics included cells from before and after the first contact was made. Making this distinction did not change the results; however, in almost all <65μm cases, a protrusion made contact with the other cell or boundary before enough time elapsed to track enough protrusions to perform a rigorous statistical analysis. The addition of the anti-VE-cadherin did not significantly change cell behavior or protrusion bias (### in 4-8) indicating that cell-specific touch is not directing cell-cell communication. Isolated cells (>200 μm from another cell or boundary) were significantly biased in direction (predicted direction just set to 0) in 2/6 (or 33.3%) instances. Isolated cells should have no signal to bias their search, so this data represents a purely random protrusive search.

The protrusions of a total of 20 cells that were > 65 from another cell were analyzed with a total of 1376 protrusions (Table 4-3). After analysis with the V-test as described above, only 2/6 of the control pairs, 0/6 of the anti-VE-cadherin treatment cells, and 2/8 of the saturating VEGF cells showed significant bias in the predicted direction (Table 4-3).

4-11 Conclusions:

In this chapter we describe our use of live time-lapse microcopy to visualize cell behavior during the first 24 hours of culture within a 3-D collagen matrix. We used a low seeding density, and we tracked the movement and behavior of isolated cells and cells that were at various initial separations from another single cell. In Chapter 3, we showed that a connected cell network forms at a critical initial cell-seeding density that corresponds to a cell-cell separation (center to center) of ~ 79μm, which suggests a distance over which cells can interact. However, just based upon the endpoint collective cell behavior data presented in Chapter 3, we cannot conclude if cells are interacting by migration, stretching, or if they have an effective radius of action that is larger than their maximally stretched form. In addition it is not clear if the interactions (whether it is migration, stretching, or some longer-range interaction) are random or directed in some manner. In this chapter, I have presented our work that has focused on studying the cell strategies used to locate other cells and our efforts to determine if cell pairs interact at a distance.

Using live imaging and tracking of cell centers, we showed that the majority of cells do not migrate significantly through the surrounding collagen matrix (Figure 4-2). Even though the cells experienced significant displacement, they were dynamic during the first 24 hours of culture. The most striking cell behavior demonstrated in the 3-D matrix was the dynamic cellular protrusion activity of cells. The endothelial cells sent out numerous filopodial extensions through and along the collagen matrix (Figure 4-1b). These needle-like protrusions were typically extended and retracted very quickly and have been widely suggested to be sensory structures, allowing a cell to explore its environment, searching for guidance cues, other cells, or suitable sites for attachment [18, 19].

The motion of isolated cells and cell pairs as well as the dynamics and

directionality of protrusions of isolated cells and cell pairs were studied extensively. We showed that cell pairs will touch and connect if they are less than 65 μm apart (center to center). Cell pairs at greater than 65 μm apart did not touch each other and, hence, did not connect. This length scale of touch and connect was similar to our collective cell length scale of interaction from Chapter 3 of 79 μm. By comparing the protrusion dynamics and directionality of isolated cells versus cell pairs, we showed that the cells are using protrusions as a sensing structure.

Our protrusion analysis in the presence of saturating amounts of VEGF and soluble VEGF receptor-1 confirm past *in vivo* results that VEGF signaling regulates protrusion dynamics in endothelial cells. Further research regarding the addition of these molecules would be valuable to understand the VEGF signaling in our system. For example, we add a "saturating" amount of exogenous VEGF. The concentration that is "saturating" in our system was estimated based on literature values. It would be informative to perform a dose response experiment to determine the critical and saturating VEGF concentrations. Also, the levels of exogenous VEGF may or may not have minimized significant concentration gradients present between cell pairs. Furthermore, the addition of the soluble VEGF receptor-1 provides a simple "loss-of-function" assay; however, the extent to which the soluble receptor interacts with the cell membrane and potentially changes VEGF signaling has not be explored in our system.

The addition of a global MMP inhibitor, GM6001, was a first step to understanding the importance of collagen degradation during cell protrusions and cell-cell communication in 3-D collagen. Our initial findings indicated that MMP-dependent collagen degradation was not required for protrusion activity in the first 24 hours of the cell-cell search. Further research using more reliable inhibitors (such as siRNA) would be useful to confirm our initial results and to potentially determine

which MMPs and/or TIMPs are important for endothelial cell-cell communication in 3-D collagen matrices.

With the addition of anti-VE-cadherin antibodies, we saw that cell-specific contact was likely not the primary sensing mechanism used to locate other cells; however, other cell-specific contact signals could be present and be responsible for the bias in protrusions seen for cell pairs that were separated by less than 65 μm. Note that the critical cell-cell separation of less than 65 μm was similar to that of twice the maximum protrusion length of a cell. Therefore, it remains unclear if indeed cell contact is the instigating signal that creates protrusion bias during cell-cell communication.

Our findings suggest that cell protrusions are used as a sensing structure. Our results are compatible with cell-cell interaction at a distance; however, we have not performed the necessary experiments to conclude that cells do not use contact as their primary sensing mechanism. In order to clarify the issue of contact versus action at a distance, a more complete protrusion analysis needs to be performed. The time-lapse experiments need to be set up such that protrusion dwell time can be calculated; therefore, imaging the cells at time intervals of varying duration (from 1 minute to 10 minutes) should be performed. In addition, the exact moment a protrusion touches a neighboring cells must be recorded and protrusion bias analysis must be separated into a "before touch" regime and an "after touch" regime.

With our current imaging methods (three *z*-planes with brightfield microscopy), the definition of "touch" and the exact 3-D protrusion direction are not well-defined or easily determined. For instance, we do not have a full 3-D visualization of the cellular dynamics, and it is not clear if a cell protrusion has actually touched or made contact with another cell. These challenges could be met by using live confocal fluorescence imaging and fluorescent expressing VE-cadherin

endothelial cells.

In order to investigate the possibility of cell-cell interaction at a distance, in the next chapter, I describe our work which focuses on the investigation of two mechanisms that could be acting from a distance: mechanical and chemical gradients. In the following chapter, we again analyze cell behavior and protrusion dynamics; however, we visualize cells near boundaries of different physical properties and study cell behavior and protrusion directionality as a function of boundary type. As it will become clear in the next chapter, we show that boundary conditions can be used as a non-specific assay for decoupling chemical and mechanical signaling in 3-D.

REFERENCES

1. Serini, G., et al., *Modeling the early stages of vascular network assembly.* Embo J, 2003. **22**(8): p. 1771-9.

2. Reinhart-King, C.A., M. Dembo, and D.A. Hammer, *Cell-cell mechanical communication through compliant substrates.* Biophysical Journal, 2008. **95**(12): p. 6044-51.

3. Bach, T.L., et al., *VE-Cadherin mediates endothelial cell capillary tube formation in fibrin and collagen gels.* Exp Cell Res, 1998. **238**(2): p. 324-34.

4. Porter, R.A., et al., *Ultrastructural changes during contraction of collagen lattices by ocular fibroblasts.* Wound Repair Regen, 1998. **6**(2): p. 157-66.

5. Sheu, M.T., et al., *Characterization of collagen gel solutions and collagen matrices for cell culture.* Biomaterials, 2001. **22**(13): p. 1713-9.

6. Bloom, R.J., et al., *Mapping local matrix remodeling induced by a migrating tumor cell using three-dimensional multiple-particle tracking.* Biophys J, 2008. **95**(8): p. 4077-88.

7. Schor, S.L., et al., *The use of three-dimensional collagen gels for the study of tumour cell invasion in vitro: experimental parameters influencing cell migration into the gel matrix.* Int J Cancer, 1982. **29**(1): p. 57-62.

8. Pedersen, J.A. and M.A. Swartz, *Mechanobiology in the third dimension.* Ann Biomed Eng, 2005. **33**(11): p. 1469-90.

9. Coffin, J.D. and T.J. Poole, *Endothelial cell origin and migration in embryonic heart and cranial blood vessel development.* Anat Rec, 1991. **231**(3): p. 383-95.

10. Friedl, P. and E.B. Brocker, *The biology of cell locomotion within three-dimensional extracellular matrix.* Cell Mol Life Sci, 2000. **57**(1): p. 41-64.

11. Davis, G.E., et al., *Matrix metalloproteinase-1 and -9 activation by plasmin*

regulates a novel endothelial cell-mediated mechanism of collagen gel contraction and capillary tube regression in three-dimensional collagen matrices. Journal of Cell Science, 2001. **114**(5): p. 917-930.

12. Drake, C.J., et al., *VEGF regulates cell behavior during vasculogenesis.* Dev Biol, 2000. **224**(2): p. 178-88.

13. Mardia, K.V., *Directional Statistics*. Wiley Series in Probability and Statistics. 2000, New York: John Wiley & Sons, LTD.

14. Zar, J.H., *Biostatistical analysis*. 4th ed. 1999: Prentice Hill.

15. Berens, *Technical Report No. 184 The circular statistics toolbox for Matlab.* Max Planck Institute for Biological Cybernetics, 2009.

16. Gavard, J. and J.S. Gutkind, *VEGF controls endothelial-cell permeability by promoting the beta-arrestin-dependent endocytosis of VE-cadherin.* Nat Cell Biol, 2006. **8**(11): p. 1223-34.

17. Galardy, R.E., et al., *Inhibition of angiogenesis by the matrix metalloprotease inhibitor N-[2R-2-(hydroxamidocarbonymethyl)-4-methylpentanoyl)]-L-tryptophan methylamide.* Cancer Res, 1994. **54**(17): p. 4715-8.

18. Zheng, J.Q., J.J. Wan, and M.M. Poo, *Essential role of filopodia in chemotropic turning of nerve growth cone induced by a glutamate gradient.* J Neurosci, 1996. **16**(3): p. 1140-9.

19. Gerhardt, H., et al., *VEGF guides angiogenic sprouting utilizing endothelial tip cell filopodia.* J Cell Biol, 2003. **161**(6): p. 1163-77.

CHAPTER 5

BOUNDARY CONDITIONS TO SEPARATE MECHANICS AND MASS TRANSFER-MEDIATED CELL SIGNALING

5-1 Introduction

In vitro vascular network formation is an interesting example of self-organization during development. In the previous chapters, we have described the dynamic self-assembly of endothelial cells from a random initial 3-D spatial distribution of individual cells into an organized, open network of tubes. Endothelial cells are initially isotropically seeded throughout a 3-D matrix and immediately employ a dynamic search to locate and interact with other cells. A significant challenge to understanding this process of cellular self-organization is determining the mechanisms by which the initial isotropic state of the system (endothelial cells dispersed in a 3-D collagen matrix) is broken and how an organized, anisotropic state (the vascular network) emerges. In chapter 3, we described our investigation of collective cell behavior as the system advances from unorganized to organized, and in chapter 4, we looked at local cell behavior as the system begins to break isotropy, but we (and others) still have yet to determine the signaling mechanisms responsible for these cell-cell interactions.

Chemical gradients [1-3], mechanical interactions [4-6], and cell-cell contact [7-9] have been implicated in vascular network formation (Figure 5-1), but the distinct roles of these stimuli remain difficult to isolate. Most methods of modifying the modulus of a matrix change both its chemical and mechanical properties, and the complicated nature of the transfer of mass and stress through 3-D matrices makes understanding and distinguishing the mechanical and biochemical signals that dictate cell behavior in 3-D is a significant challenge.

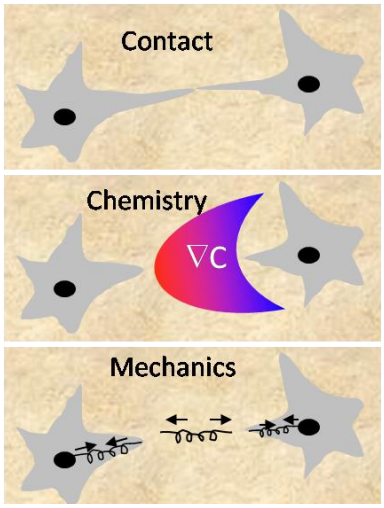

Figure 5-1. Cell-cell contact, chemical gradients, and mechanical interactions have all been implicated as possible mechanisms of cell-cell communication during vascular network formation. The similar characteristics of mass and stress transfer within a 3-D matrix make decoupling these mechanisms difficult.

In this chapter we describe how we have developed and exploited an experimental assay to study how mechanics and chemistry independently influence endothelial cell-cell communication in 3-D. Here, we describe this assay which uses boundary conditions (BCs) to decouple mechanical from mass transfer-based mechanisms of local cell-cell communication. More specifically, we analyze cell behavior and protrusion activity within a 3-D collagen matrix that is firmly attached to vertical boundaries that have variable mechanical and mass transport properties. The effective mechanics of the matrix or the effective mass transport (non-specific to a certain soluble factor) around a cell can be tuned based on the cell's distance from various types of boundaries.

5-2 Boundary conditions and FEM modeling

In this section, I describe the various boundary conditions we used and how they are able change the local mechanics and chemical environment around a cell. Briefly, we fabricated wells in the following three different materials: 1) PDMS wells were used as a stiff and impermeable boundary, 2) 2% collagen wells were used as a

stiff and diffusively permeable boundary, and 3) a 4% alginate/0.3% collagen mixture was used as a second example of a stiff and diffusively permeable boundary. The experimental setup (Figure 5-2) and protrusion analysis we used was similar to that described in Chapter 4; however, here, instead of imaging isolated cells and cells that are near other cells, we focus on cells that are various initial distances from the vertical boundary, composed of different materials (Table 5-1). In Figure 5-2, we can see a schematic diagram of the assay used for these boundary condition (BC) experiments. As described in Chapter 4, human umbilical vein endothelial cells (HUVECs) were seeded at a low seeding density of ~ $5x10^4$ cells/ml into 0.3% type I collagen. The wells in which the cell-seeded collagen was polymerized was either made out of poly-(dimethylsiloxane) (PDMS), 2.0% type I collagen, or a composite hydrogel of 4.0% alginate-0.3% collagen. Below, for each well type, I describe the physical properties, effects on chemistry and mechanics around a cell, and fabrication process.

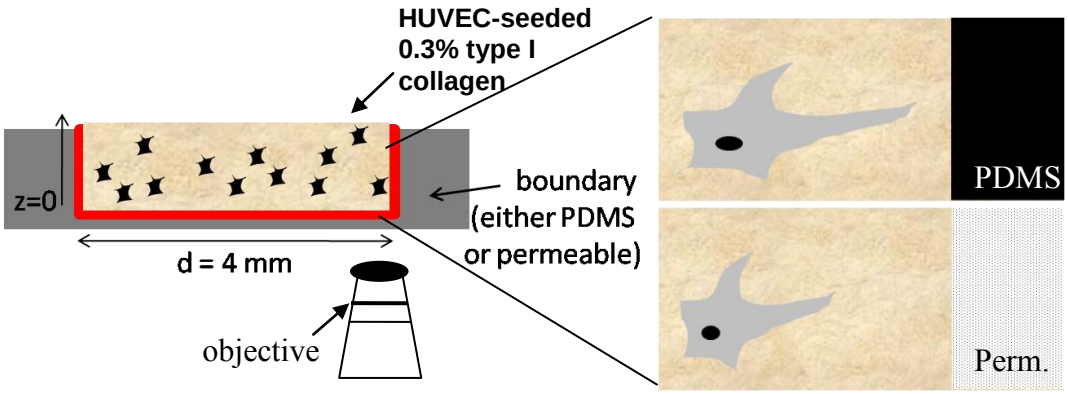

Figure 5-2. Schematic diagram of boundary condition assay. HUVECs were seeded at $5x10^4$cells/ml into 0.3% collagen. The well was made out of either PDMS or a permeable material (2% collagen or 4% algninate/0.3% collagen mixture). See Section 5-3 for fabrication methods. Individual cells near the boundaries were live imaged with an inverted brightfield microscope.

Table 5-1. Experimental conditions used during live imaging to study cell-cell signaling mechanisms.

Condition	Description	Physical Characteristic(s)	Communication mechanisms(s)
PDMS Bound.	Single cell near a PDMS boundary	Impermeable; modulus ~ >350 kPa [10]	Mechanics and/or chemistry
2% Col. Bound.	Single cell near a 2% collagen boundary	Permeable; modulus ~ 1.7 kPa	Mechanics and/or chemistry
Alg/Col Bound.	Single cell near a 4% alginate/0.3% collagen mixture boundary	Permeable; modulus ~ 28 kPa	Mechanics and/or chemistry

We used PDMS as a stiff, impermeable well boundary since PDMS is impermeable to macromolecules, and its modulus is high (~ 350 kPa)[10]. A source of either a soluble macromolecule (for example, VEGF) or a stress field (from cellular traction forces) in close proximity to the PDMS boundary would create an anisotropic chemical or mechanical local environment, respectively. We perform finite element method (FEM) calculations to model the concentration fields and stress and displacement fields around a "source" (a cell) near an impermeable boundary (Figure 5-3b iii. and Figure 5-4). For the concentration calculations in (Figure 5-3b, Figure 5-4a), no flux conditions were maintained on edge boundaries expect on the permeable boundary, and for the mechanics calculations in (Figure 5-3c, Figure 5-4b), zero displacement boundary conditions were maintained on the edge boundaries. Distributions are shown for steady state in both.

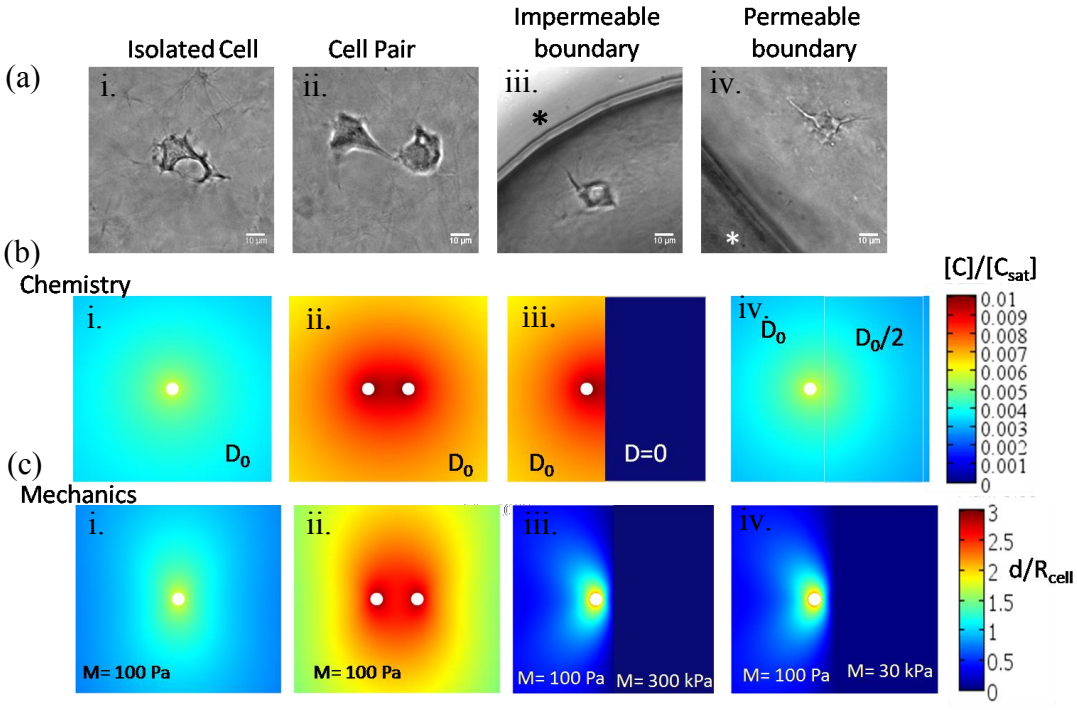

Figure 5-3. Numerical calculations for mass transfer and mechanics (both steady state) within the 0.3% collagen gel with various boundary conditions studied experimentally in this chapter. (a. i-iv) Brightfield images of endothelial cells under the labeled conditions. Black asterisk in (a.iii.) indicates PDMS boundary. White asterisk in (a.iv.) indicates 2% collagen boundary. Scale bar = 10 μm. (b) Mass transfer calculations for (i) An isolated cell, (ii) a cell pair separated by 65 μm, (iii) a cell 32 μm from a solid, impermeable wall, (iv.) a cell 32 μm from a solid, permeable wall. D_o = free diffusivity. The permeable wall in (b.iv.) has a diffusivity of ½ D_o. The scale is nondimensionalized by the saturation concentration, C_{sat}. (c) Mechanics calculations for the same geometrical conditions as in (b, i-iv.). Moduli values for the materials are labeled in the figure. Scale is nondimensionalized by the radius of the cell (10 μm)

As one can see from the distributions plotted in Figure 5-4, an impermeable boundary creates a higher concentration of soluble factor near the cell (similar to a cell pair) as compared to an isolated cell or cell near a permeable boundary. In contrast, the displacement fields around a cell near any of the boundaries (permeable or impermeable) are essentially identical (Figure 5-4b). Based on these calculations, we hypothesize that if chemical gradients or mechanical gradients are playing a role in cellular protrusion

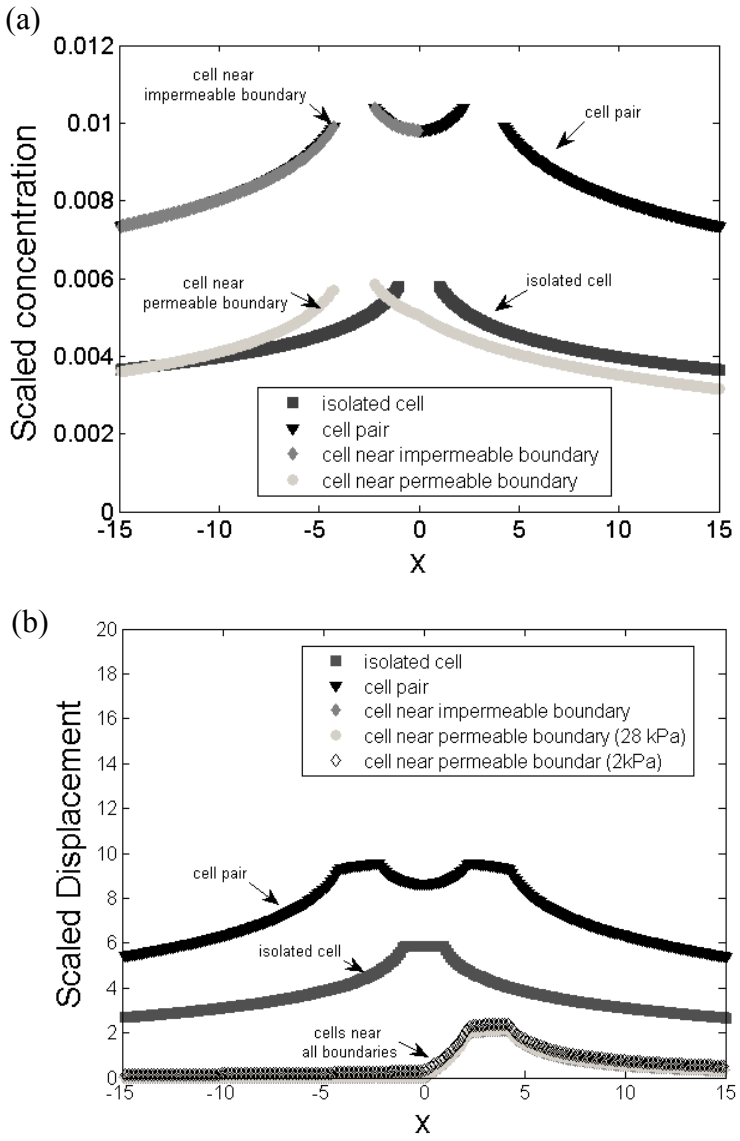

Figure 5-4. FEM modeling concentrations (a) and displacements (b) from Figure 5-3. (a) A cell near an impermeable boundary shows a nearly identical concentration profile as a cell pair. The concentration of a soluble chemical diffuses away from an isolated cell or cell near permeable boundary, decreasing the concentration around a cell. (b) The displacement field around a cells near any of the boundaries are very similar. The traction forces of the cell are small compared to the stiffness of all three boundaries.

activity, the non-uniform chemical and mechanical profiles that are established when near a PDMS boundary could influence the protrusion direction to be biased towards the boundary. There are qualitative similarities between the characteristics of mass and stress transfer, so simply studying protrusion bias near a PDMS boundary would not be sufficient to decouple chemistry and mechanics. Therefore, we create boundaries that are permeable to macromolecules but which remain mechanically stiff.

We prepared permeable, stiff boundaries using 2% collagen and also using a mixture of 4% alginate and 0.3% collagen (Table 5-2). Our dense 2% collagen has been characterized in Chapter 2. It has a modulus of ~ 1.7kPa and is diffusively permeable to macromolecules (data not shown for diffusivity). Because endothelial cells have been shown to exert traction forces of around 1 kPa [4], we also created a significantly stiffer permeable boundary (~ 28 kPa, Table 5-2) out of a mixture of 4% alginate and 0.3% type I collagen. The modulus of this composite material was tested using confined compression testing as described in detail in Chapter 2. Similar to the impermeable PDMS boundary, a source (a cell) of a stress field in close proximity to the permeable boundary would create an anisotropic mechanical local environment (Figure 5-4b); however, for a source of a soluble signal near a permeable boundary, the chemical environment would remain essentially isotropic (Figure 5-3b, c iv and Figure 5-4a) because the soluble molecule could just diffuse away. Based on these finite element calculations, we hypothesize that if mechanical gradients are playing a role cell signaling, protrusion dynamics and direction will be not be different in the impermeable and permeable cases. In contrast, if soluble gradients are dictating protrusion dynamics and/or directionality, the PDMS and permeable boundary conditions will create different cellular behaviors.

5-3 Fabrication of boundary conditions

PDMS (Figure 5-3(a, iii): Soft lithography was used to generate a PDMS stamp with 4mm- diameter wells. A layer of SU8-2100 series (Microchem Corp.) was spun, exposed, and developed to generate an array of 4-mm diameter pillars. (poly)-dimethylsiloxane (PDMS) (Sylgard® 184, Dow Corning, Midland, Michigan) was molded over the SU8 master by pouring the pre-polymer solution and curing for 3 hours at 65 °C. PDMS was poured over the pillars so there was flat layer of PDMS over the pillars (no "through holes"). A 6-mm diameter biopsy punch was used to separate the PDMS wells into individual wells that were then placed in the bottom of a 48-well plate. Before use, the PDMS wells were cleaned and treated to covalently bind the collagen to the well boundaries as described in Chapter 3 and Appendix A-6. Cell seeded collagen solutions were allowed to polymerize in the PDMS wells at 37° C and 5% $C0_2$ for 20 minutes. The entire PDMS well was placed in a 48-well plate, and 300 μl of vasculogenesis media (described in Appendix A-3) was added to each.

2% collagen (Figure 5-3(a, iv.): To prepare wells in 2% collagen, lyophilized collagen (as described above) was resuspended in 0.1% acetic acid to a concentration of 30 mg/ml. Resuspension of this high mass fraction stock solution took up to 5 days. The gels were prepared from that concentrated stock solution by adding 1N NaOH, 10x M199, 1xM199 to a final concentration of 20 mg/ml (2%) (as described in Appendix A-5) and mixing on ice. Microspheres (Fluoresbrite™ Carboxylate YG 1.0 micron Microspheres; Polyscience, Inc., Warrington, Pennsylvania) were added to the collagen solution at a concentration of $3x10^7$ beads/ml. Neutralized collagen solution was injected around a PDMS mold in order to generate a 4mm-diameter well in the 2% collagen. A PDMS cover was placed in top of each cylindrical mold in order to make the bottom of the well flat and define a thickness of ~ 0.5mm. Collagen was allowed to polymerize at 37 °C in 5% CO_2 for 30 minutes. Once the collagen was

polymerized, the PDMS cover was removed, and each well was incubated with growth media at 37 °C for at least 3 hours before use. Cell-seeded collagen solutions of 0.3% were allowed to polymerize in the 2% collagen wells at 37° C and 5% $C0_2$ for 20 minutes. The entire well was placed in a 48-well plate, and 300 μl of vasculogenesis media (described in Appendix A-3) was added to each.

4% alginate/0.3% collagen: Wells formed of 4% alginate/0.3% collagen were prepared because the incorporation of 4% alginate significantly increased the stiffness of the permeable boundary, and the 0.3% collagen was included so that the cell-seeded collagen matrix would adhere to the boundary[11]. To prepare 4% alginate/0.3% collagen boundary conditions, an 8mg/ml neutralized collagen solution and 6% stock alginate solution were mixed together on ice and injected around a PDMS mold to generate 4-mm wells as described above. Instead of a PDMS "cover" as used for the 2% collagen wells, a 2μm porous filter was placed on each cylindrical mold. The collagen portion of the gels were then allowed to polymerize by placing the entire PDMS mold in at 37 °C in 5% CO_2 for 30 minutes. Gels/molds were removed from the incubator and a 60 mM calcium chloride solution was placed on top of the 2 μm filter overnight at room temperature in order to crosslink the alginate. Finally, the filter papers were removed; the alginate/collagen constructs were pealed from the PDMS mold and were placed in wells of a 48 well-plate. Each construct was incubated with growth media at 37 °C for at least 3 hours before use. Cell seeded collagen (0.3%) solutions were allowed to polymerize in the alginate/collagen wells at 37° C and 5% $C0_2$ for 20 minutes. The entire well was placed in a 48-well plate, and 300 μl of vasculogenesis media (described in Appendix A-3) was added to each.

5-4 Collagen structure near boundaries

Here, we describe our preliminary observations regarding the collagen structure near the PDMS and permeable boundaries. Because we are interested in how

cells behave near these boundaries, it is crucial to understand the local collagen fiber orientation and density near and directly on these surfaces. The collagen fibers that we will use to quantify alignment will be visualized with confocal fluorescence microscopy as in Figure 5-4a,b. A *z*-stack of confocal images through the *z* plane of a collagen gel adhered to a PDMS boundary is rendered into a *xz* plane image in Figure 5-4c. Based on initial imaging of collagen structure near the PDMS, 2% collagen, and 4% alginate/0.3% collagen boundaries, we do not see significant fiber alignment. However a quantitative alignment analysis needs to be done to verify our observations.

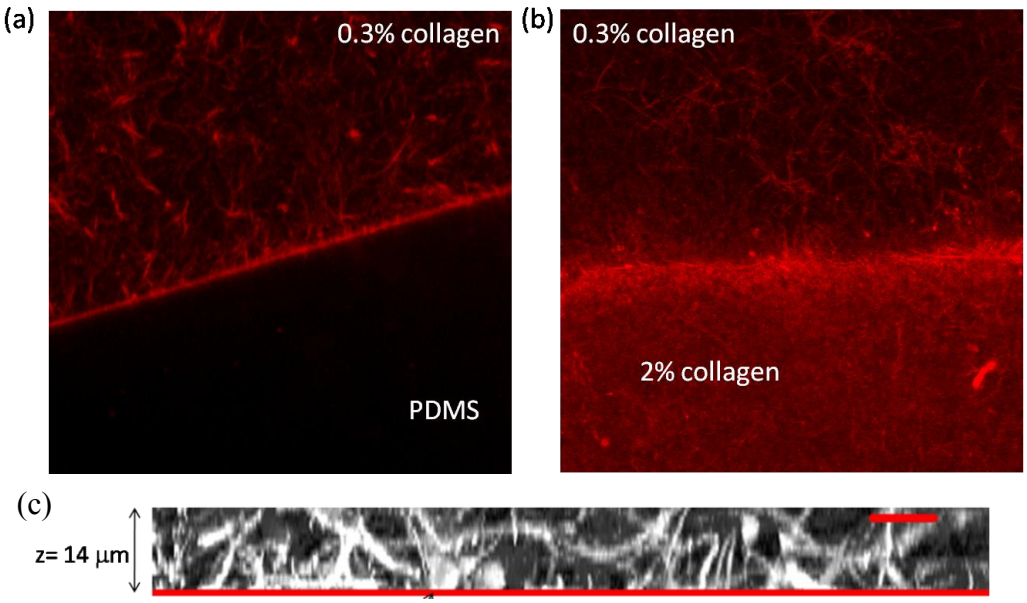

Figure 5-5. Collagen structure near boundaries. (a) *xy* plane of fluorescently labeled 0.3% collagen near an adherent PDMS boundary. (b) *xy* plane of fluorescently labeled 0.3% collagen near 2% collagen boundary. (c) *xz* plane (image reconstructed from confocal z-stacks) of fluorescently labeled 0.3% collagen near an adherent PDMS boundary (bottom). Scale bar = 10μm.

We are currently working to quantify the fiber alignment near different boundaries and within the bulk using a Fast Fourier Transform-based image analysis program in MATLAB. Using this program we will be able to quantify fiber alignment

via an alignment angle and an alignment index. The alignment index will be calculated as the fraction of fibers in a 40 degree arch of the angle of maximum alignment.

5-5 Time-lapse experiments for boundary condition assay

Cells were seeded at low density ($5x10^4$ cells/ml) to avoid potential effects of local signaling by neighboring cells. As described in Chapter 4, in the time course of a given experiment, at least 10, *xyz* positions were set on the microscope stage so that multiple cells could be analyzed during a single experiment. The stage returned to those positions at every time point. A set of 3 images, spaced by 25 μm in the *z*, were collected at each position at each time point resulting in a *z*-stack (75 μm-deep) around the original center of every cell. Time course experiments were taken for at least 24 hours with manual re-focusing of the stage every 4-5 hours.

At the conclusion of the 24 hour time lapse experiment, the plane at each time point that was in focus was used to generate a 2-D movie of cell and matrix movements over 24 hours. The embedded microspheres (Fluoresbrite™ Carboxylate YG 1.0 micron Microspheres; Polyscience, Inc., Warrington, Pennsylvania), physisorbed to the collagen matrix and the permeable boundary hydrogels, were used to observe deformation of the matrix or deformation of the boundaries. No deformation was observed in association with the dynamics of protrusions. The *xy* coordinates of the cell centers, a reference microsphere (at least 200 μm from the cell of interest), and the boundary were identified using Image J software.

In addition to tracking cell centers, a reference bead, and the boundary location, the *xy* coordinates of the end of each protrusion at its maximum length were identified manually (Figure 5-6a) identical to the protrusion analysis section in Chapter 4. A protrusion map was generated (Figure 5-6b), and again, the average protrusion frequency and length were calculated. The mean angle and resultant vector were

calculated based on a unit circle (Figure 5-6c) as described in the Chapter 4, *4-5 Protrusion analysis* section.

5-6 Cell behavior near boundaries

The behavior of single cells that were ~10-130 μm from a boundary (center of mass of cell to edge of boundary) was analyzed using brightfield microscopy live-imaging. We plot cellular behaviors as a function of initial cell-boundary separation

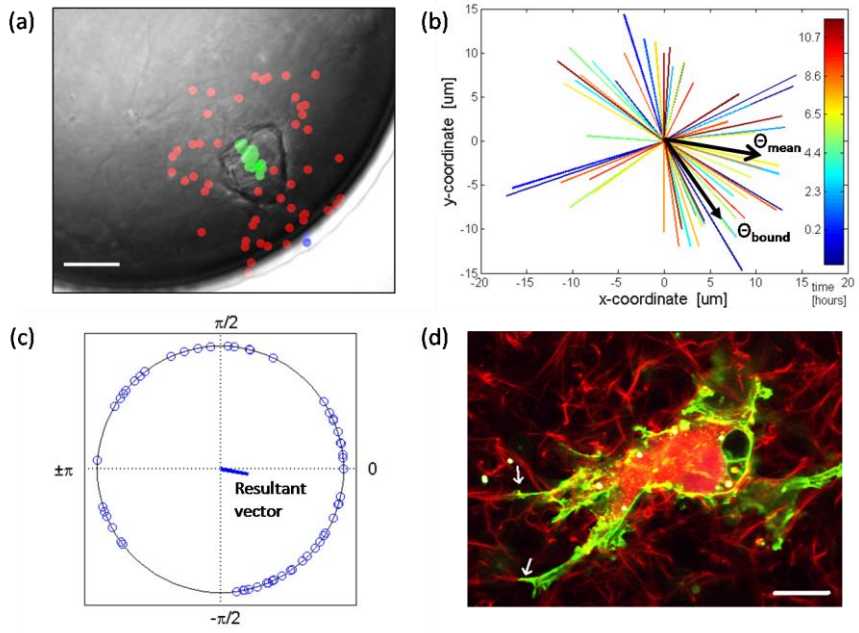

Figure 5-6. Analysis of protrusion dynamics. (a) Bright field image formed by merging 72 frames captured at 10 minute intervals over 12 hours. A cell near an impermeable boundary is shown. Tracking was performed on protrusions at their maximum extension (red circles), the cell center (green circles) and the boundary (blue circle). Scale bar = 20 μm (b) Protrusion length and angle from the cell center in (a) with color-coded time information. The mean angle, Θ_{mean}, and the mean angle towards the boundary, Θ_{bound}, are labeled. The mean angle towards the boundary, $\Theta_{bound,}$ is the predicted direction of protrusions, ϕ_A used in the statistical analysis of directionality. (c) The protrusions from (b) are plotted on a unit circle and the resultant direction and length is shown and labeled. (d) A confocal image of an endothelial cell stained with AlexaFluor 488 phalloidin in TRITC-labeled collagen illustrates that the cell sends out protrusions along collagen fibers during their search process (arrows). Scale bar = 20 μm.

in Figure 5-7. We see that a cell will touch and usually connect if it is within ~ 35-45μm from a solid, impermeable boundary (PDMS) (Figure 5-7a).

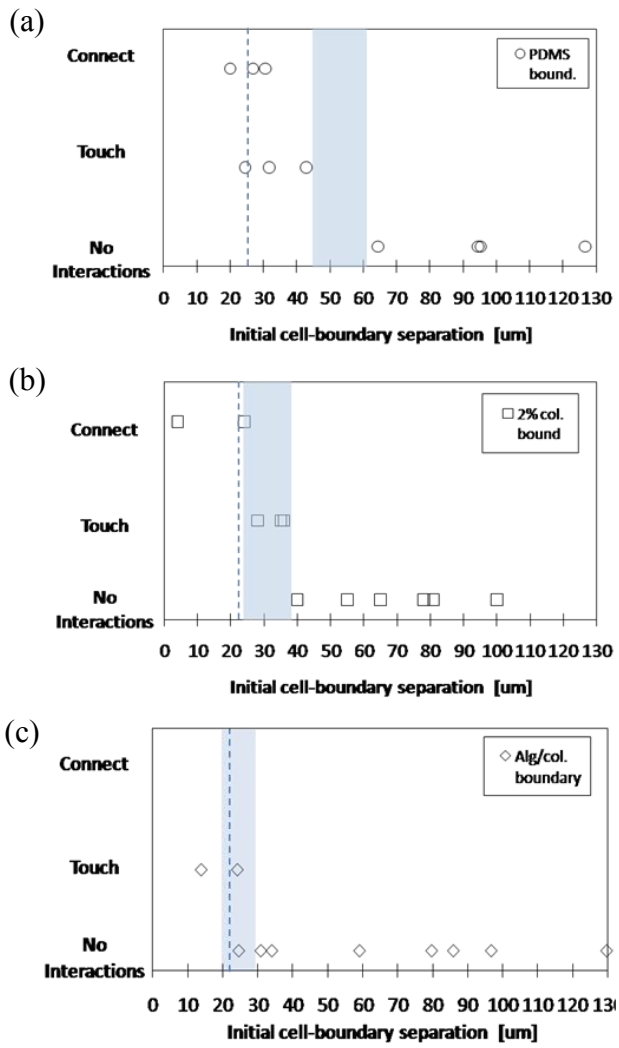

Figure 5-7. Cell-boundary interactions as a function of initial cell-boundary separation. (a-c) Each point represents a cell that started the given distance from the boundary on the x-axis. The light blue bar highlights the critical region at which a cell begins to touch a boundary. The vertical dashed line represents the average protrusion length of the cells (protrusion length analysis can be found in Figure 5-7). Conditions: (a) single cells near boundary made of PDMS in control medium; (b) single cells near boundary made of 2% collagen in control medium; (c) single cells near boundary made of 4% alginate/0.3% collagen in control medium.

As expected, this length scale is approximately half of the length scale of ~ 65 μm that was found for cell-cell interactions in Chapter 4 (because in the boundary-cell interaction, we only have one cell sending out protrusions). A cell near a solid, permeable boundary (Figure 5-7 b,c) of either 2% collagen or 4% alginate/0.3% collagen does not touch the boundary unless it is within ~ 20-35μm. We do not see cells connect with the alginate/collagen wall, but we do see connections on the 2% collagen wall.

To determine how these length scales for touch relate to the cellular protrusion length, we quantify the average protrusion length of the cells for each of the boundary condition cases (Figure 5-8a). We also plot the average protrusion length of isolated cells and cell pairs as a comparison to the boundary cases. There is no significant difference in protrusion length between isolated cells and cell at any distance from a permeable boundary (Figure 5-8b). Interestingly, cells near (<65 μm) an impermeable, PDMS boundary have significantly shorter protrusions than isolated cells. We also quantify protrusion frequency and see no significant difference in frequency for isolated cells, cell pairs, or the presence of a permeable boundary. Protrusion frequency is significantly higher when a cell is near a solid boundary (PDMS) as compared to isolated cells or cells near a permeable boundary

Returning to Figure 5-7, we plot the average protrusion length as a dotted vertical line. The average protrusion length is significantly smaller than the critical interacting/touching state (the blue shaded region) for the PDMS boundary but is not significantly different from the transition to the interaction/touching state for either of the permeable boundaries. These results indicate that cells are interacting at a distance with the impermeable boundary but not with the permeable boundaries.

(a)

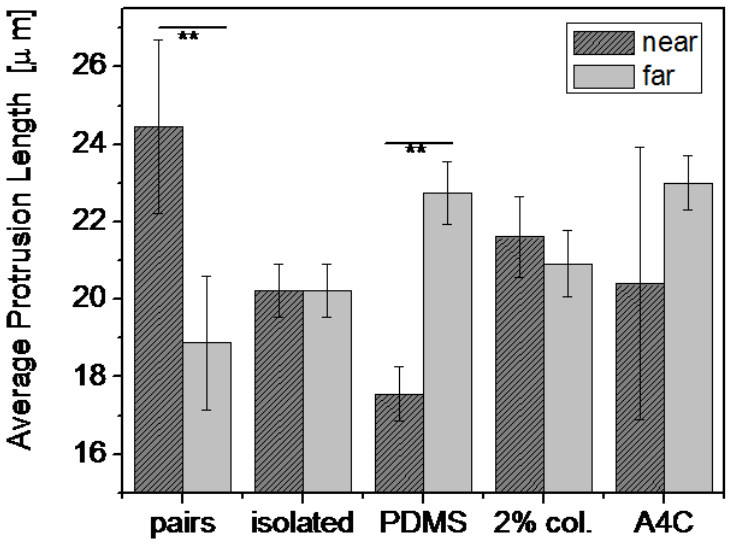

(b)

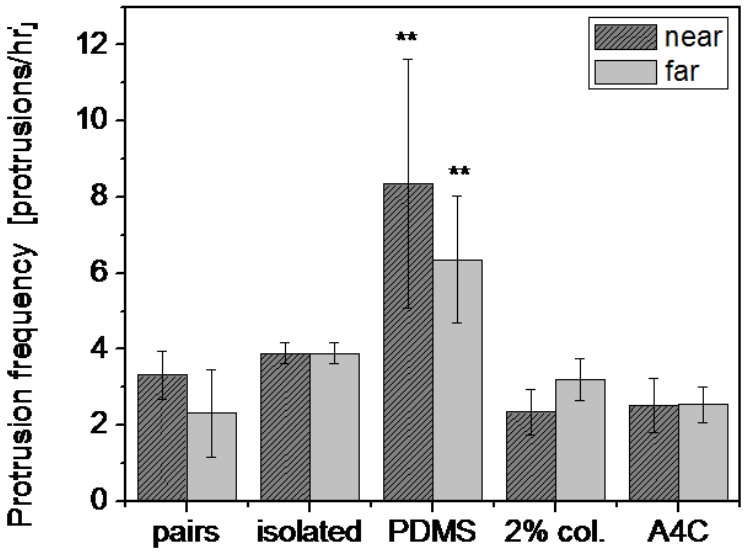

Figure 5-8. Protrusion frequency and length analysis for cells near various boundary conditions. Cell pairs and isolated cells are included for comparison. Dark grey bars (near) represent cells <65 μm from another cell or < 32μm from a boundary. Light grey bars (far) represent cells >65 μm from another cell or > 32μm from a boundary. Pairs = two cells; isolated= single cell; PDMS= single cell a given distance from a PDMS boundary; 2% col. = single cell a given distance from a permeable 2% collagen boundary; A4C= single cell a given distance from a permeable 4% alginate/0.3% collagen boundary. Error bars represent 99% confidence intervals. $p<0.01$ (**), $p<0.001$ (***). The number of cells and protrusion analyzed can be found in Tables 5-2 and 5-3.

Similarly, the results from Figure 5-8 show that cell protrusions near a PDMS boundary are distinct from cellular protrusions near a permeable boundary. Cells are immediately drawn to the PDMS boundary and flatten onto the boundary, whereas, cells seem to maintain of distance from other cells for a significant amount of time and retain a more 3-D geometry. This 'flattening' behavior of cells near the PDMS boundary results in an almost immediate decrease of distance between the cell and the PDMS boundary, and therefore, shorter protrusion lengths for cell initially close to the boundary.

The significant increase in protrusion frequency for PDMS boundaries (Figure5-8b) suggests that cells in a soft, 3-D substrate prefer either a stiff substrate or the mass transfer effects that are produced by an impermeable boundary which are distinct from that of another cell. According to our numerical calculations in Figure 5-3 and Figure 5-4, the presence of the impermeable boundary may lead to a slightly higher concentration of soluble factors or amounts of stress than does another cell possibly explaining this difference. We cannot exclude the notion that a cell may prefer to attach to a stiff substrate rather than another cell. Recent 2-D studies suggest that cells migrate preferentially towards stiffer surfaces[12, 13] and neutrophils moving in 3-D matrices have been shown to move along the most rigid fibers after probing their local environment[14].

5-7 Protrusion clustering and directionality

In this section, we describe our work quantifying the directionality of protrusions to see if they show a bias in the direction of a boundary. We quantify protrusion clustering using the resultant length, R, as described in Chapter 4.
To reiterate, the resultant length is an indication of the relative dispersion or concentration of the protrusion directions. The resultant length approaches 1 under strong directedness but approaches 0 under circular uniformity.

When a cell <32 μm away(near) from an impermeable boundary (PDMS), there is significant protrusion clustering as compared to isolated cells (Figure 5-9). Cells near either permeable boundary (2% col. or A43) do not have a significantly different resultant length (indicating less clustering of protrusions) as compared to isolated cells. We compare to isolated cells as they are in a completely isotropic and uniform chemical and mechanical environment. Because the permeable boundaries are rigid, these results suggest that mass transfer is responsible for protrusion clustering.

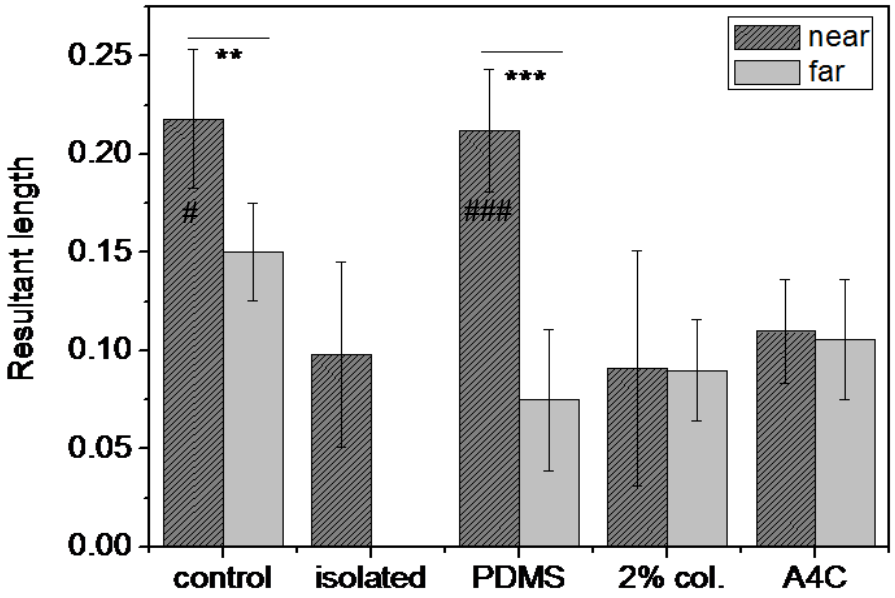

Figure 5-9. Resultant length. The resultant lengths were calculated from protrusion directions using a unit circle as described in the circular statistics analysis section of Chapter 4. The light bars (far) indicate when a cell is > 65 μm from another cell or > 32 μm from a boundary. Dark bars (near) indicate when a cell is < 65 μm from another cell or < 32 μm from a boundary. In the isolated condition, there can be no separation dependence, so the dark bar represents all isolated cells. Data represent the average resultant length from at least 8 different cells. Error bars represent the 99% confidence intervals. Asterisks represent significant differences in resultant length compared to isolated cells. $p<0.001$ (***); $p<0.01$ (**); $p<0.05$ (*). See Table 5-2 and 5-3 for sample numbers. The V-test was used to determine if cell protrusions showed a bias in the direction of another cell $p<0.001$ (###); $p<0.01$ (##); $p<0.05$ (#) are shown.

We analyzed the specific directions of protrusions using the circular statistical V-test with the circular statistics toolbox for MATLAB as described in Chapter 4 and again, we separated the cells into near (<32 μm) a boundary or far (> 32 μm).

The protrusions of 14 cells that were near a boundary were analyzed with a total of 863 protrusions (Table 5-2). Each of the cells' protrusions underwent the V-test (see Chapter 4). By applying the V-test, we could determine if the protrusions were significantly directed towards the boundary and if the directedness was dependent on initial separation from that boundary. For the pairs near the PDMS boundary, 100% of the cells analyzed (3/3) had their protrusions significantly ($p<0.05$, $p<0.01$, or $p<0.001$) directed towards the other cell (### in Figure 5-9 and Table 5-2). In contrast, only 1/6 (16.7%) and 2/5 (40%) of the cells near the two permeable boundaries showed significant bias in the direction of the boundary. All of these statistics included cells from before and after the first contact was made. Making this distinction did not change the results; however, in almost all *near* cases, a protrusion made contact with the other cell or boundary before enough time elapsed to track enough protrusions to perform a rigorous statistical analysis.

The protrusions of a total of 13 cells that were > 32 μm from a boundary, were analyzed with a total of 791 protrusions (Table 5-3). Note that all of the cells > 32 μm from the solid impermeable boundary showed significant bias in the direction of the boundary and only 4/11 of the cells near a permeable boundary showed significant bias in the predicted direction (Table 5-3). Isolated cells (>200 μm from another cell or boundary) were significantly biased in direction (predicted direction just set to 0) in 2/6 (or 33.3%) instances. Isolated cells should have no signal to bias their search, so this data represents a purely random protrusive search.

Table 5-2. Directionality of protrusions for cells < 65 μm from another cell (control) or < 32 μm from a boundary.

Condition	nprotrusions	ncells	ncells ***p < 0.001	ncells** p < 0.01	ncells* p < 0.05	% sig. directed
control	331	12	4	3	4	91.7
PDMS	258	3	3	--	--	100.0
2% collagen	326	6	1	--	--	16.7
alginate/collagen	279	5	2	--	--	40.0

Table 5-3. Directionality of protrusions for cells > 65 μm from another cell (control) or > 32 μm from a boundary.

Condition	nprotrusions	ncells	ncells *** p < 0.001	ncells** p < 0.01	ncells * p < 0.05	% sig. directed
control	217	6	1	1	--	33.3
PDMS	243	2	2	--	--	100.0
2% collagen	497	6	2	--	--	33.3
Alginate/Collagen	294	5	2	--	--	40.0
isolated cells	313	6	2 (ϕ set to 0)	--	--	33.3

5-8 Conclusions

Our results pertaining to protrusion clustering (Figure 5-9) and directionality (Tables 5-2 and 5-3), showed that there is directional bias in protrusive activity for a cell near an impermeable boundary and not for cells near impermeable boundaries. Since the permeable boundaries are essentially transparent to mass transport (Figure 5-3civ and Figure 5-4) but are mechanically similar to an impermeable boundary, the observation that no protrusion bias is seen near the impermeable boundaries is compatible with the hypothesis that protrusions sense a soluble signal.

Using our boundary condition assay, we demonstrated that mass transfer is a likely mechanism of communication directing cell protrusion activity. We have focused on endothelial cell behavior and interactions, but methods we developed could be used to investigate communication mechanisms for other cell types in other scaffold materials.

REFERENCES

1. Serini, G., et al., *Modeling the early stages of vascular network assembly.* Embo J, 2003. **22**(8): p. 1771-9.

2. Ambler, C.A., G.M. Schmunk, and V.L. Bautch, *Stem cell-derived endothelial cells/progenitors migrate and pattern in the embryo using the VEGF signaling pathway.* Dev Biol, 2003. **257**(1): p. 205-19.

3. Gerhardt, H., et al., *VEGF guides angiogenic sprouting utilizing endothelial tip cell filopodia.* J Cell Biol, 2003. **161**(6): p. 1163-77.

4. Reinhart-King, C.A., M. Dembo, and D.A. Hammer, *Cell-cell mechanical communication through compliant substrates.* Biophysical Journal, 2008. **95**(12): p. 6044-51.

5. Oster, G.F., J.D. Murray, and A.K. Harris, *Mechanical aspects of mesenchymal morphogenesis.* J Embryol Exp Morphol, 1983. **78**: p. 83-125.

6. Davis, G.E. and C.W. Camarillo, *Regulation of endothelial cell morphogenesis by integrins, mechanical forces, and matrix guidance pathways.* Exp Cell Res, 1995. **216**(1): p. 113-23.

7. Bach, T.L., et al., *VE-Cadherin mediates endothelial cell capillary tube formation in fibrin and collagen gels.* Exp Cell Res, 1998. **238**(2): p. 324-34.

8. Vittet, D., et al., *Targeted null-mutation in the vascular endothelial-cadherin gene impairs the organization of vascular-like structures in embryoid bodies.* Proc Natl Acad Sci U S A, 1997. **94**(12): p. 6273-8.

9. Yang, S., et al., *Functional roles for PECAM-1 (CD31) and VE-cadherin (CD144) in tube assembly and lumen formation in three-dimensional collagen gels.* Am J Pathol, 1999. **155**(3): p. 887-95.

10. Armani, D., Liu, C., Aluru, N. . *Re-configurable fluid circuits by PDMS elastomer micromachining*. in *12th Int. Conf. on MEMS*. 1999. Orlando, Fl.

11. Gillette, B.M., et al., *In situ collagen assembly for integrating microfabricated three-dimensional cell-seeded matrices.* Nat Mater, 2008. **7**(8): p. 636-40.

12. Lo, C.M., et al., *Cell movement is guided by the rigidity of the substrate.* Biophys J, 2000. **79**(1): p. 144-52.

13. Gray, D.S., J. Tien, and C.S. Chen, *Repositioning of cells by mechanotaxis on surfaces with micropatterned Young's modulus.* Journal of Biomedical Materials Research Part A, 2003. **66**(3): p. 605-14.

14. Mandeville, J.T., M.A. Lawson, and F.R. Maxfield, *Dynamic imaging of neutrophil migration in three dimensions: mechanical interactions between cells and matrix.* J Leukoc Biol, 1997. **61**(2): p. 188-200.

CHAPTER 6

CONCLUDING REMARKS AND FUTURE DIRECTIONS

Throughout this dissertation, I have highlighted the experiments, observations, and results that I feel contribute towards the understanding of cellular self-organization during vascular network formation. I have also reported upon the developments associated with our characterization of a dense collagen matrix that has the potential to be an experimental platform for both *in vivo* and *in vitro* cellular-, tissue-, and organ-scale research.

We have demonstrated that dense collagen matrices are mechanically robust while maintaining the ability to be remodeled by endothelial cells. A collagen concentration of 1.0% was the threshold matrix density that permits cellular invasion and endothelial network formation while still supporting microfabrication and a functional (perfusion without leaks for 3 weeks) microfluidic device. Because the dense collagen can be both microfabricated and remodeled by cells, there is potential to control the spatial and temporal chemistry and fluid mechanics seen by endothelial cells and cells in the bulk within these scaffolds while observing of cellular invasion and angiogenesis.

Currently, our lab is endothelializing the channels within the collagen microfluidic network and is using it as a platform to study tumor angiogenesis. The vascular structure grown within the microfabricated dense collagen scaffold could be used as the base state for investigating the maturation of the primary vascular plexus and the initiation of angiogenesis *in vitro*. Using our system, we will be able to observe the mechanisms of remodeling and the tendency of capillaries to branch, undergo intussusceptions, or regression as we change the mechanical or chemical environment across the plexus of endothelial cells. We will also be able to study the

roles of proliferation, migration, and recruitment of supporting cells in the maturation process. Finally, an endothelial cell-lined microfluidic channel within a cell-seeded collagen gel is a means to create an accessible, functional microvascular network *in vitro* that can be used supply thick engineered tissue constructs with the necessary nutrients and oxygen for survival and direct the development of complex tissues.

By altering the cell-seeding density within the 3-D collagen matrix, we performed a simple assay of the cellular self-organizational process. We have performed a percolation analysis and find the critical cell seeding density for 3-D percolation to be at an initial seeding density of $2x10^6$ cells/ml, corresponding to an initial cell-cell separation of ~ 79 μm. The cell-cell separation of ~ 79 μm could be associated with the extent of cell migration, the amount a cell can stretch, or an "action-at-a-distance" mechanism that propagates through the collagen matrix. The work reported in this chapter led us to additional experiments, reported in Chapters 4 and 5, designed to determine the origin(s) of this length scale.

In Chapters 4 and 5, we turned to a low cell seeding density and live cell imaging. The most striking cell behavior demonstrated in the 3-D matrix was the dynamic cellular protrusion activity of cells. During the first 24 hours of culture, endothelial cells sent out numerous filopodial extensions through and along the collagen matrix. By analyzing the protrusion dynamics and directionality of cells we showed that the critical cell-cell separation for cell pair interactions is ~ 65μm. Our findings are compatible with the hypotheses that cell protrusions are used as a sensing structure; however, one of the most basic outstanding questions, whether or not cells interact at a distance through their extracellular matrix, remains unclear.

cell-cell search.

Additionally, we have demonstrated that using boundary conditions allows us to separate mechanical from mass transfer-based mechanisms of local cell-cell

communication. By tracking the cell protrusion dynamics and analyzing the directionality of protrusions cells near both impermeable and permeable, stiff boundaries, we showed that cell behavior is compatible with the hypothesis soluble chemical gradients are the primary mechanism responsible for directing cellular protrusion activity in 3-D collagen matrices.

Further work needs to be performed to verify the initial result that chemical gradients direct protrusion activity. By setting up a linear gradient of a select number of soluble molecules using a microfluidic device, we can confirm (or reject) that protrusions are directionally biased. Live confocal fluorescent imaging will be a critical step to improving the visualization of cellular protrusive activity as well as a means to visualize the complete three-dimensionality of the cell behavior. The transfection of endothelial cells with GFP-actin will be a logical way to fluorescently visualize the thin, dynamic protrusions sent out by endothelial cells. Fluorescent confocal images should have higher contrast and resolution as compared to brightfield images and should allow for us to automate the protrusion analysis and cellular tracking protocols. Furthermore, this automation will permit a larger sample size.

While there remain significant challenges in the fields of developmental biology, vascular biology, tumor angiogenesis, and tissue engineering, this work and the work cited in this dissertation have contributed a piece of the foundation of knowledge in each of these fields.

APPENDIX A

EXPERIMENTAL PROTOCOLS

A-1 Reagents

Human umbilical vein endothelial cells (HUVECs), Medium 199 (M199), fetal bovine serum (FBS), L-glutamine, penicillin/streptomycin, trypsin/EDTA, HEPES buffered saline solution (Lonza, Basel, Switzerland). Endothelial cell growth supplement (ECGS), vascular endothelial cell growth factor (VEGF), basic fibroblast growth factor (FGF), phosphate buffered saline (PBS) (Upstate Cell Signaling Solutions, Lake Placid, NY). Rat tails (Pel-Freez Biologicals, Rogers AR). Phorbol-12-myristate-13-acetate (TPA), (Cell Signaling Technology, Danvers, MA). Heparin solution, Press-to-Seal® silicone isolators, Lab-Tec® chamber slides (Invitrogen, Carlsbad, CA). (poly)ethylenimine (PEI), GM6001, monoclonal antibody against human VE-cadherin, monoclonal antibody (clone GC-4) against human N-cadherin (Sigma-Aldrich, St. Louis, Missouri). Alexa Fluor 488 phalloidin, Alexa Fluor 568 phalloidin, 4',6-diamidino-2-phenylindole (DAPI), YOYO-1 iodide, (Molecular Probes, Eugene, OR). Soluble VEGFR-1 (sVEGF-R1), (R&D Systems, Minneapolis, MN). L-ascorbic acid (Acros Organics, Atlanta, GA). Triton X-100 (MP Biomedical, Solon, OH). (poly)-dimethylsiloxane (PDMS) (Sylgard® 184, Dow Corning, Midland, Michigan). Fluoresbrite™ Carboxylate YG 1.0 micron Microspheres (Polyscience, Inc., Warrington, Pennsylvania)

A-2 Passing human umbilical vein endothelial cells (HUVECs)

I use the large flasks that have surface area of 75 cm^2 (T75 flask). When a flask is 100% confluent, there are ~ $3x10^6$ cells in the flask. I usually pass the cells when they are about 85-95% confluent, and I re-feed the cells every 2-3 days. Usually I resuspend (1) T75 flask into 8 milliliters of media and put 4 ml of that into 4 new

flasks (so 1 ml/flask). This produces a 1:8 dilution. If I need a confluent flask of cells sooner or later than about 4 days, I will seed the new flasks at 1:4 or 1:16, respectively. For example, passing cells from (1) confluent T75 flask into (4) T75 flasks at a 1:8 dilution is described below. All procedures are done in the hood with sterile pipette tips, flasks, etc. Wear gloves as we are dealing with human cells (and for sterility purposes).

1. Wipe down hood with 70% EtOH.
2. Fill a small beaker about ¼ full of bleach (under the sink) and place in the hood. This will be your cell waste beaker.
3. Place pipette-aide and appropriate sized disposable pipettes in the hood so they are ready to use. I use a 50 ml pipette and (2-3) 10ml, 5ml, and 25 ml pipettes.
4. Place 15 ml of growth media (M199+supplements) into 4, T75 flasks.
1. Label side of flask with marker: Cell type, Date, Passage and Generation #, Your Initials
5. Place flasks in incubator to equilibrate. Also warm 50 ml vials of HEPES buffered saline solution, trypsin/EDTA, and growth media in the incubator until they are warm (~20-30 minutes). Wipe down vials with 70% EtOH.
6. Once the flasks and vials are warm, place them and the confluent flask in the hood.
7. Dump out old media into bleach beaker.
8. Rinse flask with ~10 ml of HEPES; dump out in bleach.
9. Add 3 ml of trypsin/EDTA and place flask in incubator for ~1 minute. Place under scope to ensure that cells have rounded up off of the flask.
10. Dump out trypsin and tap flask to detach cells.
11. Neutralize/resuspend cells in 8 ml of growth media. Pipette up and down and on the flask bottom surface to detach and suspend cells homogenously.

12. Place 1 ml into each new flask (the ones that have 15 ml media in them). Swirl flasks to distribute cells and place in incubator.

If you want to resuspend to a specific number of cells/ml (like when setting up an assay), from step 11:

13. Place the 8 ml of growth media/cells into a 15 ml conical vial.
14. Weigh it on the balance and make a balance tube.
15. Spin at 1200rpm for 3min 30 sec in bench top centrifuge.
16. Cells will form a visible pellet in the bottom of the tube. Pour out supernatant carefully. Tap vial to loosen pellet in residual media left in vial.
17. Add 1 ml media and pipette up and down to resuspend cells.
18. Use ~ 50 ul on the hemocytometer to count how many cells you have in the 1 ml.
19. Add media to get the desired cell concentration.

A-3 Preparation of growth media and vasculogenesis media

Growth Media (500ml bottle)

500 ml M199 (in fridge)

20% FBS= 100 ml (in freezer, must be thawed for ~ 1 day)

20ug/ml endothelial cell growth supplement (ECGS)= 15 mg (in freezer)

5 U/ml heparin= 250 ul of 10,000U/ml stock (in fridge)

150 Units/ml Pen/Strep = 7.5 ml stock (in freezer, must be thawed)

2 mM L-glutamine = 6 ml stock (in fridge)

Vasculogenesis Assay Media (10ml)

9840 ul Growth Media

16 ul TPA (200 uM in DMSO stock) = 50 ng/ml (in freezer)

40 ul VEGF (0.01 mg/ml stock) = 40 ng/ml (in freezer)

16 ul FGF (0.025 mg/ml stock) = 40 ng/ml (in fridge)

100 ul ascorbic acid (5mg/ml stock) = 50 ug/ml (in fridge)

A-4 Harvesting Type I Collagen from Rat Tails

The collagen extraction procedure should be performed in a sterile environment since it will be used for cell culture.

Extraction:

1. Autoclave necessary instruments and sterile filter the acetic acid into a sterile bottle.
2. Clean hood with 70% EtOH and place sterile instruments, scalpel blade, a 400ml beaker, 70% ethanol, and 2 large Petri dishes into the hood.
3. Place frozen tails in a large Petri dish filled with 70% ethanol (in the biohood). Let them soak for about 15 minutes to let them thaw. Fill the beaker and another Petri dish with 70% ethanol. You will perform the rest of the steps under ethanol and in the hood.
4. Cut about 1 cm off of the thick part of the tail and the very tip of the end of the tail with the razor blade.
5. Cut a straight line down the length of the tail. Try to only cut the outer epidermis layer. Hold the tail at the base (thick end) with the hemostat and peel away the outer skin layer with the other hemostat and discard.
6. Now you should be able to see silvery tendons running down the length of the tail. Hold the tail at the base, grab a tendon at the tip of the tail and pull the tendons in the direction of the tail tip. Make sure to clean the tendon of all fat and/or fascia that may be stuck on the ends. Place clean tendon in the beaker of ethanol.
7. Continue to grab tendons from the tip of the tail. When no more are available, cut the tip of the tail to the next joint and repeat with the exposed tendons. Work your way up to the base until no tendons are left.

8. Place a 50 ml conical tube on the balance and tare the balance to 0.
9. Using forceps, raise the tendon mass (in the beaker of EtOH) to the air and gently shake and allow to dry briefly (10-20 seconds). Place in the 50 ml conical tube and weigh the tendons. Don't leave tendons exposed to air for too long or they will dry out.
10. Using a pipette-aid, add 0.1% acetic acid to the conical tube with the (between 75-100 ml/gram of tendon).
11. Allow the collagen to solubilize for at least 48 hours at 4° C. During this time, periodically agitate the tube. The tendons will swell to occupy a large part of the total solution volume.

Centrifugation:

1. Weigh collagen tube and make a balance tube by filling it with the same weight (within .001g) of water.
2. Take down to NBTC on ice. (Note: keep collagen solution on ice at all times)
3. Reweigh the tubes carefully, making sure that the tubes that are directly opposite from each other are perfectly balanced.
4. Centrifuge in the NBTC Hettich at 4° C, RCF: 8800 xg, RPM 8920, radius 99mm with the rotor for 50 ml conical tubes for 1 hour.
5. In the hood, collect the clear supernatant and discard the pellet or any cloudy material. (you can also add more acetic acid and spin down again).
6. Place the supernatant in a new, sterile 50 ml tube.
7. Freeze dry/lyophilize the clear collagen solution until it is completely dry (usually takes a few days).
8. Dried collagen (looks like cotton candy) can be kept in the freezer for many months.

9. Resuspend dry collagen in appropriate amount of 0.1% acetic acid to reach the desired concentration of stock solution. Collagen solution should be used within ~ 3 months.
10. Allow to completely dissolve at 4 deg. C for at least 2 days (or until it is completely clear). Agitate periodically.
11. It is now ready to use.

A-5 Gelation Protocol for Type I Collagen

Solubilized type I collagen is a heterodimer 300 nm in length composed of two alpha $_1$(1) chains and one alpha$_2$(1) chain. When the pH of the collagen solution is brought to neutral (6.5-7.5) and when its temperature is raised about 4° C, the triple helices will laterally associate to form large fibrils and the collagen solution forms a gel. Be sure to always keep collagen solutions on ice or in the fridge. In addition, when making 3-D gels for cellular applications, perform the following protocol in a sterile biohood with sterile solutions, tubes, and instruments.

Procedure:

1. Place on ice:
   A. 1x M199
   B. 10x M199
   C. 1N. NaOH
   D. Collagen stock solution
   E. Empty conical vial
2. Determine the desired final volume and concentration of collagen solution needed.
3. Add to the empty tube the following volume of 10x M199
   Final volume/10 = ml 10x M199
4. Calculate the volume of collagen to be used (do not add to the M199 yet)

Final volume x final collagen concentration in mg/ml/ stock concentration = volume of collagen to be added

5. Add to the 10x M199 the following volume of ice cold 1N NaOH
(volume of collagen to be added)x 0.02 ml = volume 1N NaOH
6. Add to the 10xM199/1N NaOH the following volume of ice cold 1xM199:
(final volume)-(volume collagen)-(volume 10xM199)-(volume 1N NaOH) = volume 1x M199 to add
7. Mix the tube and hold on ice.
8. Add the calculated volume of collagen and mix carefully (try not to get any bubbles).
9. Test the pH with a pH strip or use color indicator of media. It should be light pink. If it is still acidic (over ~7.5), it will be yellow. Add a SMALL amount of NaOH (~1microliter) until it is pink. If it is purple, then it is too basic. Start over.
10. Leave on ice until ready to use. At this point cells can be mixed in with the collagen. (use neutralized collagen within 1 hour)
11. Place desired amount of collagen in well. Allow to gel at 37 degrees in the incubator for ~30 minutes.
12. Place 1xPBS or 1x M199 on gels to keep them hydrated.

A-6 Adhering collagen to a substrate

Glass Treatment Protocol:

1. Clean substrate with soap and water, EtOH, and water; dry.
2. Plasma clean for 4 minutes.
3. Place plasma cleaned samples in a sterile 1.0% PEI solution and let sit for 10 minutes at room temperature.
4. Remove from PEI, rinse with sterile water, and dry.

5. Place samples in 0.1% glutaraldehyde solution for 30 minutes at room temperature.
6. Remove from glutaraldehyde and rinse with sterile water. If preparing a substrate which will be used in combination with cells, wash the glutaraldehyde coated substrate multiple times in clean water baths to wash away ALL excess glutaraldehyde. I usually do three, 15 minute washes on the shaker. You can also wash overnight. I smell the last water bath….if there is any glutaraldehyde odor, it needs more washing.
7. Dry substrate completely before using.

Note that the collagen gel will only attach to the substrate if it is allowed to gel on the treated surface. Simply placing collagen that is already gelled on a treated substrate will not work.

A-7 General Fixing and Staining protocol used for HUVECs in collagen gels

1. Fix with 3.7% formaldehyde in PBS for 30 minutes on shaker.
2. Wash 2x for 15 minutes with PBS.
3. Permeablilize with 0.5% Triton X for 10 minutes.
4. Block with 1% BSA in PBS for 30 minutes on shaker.
5. Incubate with AlexaFluor 568-phallaidin (10 ul stock for every 200 ul) for 1 hour on shaker.
6. Wash 2x for 15 minutes with PBS on shaker.
7. Incubate with 500nM YOYO-1 for 30 minutes on shaker.
8. Wash 2x for 15 minutes with PBS on shaker.

A-8 Confined compression testing protocol for collagen gels

Testing the sample

1. Place 250 gram load cell (Honeywell Sensotec, Columbus, OH). on the Enduratec ELF-3200 test system (Bose EnduraTEC, Minnetonka, MN) stage and connect to the back of the computer in the '250g' port. Be sure that the '250g' label on the load cell is facing up. Place the appropriate sized plastic ring (probably the 8 mm) in the cup and secure with the screws. Screw cup onto load cell and pour PBS in the cup. The more PBS you put in, the harder it is to get the gel in place. You want to be sure that the PBS covers the gel and the PE plug, though.
2. Turn on the Endurotec by flipping both switches in the back.
3. Open Wintest, Cdrive, program files, EnduraTEC, Valerie250g
4. Place sample in cup by carefully scooping it in PBS. Using a spatula or forceps, guide the gel into the hole. Place polyethylene plug (8mm) in the cup and guide it to sit above the gel. Loosen load cell and slowly lift it to right below the probe….just touching the probe (not the cup) so the plug and gel do not float away.
5. Click on the Local icon and turn on to 'High'.
6. Tare and position. In the top menu, go to Set-up, Channels, Load-250g, Tare. Adjust gram reading so it is ~ 0g. Go to the 'Home' tab. Set home to 0.000mm.
7. Calculate 30% compression with 5% step size.
    a. Example: 30% of 2 mm = 0.6 mm
        i. 5% of 2 mm = 0.1 mm = step size
    b. Based on this example we will have six steps, each of 100 microns (0.1 mm)

8. Calculate the frequency = 1/sec
    c. Example: We want to let the sample fully relax after each step. To start, we'll have the relaxation time be long (20 min) however, we may be able to decrease this time once we see the relaxation time for a few samples. Frequency = 1/sec= 1/1200s = 0.0008333
9. Set scan time and scan points. Go to 'Timed Data' tab. One scan cycle cannot be more than 1000 seconds. In order for the machine to record the full 6 steps (each 20 minutes long = 7200 sec), we will need it to go through 8 cycles= 8000 seconds.
10. Set the steps and frequency from the calculations above. Go to Waveform: Disp. Add/Edit. Type the correct step size and frequency. You must do this for each step. Do not change the first step or other settings.
11. Show program where to save file: Go to 'Timed Data" and browse. Name a new file in your folder.
12. Slowly screw the top micrometer until the gram reading goes negative. Do this VERY slowly and watch the load as you are trying to make contact. You do NOT want to squish the gel; you just want to make contact! Once you see a 'dip' in the load, let it relax back to equilibrium (should only take a few seconds if you didn't squish the gel).
13. Begin testing: Go to Timed data, Start. Hit the Green Run button, Zero start, and say 'Yes' to the final box that pops up.
14. Watch the monitor until you see the machine take its first step. Once it has done its first step, you can leave and return when it is done.

Removing the sample

1. When the test is complete, the Local button will be green again and there won't be a red stop icon at the top. Your data is saved in the file that you specified before the test began.
2. Turn off the machine by flipping both switches.
3. Lower the load cell/cup by loosening the bottom screw. Remove the sample, porous plug, and the PBS. Place the plug back in the tube from the drawer. Discard the sample in the trash and pour the PBS down the drain. Rinse and wipe out the cup well and put it back in the drawer.
4. Remove the 250 g load cell and place gently back in the box in the drawer.
5. Exit the Endurotec program and save the .txt file to a portable USB if you want to take the data with you. There is no internet on the computer, so you can't email the files.

MATLAB Analysis: (using .m files from Dr. Lawrence Bonassar lab)

1. Name and save a new folder for each sample.
2. Rename text file data.txt and save in folder
3. Create an info.txt file with four lines:
    a. Thickness of sample (mm)
    b. Diameter of sample (mm)
    c. Step size (mm)
    d. # of steps
4. Create two empty folders and save as Analysis and Steps in the test folder.
5. Go to MATLAB and set path to correct .m files and folder.
6. Run chunkdata file. If okay, type 0.
7. Run SRcurvefit file.
8. Run DATAAnalysis file. Remove unwanted points to get linear region.

9. Set lower and upper bounds (example: Lower=1, Upper =6 for 6 steps)
10. Ha.txt file gives you modulus in Pascal*1000. Parameters.txt file has a column that gives τ for each step…usually values around 2-10. Use τ to find the specific permeability in cm^2 using sample thickness, equilibrium modulus, and viscosity of water.

APPENDIX B

AN ACTIVE WOUND DRESSING WITH CONTROLLED CONVECTIVE MASS TRANSFER[1]

B-1 Introduction

Acute cutaneous wounds and burns often involve damage to the underlying vascular structure, and this damage can lead to impaired transport of metabolites and immunoresponsive factors to and from the wound site. Chronic cutaneous wounds, such as those that develop in diabetic patients, suffer from an impaired healing response that is associated with biochemical imbalances; these wounds often fail to heal for weeks or months when treated with conventional wound dressings. Both of these classes of wounds would benefit from a tool that allows the clinician to monitor and control the soluble chemistry within the wound bed.

Conventional wound dressings—such as simple occlusive dressings—provide the basic functions required to allow wound healing, namely protection from outside agents and a barrier to evaporation. The advantages of conventional dressings are simplicity of application, familiarity, and low cost. The disadvantages of these dressings are the requirement of frequent changes, lack of specific biochemical or mechanical activity, and lack of external access to control and monitor the state of the wound bed. We are interested in the developing a dressing that can be used to treat difficult wounds in both mechanically and chemically active ways; such active dressings could be used to inhibit infection by clearing pathogens and delivering antibiotics, to provide diagnostic information about the state of the wound in real time, and to stimulate healthy healing responses.

B-2 An active wound dressing (AWD)

Working under Dr. Mario Cabodi, my project was to help design an active wound dressing (AWD) capable of delivery and extraction of solutes via externally

controlled convective mass transfer (Figure B-1). The device we ultimately made and characterized consisted of two separate materials that we covalently bind to form a bilayer: a thin, porous sheet of poly (hydroxyethyl methacrylate) (pHEMA) that contacts the wound surface directly and carries a pressure driven flow, and a sheet of

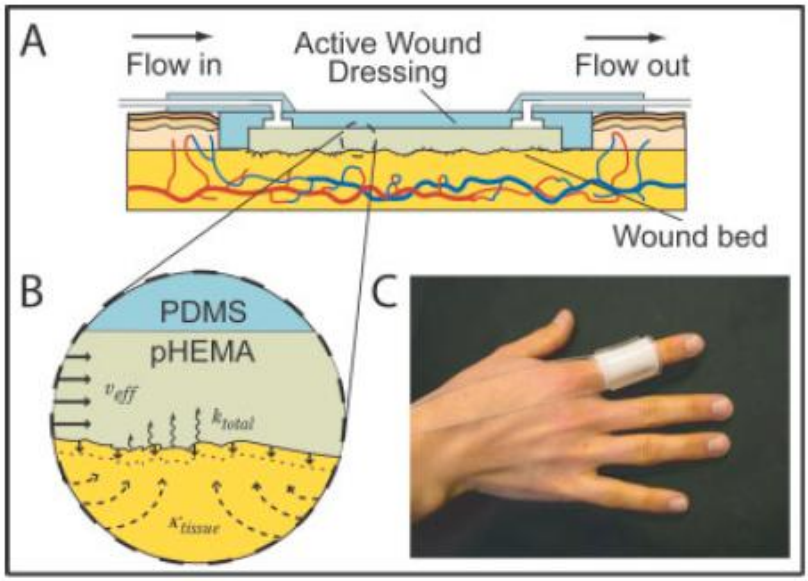

Figure B-1. Active wound dressing. (A) Schematic cross-sectional view of an AWD placed in a wound bed, with input and output flow connections. (B) Expanded view of the interface between the AWD and the wound bed illustrating modes of action of AWD: the wiggly arrows represent convective mass transfer with mass transfer coefficient k_{total} (cm/s) into a flow through the porous pHEMA sponge; the dashed arrows represent flow through the tissue (which has hydraulic permeability k_{tissue} (cm^2)); the bold arrows pointing into the tissue represent mechanical stress. (C) Image of an AWD adhered to a curved substrate (an uninjured index finger).

poly (dimethyl siloxane) (PDMS) that provides a vapor barrier and fluidic structures (fluid reservoirs and connections to the external pumping source). As illustrated schematically in Figure 1(B), the AWD can affect a wound in multiple ways: convective mass exchange from the surface of the wound bed, convective perfusion through the tissue, and application of mechanical stresses to the tissue. My specific roles in the project were to 1) help fabricate the bilayer dressing from PDMS and

pHEMA, 2) measure the convective permeability of the pHEMA sponge, and use this value to design a device with a spatially uniform flow profile, and 3) quantify the global coefficient of mass transfer of the AWD on a dissolvable synthetic surface, and compare it to existing theories of mass transfer in porous media. Below, I describe my results for quantifying the global mass transfer coefficient of the AWD.

B-3 Results

When placed in contact with a solid boundary, we can measure the global coefficient of interfacial mass transfer in order to quantitatively measure the efficiency of the AWD (Figure B-2). By solid boundary, we refer to one that is impermeable to convection (i.e., with specific Darcy permeability, κ_{tissue} much lower than that of the pHEMA sponge, $\kappa_{pHEMA} = 2.0 \times 10^{-9}$ cm^2 , but that can exchange solute by diffusion. In this situation, the flow of fluid driven through the dressing will be confined to pHEMA sponge and will not pass through the underlying tissue. Such a boundary mimics a tissue of low Darcy permeability, such as ligament ($\kappa_{lig} \sim 10^{-15}$ cm^2) or cartilage ($\kappa_{cart} \sim 10^{-14}$ cm^2). I used solid benzoic acid to mimic such a tissue.

To treat the limiting case of an impermeable substrate, we use the formalism of convective mass transfer in dilute solution, such that the global mass transfer coefficient, k_{AWD} (cm/s), is defined as:

$$k_{AWD} = \frac{J}{(C_s - C_\infty)} \qquad 1$$

where J (mol/cm^2 s) is the average molar flux from the wound bed into the dressing, C_s (mol/cm^3) is the concentration of a solute at the surface of the wound bed, and C_∞ (mol/cm^3) is its concentration in the incoming stream.

In the case of a dissolving substrate such as benzoic acid, we can assume local equilibrium such that the surface concentration is equal to the saturation concentration:

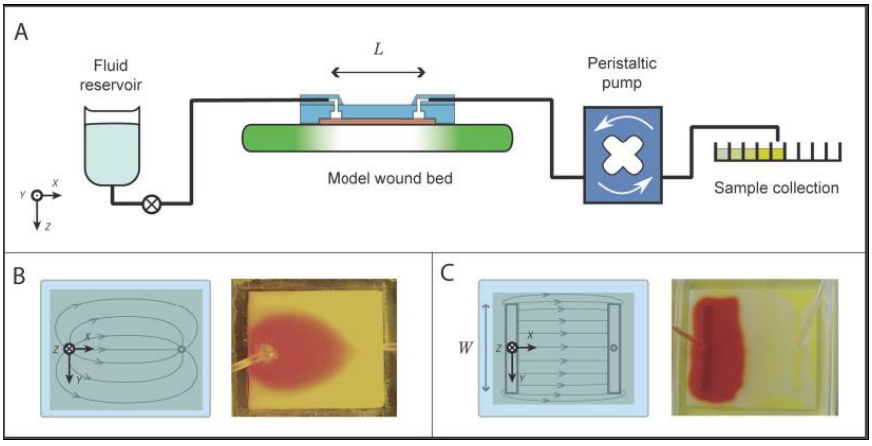

Figure B-2. Design and operation of the AWD. (A) Experimental setup: the assembled device was placed on the substrate, a fluid reservoir was connected at the inlet with the meniscus maintained at the height of the substrate, and a peristaltic pump was connected at the outlet and the fluid exiting it was collected. (B) Expected streamlines (left) for small reservoirs devices and observed advancing front of a solution of dye driven between reservoirs formed by the bores of the Tygon tubing butted up against the pHEMA sponge. (C) Expected (left) and observed (right) advancing front of a solution of dye driven between extended, low resistance reservoirs.

$C_s = 2.2 \times 10^{-5}$ mol/cm^3. We measured the mass flow rate by collecting the outlet solution on an analytical balance and the concentration of benzoic acid in the efflux by UV-vis absorbance; from these two values, we obtained the molar flux (mol/s) from the benzoic acid surface for multiple flow rates through the device.

Figure B-3 presents plots of the global mass transfer coefficient, kAWD, versus the mass flow rate of liquid through the porous layer, Q (cm3/s), for three different devices. We fitted these experimental data to a power law function of the form predicted by analysis of the mass transfer in this geometry:

$$k_{\mathrm{AWD}} = \frac{J}{(C_s - C_\infty)} = aQ^b \qquad 2$$

For the three devices we measured, we found $0.0010 < a < 0.0022$ and $0.41 < b < 0.55$. We note that there is some degree of variability between the different devices, and within the data points for the device 3. We believe possible sources for this variability to be variations in the structure of the sponge and substrate for different experiments, and channeling of fluid through irregularities in substrate and the

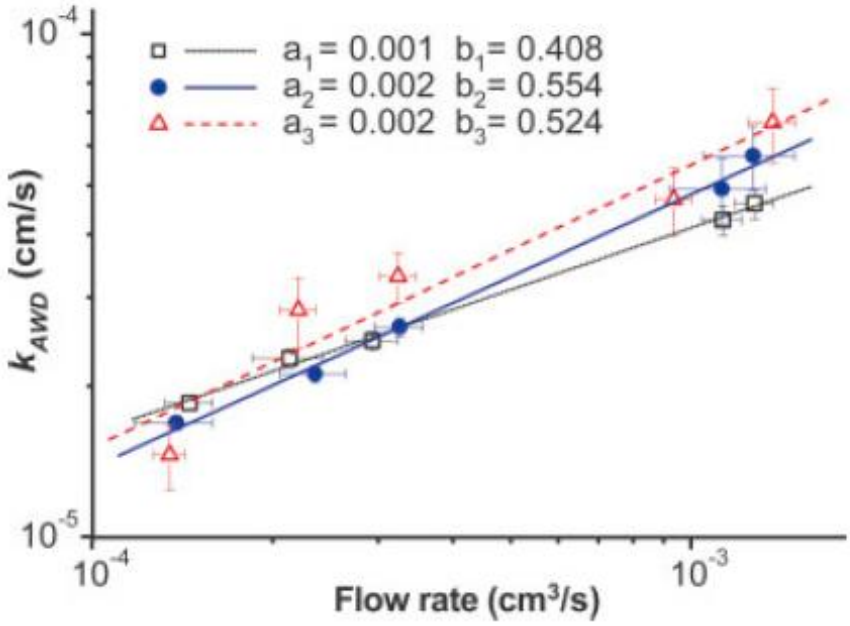

Figure B-3. Dependence of the global mass transfer coefficient kAWD (cm/s) on mass flow rate Q (cm^3/s). These data represent three separate AWDs and three benzoic acid substrates. Each symbol corresponds to a different device and substrate. The AWD was operated on the surface of benzoic acid and the concentration of the acid was measured in the efflux for multiple mass flow rates through the device. Each data point represents three to five separate efflux collections and absorbance readings at a single mass flow rate. Error bars are the propagated uncertainty of absorbance values and mass flow rates.

pHEMA sponge. The measured parameters are consistent with predictions of mass transfer into a flow through a porous material, for which *b* is 0.5; this scaling indicates that the global mass transfer coefficient, k_{AWD}, varies as the square root of the flow rate, *Q*. The extraction of solute from the wound bed can thus be controlled by varying the externally imposed volumetric flow rate: for example, in order to double the flux of a solute from the surface of a wound, the volume flow rate must be increased by a factor of 4. To relate the observed rates of mass transfer to the characteristics of the porous exchange layer, we used existing theories of mass transfer within porous media. We can treat the flow through the porous material as a uniform (plug-like) flow

of speed v_{eff} (cm/s) over a solid boundary, where v_{eff} is the net speed of fluid along the direction of motion; this speed corresponds to the front velocity of a solution of nonbinding solute. This treatment is valid provided that diffusion within the pores is fast relative to convection, or, stated otherwise, the pore Péclet number, $Pe_{pore} = v_{pore}d_{pore}/D_{BA/water} < 10$. Here, v_{pore} is the fluid velocity in the pore, d_{pore} is the average pore diameter, and $D_{BA/water}$ is the diffusivity of the solute in the fluid. In the case of our wound dressing, the boundary was the wound bed and the porous medium was the pHEMA sponge. We employed an existing model to express the prefactor, a, in Eq. (2) in terms of the diffusivity of benzoic acid in water, $D_{BA/water}$, the total volume of the device, V, and the tortuosity of the porous medium, τ:

$$a = 1.128\left(\frac{D_{BA/water}}{V}\right)^{0.5}\frac{1}{\tau} \qquad 3$$

Given Eq. (3) and assuming $b = 0.5$, we can predict the mass transfer for a given flow rate through the wound dressing, using the independently obtained tortuosity of the sponge, τ. We estimated the tortuosity of our porous material to be $\sim$ 3 by using the measured permeability and approximate values for porosity and pore diameter. Using the total volume of the active area of the device ($V = V_m + V_s = 0.625$ cm^3) and the diffusivity of benzoic acid in water ($D_{BA/water} = 8 \times 10^{-6}$ cm^2/s) in Eq. (2) we then predicted that the prefactor for our system should be $a = 0.0013$; this value is consistent with the experimentally observed values ($0.0010 < a < 0.0022$).

Although our results for interfacial mass transfer mediated by the AWD are consistent with the established correlation in Eq. (2), it is useful to point out the conditions for which this correlation might not apply. In our experiments, the Péclet number, Pe_{pore}, ranged from 0.125 to 1.25, indicating that diffusion within the pores was fast relative to convection. If Pe_{pore} were to become large (>10), hydrodynamic dispersion would become important in defining the mass transfer, and at high rates of perfusion or for larger solutes (with low diffusivity), the exponent in Eq. (1) would

change to $b = 0.33$. At the maximum mass flow rate (and maximum pore velocity) used for our experiments, the square root scaling may break down for extracted molecules with free diffusivities less than 1×10^{-6} cm^2/s, leading to lower rates of mass transfer relative to the prediction of Eq.(2).

B-4 Discussion and conclusions

When designing and characterizing the AWD, we focused on mass transfer—exchange of solute between the perfusing liquid and the wound bed. In a clinical context, the ability to generate well-defined mass exchange with the wound bed could be useful for the delivery of therapeutics, the elimination of destructive soluble factors in the wound, and the collection of chemical samples from the wound for diagnostic purposes. Our design allows active mass transfer with or without the application of significant mechanical stress on the wound bed; this decoupling mass exchange and mechanical action is not achievable with current AWDs, and may be useful clinically for the elucidation of the distinct roles of mass transfer and mechanical stimulation in defining the therapeutic function of active dressings.

Potential weaknesses of our AWD for clinical application include the complexity of application and operation relative to conventional dressings and current active dressings, and binding of certain solutes to the dressings in a manner that complicates analysis of the exudates. The implementation of the AWD on arbitrary wound shapes poses a potential challenge, in that it would be impossible to fabricate AWDs to fit every possible wound shape. A possible approach would be to use a device with an active area that is larger than the footprint of the wound bed, and apply an inert sealant (i.e., vaseline) to the edge of the wound; the sealant would occlude the area of the device outside the wound site, ensuring that healthy tissue around it is not affected by the AWD. For larger wounds, a combination of devices running in parallel could be used; our demonstration of operation with barriers supports the hypothesis

that independent regions from distinct devices could be operated side by side without interfering with one another.

We described material characterization, device fabrication and basic operation of an AWD. This AWD allowed for mass exchange with a substrate with both spatial and temporal control. The delivery of solutes demonstrated the feasibility of using this device to act as a therapeutic tool; the collection of solutes indicated the possible use in “diagnostic mode” for continuous assessment of wounds.

REFERENCES

1. Cabodi, M., et al., *An active wound dressing for controlled convective mass transfer with the wound bed.* J Biomed Mater Res B Appl Biomater, 2006.

APPENDIX C

MATLAB COMPUTER CODES

C-1 Protrusion map with color-coded time information

```
function coords = linefile2(fname)

  figure, hold on
  coords = load(fname);
  cmap = colormap(jet);   %% CHANGE COLORMAP HERE %%
  max_time = max(coords(:,3));
  cmap_step = size(cmap, 1)/max_time;

  for i=1:1:size(coords,1)
    current_x = coords(i, 1);
    current_y = coords(i, 2);
    current_time = coords(i, 3);
     z = line([0 current_x], [0 current_y], 'Color',
   cmap(ceil(cmap_step*current_time),:));
  end

  cbar_length = size(get(colorbar, 'YTick'), 2);
  ticks = linspace(min(coords(:,3)), max(coords(:,3)),
cbar_length);
  colorbar('YTickLabel', {ticks});
```

C-2 Angle between two vectors

```
function answer = ang(a, b)

  %%% answer is the angle between a and b, in degrees
  %%% a is a 2d line [x_a, y_a]
  %%% b is a 2d line [x_b, y_b]

  x_a = a(1,1);
  y_a = a(1,2);
  x_b = b(1,1);
  y_b = b(1,2);

  mag_a = sqrt( x_a^2 + y_a^2);
  mag_b = sqrt( x_b^2 + y_b^2);

  dotab = dot(a, b);

  answer = acosd( dotab / mag_a / mag_b );
```

C-3 Circular Statistics Toolbox for Matlab [1, 2]

Mean angle of protrusions:

```
function [mu ul ll] = circ_mean(alpha, w)

if size(alpha,2) > size(alpha,1)
    alpha = alpha';
end

if nargin<2
  % if no specific weighting has been specified
  % assume no binning has taken place
    w = ones(size(alpha));
else
  if size(w,2) > size(w,1)
    w = w';
  end
end

% compute weighted sum of cos and sin of angles
r = w'*exp(1i*alpha);

% obtain mean by
mu = angle(r);

% confidence limits if desired
if nargout > 1
  t = circ_confmean(alpha,0.05,w);
  ul = mu + t;
  ll = mu - t;
end
```

Resultant length:

```
function r = circ_r(alpha, w, d)

% check vector size
if size(alpha,2) > size(alpha,1)
    alpha = alpha';
end

if nargin<2
  % if no specific weighting has been specified
  % assume no binning has taken place
    w = ones(size(alpha));
else
  if size(w,2) > size(w,1)
    w = w';
  end
end

if nargin<3
  % per default do not apply correct for binned data
  d = 0;
end
```

```
% compute weighted sum of cos and sin of angles
r = w'*exp(1i*alpha);

% obtain length
r = abs(r)/sum(w);

% for data with known spacing, apply correction factor to
correct for bias
% in the estimation of r (see Zar, p. 601, equ. 26.16)
if d ~= 0
  c = d/2/sin(d/2);
  r = c*r;
end
```

V-test

```
function [pval v] = circ_vtest(alpha, dir, w, d)

if size(alpha,2) > size(alpha,1)
    alpha = alpha';
end

if nargin<3
  % if no specific weighting has been specified
  % assume no binning has taken place
    w = ones(size(alpha));
else
  if size(w,2) > size(w,1)
    w = w';
  end
  if length(alpha)~=length(w)
    error('Input dimensions do not match.')
  end
end

if nargin<4
  % per default do not apply correct for binned data
  d = 0;
end

% compute some ingredients
r = circ_r(alpha,w,d);
mu = circ_mean(alpha,w);
n = sum(w);

% compute Rayleigh's R (equ. 27.1)
R = n * r;

% compute the V statistic (equ. 27.5)
v = R * cos(mu-dir);

% compute u (equ. 27.6)
```

```
u = v * sqrt(2/n);

% compute p-value from one tailed normal approximation
pval = normcdf(u);
```

C-4 Bonassar Lab Confined Compression Code:

Chunkdata

```
function chunkdata;
%data format [points elapsedtime scantime disp load]
%this is an attempt at a chunking program
%this program will open the the data file from the induratec
and save the
%header and the text seperately
%the data has to be TAB DELIMINATED- no commas- therefor
megan's data can
%not be read through this program.

[h,info] = hdrload('info.txt');

diameter = info(2,1)  % need to get these as inputs
stepsize = info(3,1)  % in mm
h0 = info(1,1)       % in mm
nsteps = info(4,1)     % number of steps

[h,data] = hdrload('data.txt');
% data=[points, elapsedtime, scantime ,Displacement(mm), load]
% debug change columns for stress and strain appropriately

time = data(:,2);
stress=data(:,5).*(1000^2*9.81*4)/(pi*diameter^2); %(:,5)
strain=data(:,4).*(-1)/h0;     %(:,4)
ri=abs(data(:,4))./stepsize;   %rough incrimenting (for
chunking)  (:,4)

data = [time, stress, strain, ri];

format short

% repeat the last row of data for no reason and fix the index
data = [data; data(end,:)];
data(end,end) = nsteps + 1;

% round (:,4) to the nearest integer, throwing out rows not
within .25
data = data(find(abs(round(data(:,4))-data(:,4)) < 0.25),:);
data(:,4) = round(data(:,4));

% find mean stress when (:,4) = 0
mean_stress = mean(data(find(data(:,4)==0),2));

% normalize stresses
data(:,2) = data(:,2) - mean_stress;
```

```
% remove angry rows
data = data(find(data(1:end-1,2) < data(2:end,2)),:);

% do some step junk
cd Steps
i=1
for i = 1:nsteps
    I = find(data(:,4)==i)
    i
    index(i) = I(1)
    index(i+1) = I(end)+1;

    chunkdata = data(I,1:3);

    filename = sprintf('%d.txt',i);
    fid = fopen(filename,'w');
    fprintf(fid,'%6.2f\t %12.8f\t %12.8f\n',chunkdata');
    status = fclose(fid);


    subplot(ceil(nsteps/2),2,i)
    plot(chunkdata(:,1),chunkdata(:,2),'.')

    title(sprintf('%d step',i));
end
```

Data Analysis:

```
function dataanalysis
format compact;

cd

[h,info]=hdrload('info.txt');
h0=info(1,1)
cd Analysis;
param=importdata('Parameters.txt');

tau=param(:,2);
eqstress=param(:,3);
strain=param(:,4)


% graph the Eq Stress-Strain curve and ask user to select
linear region
plot(strain,eqstress,'o');

ans=input('if all data looks good enter 0.  If not enter points
you want to exclude (in row vector if more than one point
\n[#,#,#]\n )');

while ans ~= 0
    tau(ans',:)=[];
    eqstress(ans',:)=[];
```

```
    strain(ans',:)=[];
    figure(2);
    plot(strain,eqstress,'o');

    ans=input('If figure 2 is correct enter 0.\n if not re
enter the points from figure 1 that you would like to remove.\n
example[#,#,#]');
end
```

SRCurvefit

```
[h,info]=hdrload('info.txt');
            nstep=info(4,1);
            cd steps;
             for i = 2:nstep
               name = sprintf('%d.txt',i);
               dd=pwd;
               disp(sprintf('%s:%s',dd,name));

               [model,real,values,fit]=SRfit(name);
               Stress(i,1:4)=model;         %[A,B,C,Strain]
A,B,C are Rawly's curve fit values-have to convert
               R2(i,1)=fit;
               numberplots=nstep;
               if 1==isodd(nstep)
                  numberplots=nstep+1;
               end
               subplot(numberplots/2,2,i)
               tit = sprintf('%d step',i);

plot(real(:,1),real(:,2),'o',values(:,1),values(:,2),'rx-');
               legend('Data', 'Aexp(B*x)+C');

             end
```

REFERENCES

1. Berens, *Technical Report No. 184 The circular statistics toolbox for Matlab.* Max Planck Institute for Biological Cybernetics, 2009.
2. Zar, J.H., *Biostatistical analysis*. 4th ed. 1999: Prentice Hill.